The Dissertation Committee for Xiaobin Xu Certifies that this is the approved version of the following dissertation:

Ultrasensitive Surface Enhanced Raman Scattering Nanomotors

—for Location Predicable Biochemical Detection, Single-Cell Bioanalysis, and Controllable Biochemical Release and Real-Time Detection

Committee:

Donglei (Emma) Fan, Supervisor

Paulo J. Ferreira

Charles Buddie Mullins

Ray T. Chen

Arumugam Manthiram

Ultrasensitive Surface Enhanced Raman Scattering Nanomotors

—for Location Predicable Biochemical Detection, Single-Cell Bioanalysis, and Controllable Biochemical Release and Real-Time Detection

by

Xiaobin Xu, B.E.; M.E.

Dissertation

Presented to the Faculty of the Graduate School of

The University of Texas at Austin

in Partial Fulfillment

of the Requirements

for the Degree of

Doctor of Philosophy

The University of Texas at Austin

August 2014

Acknowledgements

The first person I would like thank greatly is my advisor, Prof. Donglei Fan. Thank you for offering me the opportunity to study in your group at UT-Austin. I believe that choosing to join your group has been one of the best decisions in my life. The most important things I learned from you are to have the right attitude for research and the characteristics necessary to become an excellent researcher. Thanks for letting me work on so many fantastic projects; I have really loved this research experience. Thanks too for your rigorous guidance in almost every aspect of my research. Without you, I would not have had so many achievements. Moreover, I will never forget how you helped me revise my manuscripts and practice my presentations without sleep. I am very fortunate to be your student because you are the best advisor.

I would also like to give thanks to all of my collaborators. I wish to thank: Prof. Alan X. Wang for your excellent work on optical simulation; Prof. Ray T. Chen for your extensive support on optical devices, which helped me obtain my first publication; and Prof. Paulo Ferreira for your help in taking perfect HRTEM images and your assistance in accessing the High Resolution Tunneling Electron Microscope (HRTEM). I am also indebted to my fellow students Kwanoh Kim, Chao Liu, Jing Ning, Jianhe Guo, Michael Asoro, and Dr. Huifeng Li. Your dedicated collaboration and friendship are very important to my life and career.

I am also grateful for all of my committee members, Prof. Paulo J. Ferreira, Prof. Charles Buddie Mullins, Prof. Ray T. Chen and Prof. Arumugam Manthiram, for the time, effort, and great advice you have provided me on my thesis proposal and dissertation.

I am also thankful for all of Prof. Fan's group members: Kwanoh Kim, Chao Liu, Wesker Lei, Jing Ning, Jianhe Guo, and others that have made the lab such a welcoming place over the years. I have really enjoyed the time working with you.

I would like to thank all the faculty and staff members of the Materials Science and Engineering Program at The University of Texas at Austin. Since my first day at UT-Austin, Prof. Kovar has always provided me with great advice on my courses. He was also a great mentor when I was working as a teaching assistant for the class ME 136 L. I am thankful for Prof. Manthiram for the kind support in testing our materials for applications in energy devices. I am also grateful for Prof. Babenberg for the critical advice on TEM characterization and Dr. Jianshi Zhou for allowing me to access the instruments. Thank you to Dr. JP Zhou for the helpful HRTEM training. Rebecca, Bonnie, Liz, and Joan, for your timely assistance that enabled me to conduct research smoothly—Thanks a lot! I would also like to express my gratitude to all the staff members in the Center of Nano and Molecular Science and Technology, and Drs. Zhang, Celio, and Smith for your training on various instruments. Finally, I would like to dedicate this dissertation to my wife and our parents for their love and support.

Ultrasensitive Surface Enhanced Raman Scattering Nanomotors

—for Location Predicable Biochemical Detection, Single-Cell Bioanalysis, and Controllable Biochemical Release and Real-Time Detection

Xiaobin Xu, Ph. D.

The University of Texas at Austin, 2014

Supervisor: Donglei (Emma) Fan

Localized surface plasmon resonance resulting from the concerted oscillations of conduction-band electrons in noble-metal (Au, Ag) nanostructures greatly induces enhanced electric (***E***) fields in confined nanoscale locations, such as on the tips of nanorods or in the junctions of nanodimers. These ***E***-field enhanced locations are called hot spots. In the vicinity of hot spots, Raman scattering spectra of biochemicals can be substantially amplified with an $\boldsymbol{E}^4$ dependence due to the ***E***-field enhancement of both the incident light and Raman spectra. This is called surface enhanced Raman scattering (SERS). SERS is known for its high sensitivity in providing fingerprint vibrational information of molecules. It has triggered intense interest because of its potential applications for label-free and multiplex biochemical detection relevant to medical, environmental and defense purposes. However, the tremendous potential of SERS for ultrasensitive detection has still not materialized because of four major obstacles: (1) it is extremely difficult to obtain a large number of hotspots for sensitive and reproducible detection due to the stringent requirement of hot spots of only a few nanometers; (2) it is arduous to achieve ultrasensitivity for the detection of a single/few molecules; (3) it is challenging to assemble the hot-spots at designated positions for location predicable

sensing; and (4) it is even more difficult to change the state-of-the-art static/passive sensing schemes into dynamic/robotized schemes and also to incorporate multi-functionality into a single SERS nanostructure.

In this research, we addressed the aforementioned problems by rational design, fabrication and robotization of ultrasensitive SERS nanomotor sensors. A nanomotor sensor consists of a tri-layer structure with a three-segment Ag/Ni/Ag nanorod as the core, a thin layer of silica in the center, and uniformly distributed Ag nanoparticles as the outer layer. The inner metallic nanorod core is the key structure in realizing the concept of the robotization of nanosensors, which can be electrically polarized and thus efficiently manipulated by electric tweezers. The presence of the Ni segment in the metallic nanowire core also allows manipulation and assembling by magnetic interactions. The central silica layer provides a supporting substrate for the synthesis of the Ag nanoparticles and separates the Ag nanoparticles from the metallic nanorod core to eliminate the effect of plasmonic quenching. Finally, the outermost layer made of Ag nanoparticles with optimized sizes and junctions provides a large number of hot spots (~1200/μm^2) for ultrasensitive SERS detection with single molecule sensitivity and an enhancement factor (EF) of 1.1×10^{10}. Moreover, two additional SERS enhancement mechanisms were investigated, i.e., the optical management with nanophotonic devices and the near field effect, which can readily increase the EF by 10 and 2 times, respectively, to at least 10^{11}.

Finally, three applications of the SERS nanomotor sensors have been demonstrated: (1) the ultrasensitive SERS nanomotors were transported and assembled into a 3×3 array for location predicable sensing of multiplex molecules; (2) ultrasensitive SERS nanomotors were transported to individual living cells amidst many

cells for single-cell bioanalysis; and (3) the SERS nanomotor sensors can be controlled to rotate by the electric tweezers for tunable biochemical release and detection.

This research, exploring robotized nanosensors by integrating SERS and NEMS, is innovative in both material design and device concept, which could inspire a new device scheme for various bio-relevant applications.

Table of Contents

List of Tables

List of Figures

List of Illustrations

Chapter 1: Introduction*

1.1 Physics of Raman Scattering

When light shines on atoms or molecules, most photons are elastically scattered, which means that the scattered photons have the same frequency as the incident light, i.e., $\nu_{incident} = \nu_{scattered}$. This phenomenon is called elastic Rayleigh scattering. However, as discovered by the Nobel Prize laureate, Dr. Venkata Raman, there is a small fraction of light that undergoes inelastic scattering (~1/1,000,000 or less), which gains or loses energy due to the absorption or release of quantized vibrational or rotational molecular modes as shown in Figure 1.1. This effect is the so-called Raman scattering.

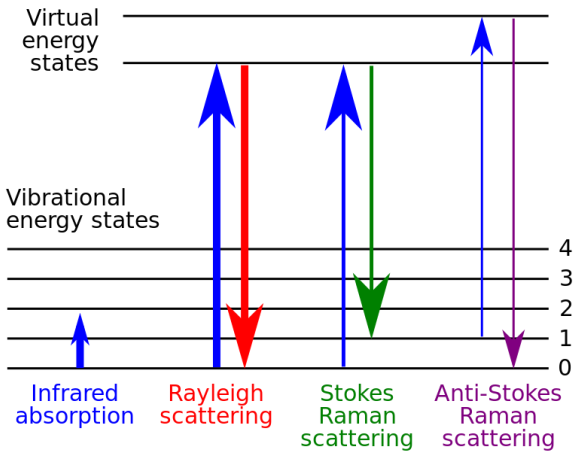

Figure 1.1: Diagram of energy band of Raman scattering.

* Portions of this chapter have been previously submitted to X. Xu, K. Kim and D. L. Fan, ASME-Journal of Nanotechnology in Engineering and Medicine, submitted (2014)

1.2 DISCOVERY AND HISTORY OF SURFACE ENHANCED RAMAN SCATTERING

It has been over 40 years since Fleischmann *et al.* first observed the substantially enhanced Raman scattering spectra of sub-monolayer pyridine molecules on electrochemically roughened silver (Ag) electrodes in 1973[1]. Four years later, two research groups independently reported that increased concentrations of the molecular species could not be the cause of the enhancement of Raman scattering. Jeanmaire and Van Duyne farsightedly proposed that the enhancement is due to the strengthened localized electric fields in closely positioned Ag nanoparticles, the so-called hot spots[2], while Albrecht and Creighton suggested that the enhancement is the result of charge transfer between plasmonic nanoparticles and analyte chemicals[3]. Today, both theories are widely accepted and this phenomenon is known as surface enhanced Raman scattering (SERS).

Early investigations of SERS were largely focused on phenomena occurring on electrochemically roughened Ag substrates. However, electrochemically roughened Ag substrates cannot provide the substantial SERS enhancement factor (EF) that is necessary for single-molecule detection. Until recently, the design and synthesis of SERS substrates has been remarkably improved, largely due to vigorous advances in micro- and nanofabrication. An EF of $\sim 10^{10}$ has been reported, which can readily detect single molecules of various species.[4,5] Additionally, because of the advantages in detecting molecules in a label-free and multiplex manner, SERS was applied to the detection of various bio-relevant species, such as DNA/genes[6-9], anthrax[10,11], chemical warfare

stimulants[12], and glucose levels in patients[13-19]. SERS has also been used to explore environmental protection issues, the study of chemical catalysis,[20,21] and for the detection of explosive agents for defense purposes.

However, the practical applications of SERS for biochemical detection remain extremely challenging because: (1) it is difficult to create a large number of hotspots; (2) it is arduous to obtain ultrahigh sensitivity for the detection of a broad spectrum of species; (3) it is even more challenging to realize location predicable sensing for rapid detection; and (4) most of the state-of-the-art sensors function in a passive and static fashion. Robotization of the SERS sensors for active and dynamic sensing is in dire need for biological applications.

In this research, we addressed the aforementioned issues by the rational design, fabrication and robotization of ultrasensitive SERS nanomotor sensors. A nanomotor sensor consists of a tri-layer structure with a three-segment Ag/Ni/Ag nanorod as the core, a thin layer of silica in the center, and uniformly distributed Ag nanoparticles as the outer layer. The inner metallic nanorod core is the key structure in realizing the concept of robotization of nanosensors, which can be electrically polarized and thus efficiently manipulated by electric tweezers. The presence of the Ni segment in the metallic nanowire core also allows manipulation and assembling by magnetic interactions. The central silica layer provides a supporting substrate for the synthesis of the Ag nanoparticles and separates the Ag nanoparticles from the metallic nanorod core to eliminate the effect of plasmonic quenching. Finally, the outermost layer made of Ag

nanoparticles with optimized sizes and junctions provides a large number of hot spots (~1200/μm^2) for ultrasensitive SERS detection with single molecule sensitivity and an EF of 1.1×10^{10}. Moreover, two additional SERS enhancement mechanisms were investigated, namely, the optical management with nanophotonic devices and the near field effect, which can readily increase the EF by 10 and 2 times, respectively, to at least 10^{11}.

1.3 SERS ENHANCEMENT MECHANISMS

SERS enhancement can be attributed to two mechanisms: electromagnetic and chemical enhancements. It is critical to understand both enhancement mechanisms to design and fabricate optimized SERS substrates.

1.3.1 Electromagnetic enhancement

The mechanism of electromagnetic enhancement dominates most SERS studies. A localized surface plasmon occurs when an electromagnetic wave interacts with metal nanoparticles, where the conduction-band electrons in the metal nanoparticle collectively oscillate due to the incident light. As a result, greatly enhanced electric fields can be found in the vicinity of the nanoparticles [Figure 1.2]. SERS uses this large local field to boost Raman scattering signals of molecules at or close to the surface. For molecules in the vicinity of nanoparticles, the single molecule enhancement factor (SMEF) due to SERS can be expressed as[22]:

$$SMEF \approx M_{Loc}(\omega_L)M_{Rad}(\omega_R) \approx \frac{|E_{Loc}(\omega_L)|^2}{|E_{Inc}|^2}\frac{|E_{Loc}(\omega_R)|^2}{|E_{Inc}|^2} \quad (1)$$

where M_{Loc} is the local field intensity enhancement, M_{Rad} is the radiation enhancement

factor, and ω_L and ω_R are the resonant angular velocities of the local field E_{loc} and radiation field E_{rad}, respectively. In many cases, the Raman shift is small and one can make the additional approximation that $\omega_L=\omega_R$, which leads to the famous expression of the SERS enhancement in the $|E|^4$ -approximation as $SMEF \approx |E_{Loc}(\omega_L)|^4 / |E_{Inc}|^4$.

The meaning of this result is very straightforward; if the electric field can be increased by one order of magnitude, then the SMEF will be increased by four orders of magnitude. Therefore, enhancing the localized electric field is the most effective approach for increasing the sensitivity of SERS.

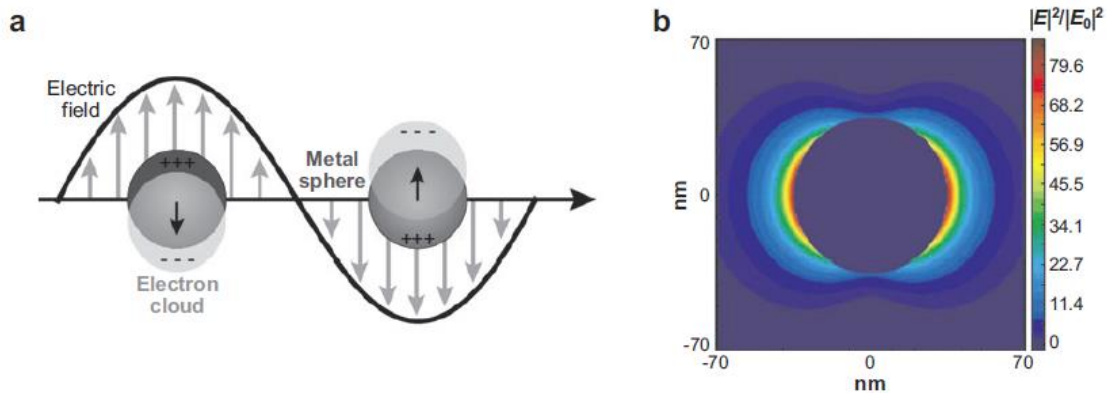

Figure 1.2: (a) Illustration of a localized surface plasmon resonance. (b) Extinction coefficient (ratio of cross-section to effective area) of a spherical silver nanoparticle of 35 nm in radius in vacuum. $|\boldsymbol{E}|^2$ contours for a wavelength corresponding to the plasmon extinction maximum. Peak $|\boldsymbol{E}|^2/|\boldsymbol{E}_0|^2 = 85$.[23]

1.3.2 Chemical enhancement

The electromagnetic enhancement mechanism cannot fully explain the observed magnitude of the SERS enhancement. Experimental evidence shows that there should be a second enhancement mechanism that works independently from the electromagnetic enhancement mechanism. For instance, CO and N_2 molecules differ by a factor of 200 in their SERS intensities at the same experimental conditions. Additionally, the enhancement of molecular resonances when scanning certain electrochemical potentials has been observed.

These observations can be explained by a resonance Raman mechanism (chemical enhancement) in which the new electronic states arising from chemisorption serve as resonant intermediate states in Raman scattering. The highest occupied molecular orbital (HOMO) and lowest unoccupied molecular orbital (LUMO) of the adsorbate are symmetrically positioned in the energy band diagram with respect to the Fermi level of the metal [Figure 1.3]. In this case, charge-transfer excitations (either from the metal to the molecule or vice versa) can occur at approximately half the energy of the intrinsic excitation energy of the adsorbate. The magnitude of the chemical enhancement is usually 10~100-fold.

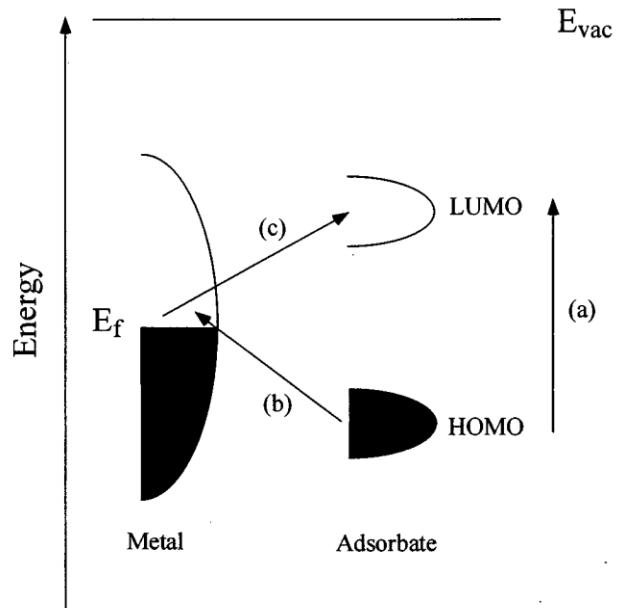

Figure 1.3: Typical energy band diagram of a molecule adsorbed on a metal surface. The highest occupied (HOMO) and lowest unoccupied (LUMO) molecular orbitals are broadened into resonances by their interactions with the metal states; orbital occupancy is determined by the Fermi energy. Possible charge transfer excitations are shown.

Chapter 2: State-of-the-art SERS substrates†

After decades of research on the fabrication of SERS substrates for ultrahigh detection sensitivity [Figure 2.1], four general types of nanostructures have emerged that generate large electromagnetic enhancement: (1) atomic rough surfaces, e.g., roughed Ag surfaces; (2) nanoparticle aggregations that form nanogaps, e.g., dimers and trimers; (3) nanostructures with sharp tips; and (4) designed core-shell nanostructures.[24-26]

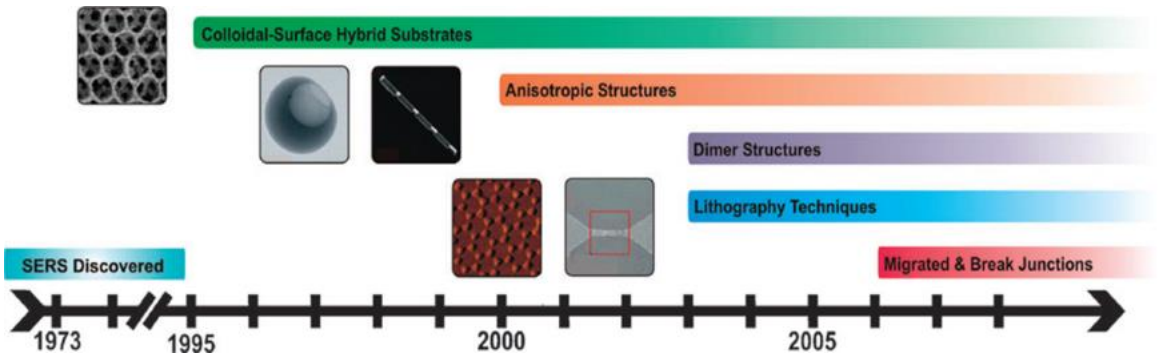

Figure 2.1: Progress on developing suitable SERS substrates.[7,27-36]

Thousands of papers have been published on the fabrication of SERS substrates. Here, we will briefly review the most commonly employed fabrication methods including wet chemical synthesis, lithography fabrication, and other unique methods for SERS sensors.

† Portions of this chapter have been previously submitted to X. Xu, K. Kim and D. L. Fan, ASME-Journal of Nanotechnology in Engineering and Medicine, submitted (2014)

2.1 WET CHEMICAL SYNTHESIS

The wet chemical synthesis approach, such as hydrothermal fabrication, has been broadly adopted for the large-scale efficient growth of monodispersed plasmonic nanoparticles. The size and shape of the plasmonic nanocrystals can be precisely controlled by the temperature, concentration and stoichiometry of the reagents, surfactants or additives. However, most of the as-synthesized nanoparticles are dispersed uniformly in suspension without controlled aggregations, while pairs of nanoparticles with narrow junctions can provide much stronger localized surface plasmon resonance (LSPR). Previously, a salt solution was added during the drying process of nanoparticles, which assisted in the compact aggregation of colloidal plasmonic nanoparticles to create nano-junctions between neighboring particles. Although SERS EFs as high as 10^{12} to 10^{14} were reported,[4,5,37] the control of the junctions of nanoparticles (i.e., hotspots) is entirely random in EF enhancement, quantity, and location.[38] To obtain desired dimer/trimer/small aggregate structures, transparent silica or polymers were used to enclose two or more plasmonic nanoparticles in individual capsules.[39-41] Nevertheless, the quantity of nanoparticles in each capsule remains uncontrollable.

With proper design, the wet chemistry method can also be used to fabricate more complex nanostructures, such as Au/Ag nanoshells. Instead of obtaining tiny hotspots from nanoparticle aggregates, which only exist in the nanogaps, Au nanoshells hotspots were synthesized with better control. The fabrication process of Au nanoshells includes the growth of monodisperse silica layers on Au seeds (1–2 nm), followed by the synthesis

of another Au layer to fully cover the silica surface.[42] Ag nanoshells can be obtained in a similar manner.[43] Note that the plasmon resonant frequency of a nanoshell can be tuned from the visible to the infrared region of the electromagnetic spectrum by controlling the dimensions of the core and shell[42-44], respectively, which gives rise to an array of useful applications[8,45,46]. Recently, more complex and biocompatible structures (e.g., nanomatryoshka) were synthesized and applied to biomedical research [Figure 2.2a].[47]

2.2 TOP-DOWN LITHOGRAPHY METHODS

Lithographical techniques, such as photolithography and electron beam lithography (EBL), are broadly utilized in the semiconductor industry. Among all the lithography techniques available, the state-of-the-art EBL technique can synthesize ultrafine plasmonic nanostructures,[28] though it is costly. In 1996, the nanoimprint lithography technique developed by Chou *et al.*[48] emerged as an economical alternative to EBL for the mass production of nanostrctures [Figure 2.2b]. For instance, Li et al. have successfully created ordered arrays of gold-capped polymer nanofingers over a large area by nanoimprint lithography.[49,50] Controlled numbers of nanofingers can be readily fit together by the action of surface tension from solvent evaporation. In this approach, hotspots were created in the junctions with an EF of ~ 10^{11}.[49 50] Based on a similar concept, Schmidt et al. economically created hotspots in assembled silver-capped Si nanopillars via maskless reactive ion etching.[51]

2.3 OTHER ADVANCED METHODS

Many other unique methods have been developed to synthesize reproducible SERS substrates. The recent breakthrough of on-wire lithography[32,33,35,52-54] (OWL) [Figure 2.2c] demonstrated the capability to control gap size of metallic nanodisk/rod pairs to a few nm and single-molecule sensitivity for various biochemicals, such as methylene blue,[55] p-mercaptoaniline,[56] and Cy-3-labeled DNA,[57] has been reported. Other methods, including nanosphere/colloidal lithography[29,58] [Figure 2.2d], and porous template-assisted deposition[36] were explored for sensitive and location-predictable SERS sensing.

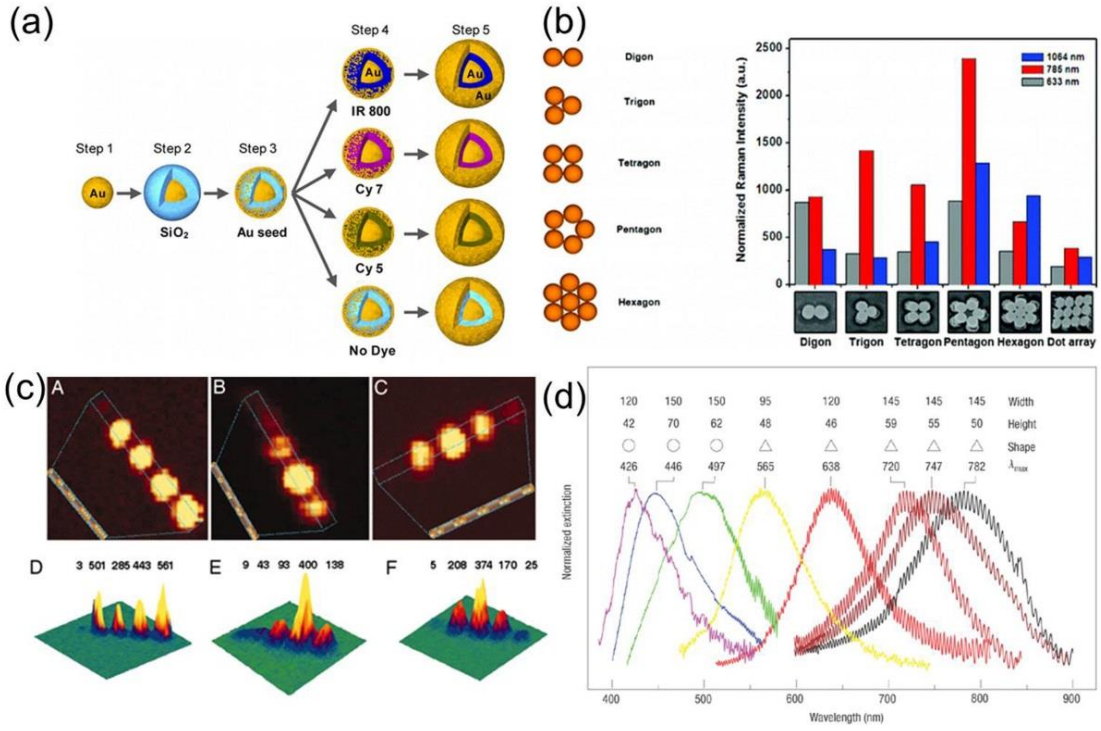

Figure 2.2: (a) Synthetic process of nanomatryoshkas. (b) Schematic drawings of the polygonal assemblies made by the nanoimprint method, and the corresponding normalized intensity of the Raman signal at 1600 cm^{-1} measured for 633, 785, and 1064 nm incident radiation. (c) Confocal Raman microscopy images of gapped nanowire structures functionalized with methylene blue. (A–C) Two-dimensional Raman images. D (A), E (B), and F (C). (D–F) Three-dimensional Raman images. A Inset, B Inset, and C Inset are schematic representations of the structures being imaged. Peak intensities are in arbitrary units. (d) Effect of size and shape on LSPR extinction spectrum for silver nanoprisms and nanodiscs formed by nanosphere lithography. The high-frequency signal on the spectra is an interference pattern from the reflection at the front and back surfaces of the mica.

Chapter 3: Design and fabrication of longitudinal SERS nanosensors‡

3.1 BACKGROUND

The practical application of SERS for ultrasensitive biochemical detection remains challenging for two primary reasons. First, it is difficult to create a large number of hotspots with controlled junctions at a low cost for sensitive and relatively reproducible detection[59]. Second, it is even more difficult to flexibly assemble the hotspots at specific positions for location predicable sensing.

Previous research in biochemical detection with SERS spectroscopy utilized aggregates of colloidal plasmonic nanoparticles, where the hotspots are, by nature, random in dimensions, quantity, and location.[38] The applications of OWL are still limited by the low density of hot spots. Other methods, including E-beam lithography,[28] nanosphere/colloidal lithography[29], and porous template-assisted deposition[36] were explored for sensitive and location-predictable SERS sensing. However, creating a large number of strong hotspots remains challenging due to the difficulty in controlling the gap size to only a few nanometers.

‡ Portions of this chapter have been previously published in X. Xu, K. Kim, H. Li, D. L. Fan, Advanced Materials, 24, 5516 (2012); X. Xu, H. Li, D. Hasan, R. Ruoff, A. X. Wang and D. L. Fan, Advanced Functional Materials, 23. 4332 (2013)

3.2 DESIGN OF THE NANOSENSORS

In this work, we address the aforementioned issues by economically synthesizing SERS nanocapsules and flexibly assembling them into designed arrays via electric fields for ultrasensitive and location-predictable biochemical sensing. A plasmonic nanocapsule consists of a tri-layer structure with a three-segment Ag/Ni/Ag nanorod as the core, a thin layer of silica as the capsulating layer, and uniformly distributed Ag NPs on the silica as the hotspot layer (Scheme 3.1). Each layer in these nanocapsules serves a specific purpose.

The inner metallic nanorod cores can be electrically polarized and thus manipulated by electric tweezers[60-65] based on combined AC and DC electric fields. The embedded Ni magnets in the nanorods assist the assembly of the nanocapsules onto patterned nanomagnets at designated locations. (Note that the electric tweezers will be discussed in Chapter 5.) The central silica layer provides a supporting substrate for the synthesis of the Ag NP arrays, which also effectively separates the plasmonic Ag NPs from the metallic nanorod cores to eliminate plasmonic quenching. Finally, the outermost layer, which is composed of Ag NPs with optimized sizes and junctions, provides a large number of hot spots (~1200/μm^2) for ultrasensitive detection.

In Chapters 5 and 6, we will discuss how to transport and assemble such nanocapsules into ordered arrays using our recent nano-manipulation invention, the so-called “electric tweezers”. A prototype of a 3×3 nanocapsule sensor array has demonstrated the ability to successfully detect various biochemicals. Such Raman

nanosensors are designed and fabricated to remove the obstacles that have hitherto hindered the broad application of SERS and may inspire new designs of Raman nanosensors.

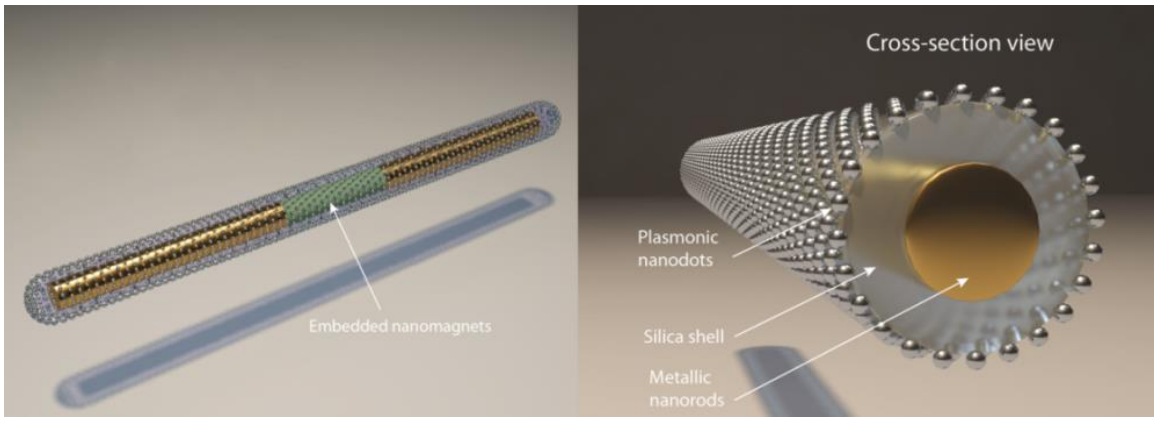

Scheme 3.1: Structure of a tri-layer nanocapsule.

3.3 FABRICATION

The fabrication of nanocapsules follows the steps outlined in Scheme 3.2. We began with the synthesis of multi-segment Ag/Ni/Ag nanorods (300 nm in diameter, L_{Ag}= 2.5 μm, L_{Ni}= 1 μm) by electrodeposition in nanoporous anodized aluminum oxide membranes, as described previously.[32,33] Briefly, a Cu layer that is 500 nm thick was sputtered onto the back of the membrane to seal the pores and to serve as the working electrode in the three-electrode electrodeposition system. The electrodeposition of the nanowires from the working electrode began at the bottom of the nanopores. The amount of electric charge passing through the circuit controls the length of the segments of the Ag/Ni/Ag nanowires in the membrane. After dissolving the membrane in a 2 M NaOH

solution, the nanowires were washed by sonication and centrifuged in ethanol and deionized (D.I.) water twice before being re-suspended in D.I. water.

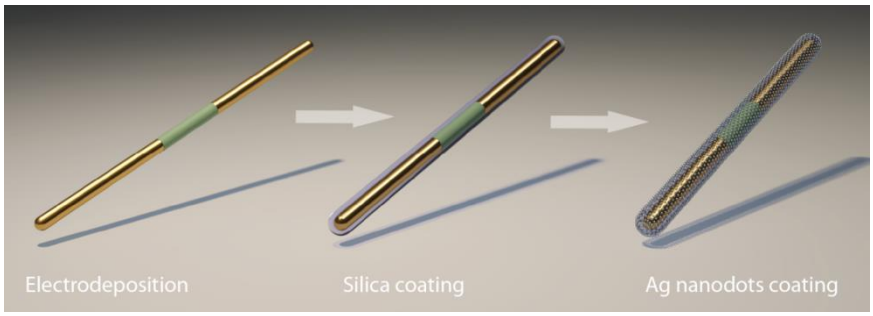

Scheme 3.2: Synthetic process of nanocapsules.

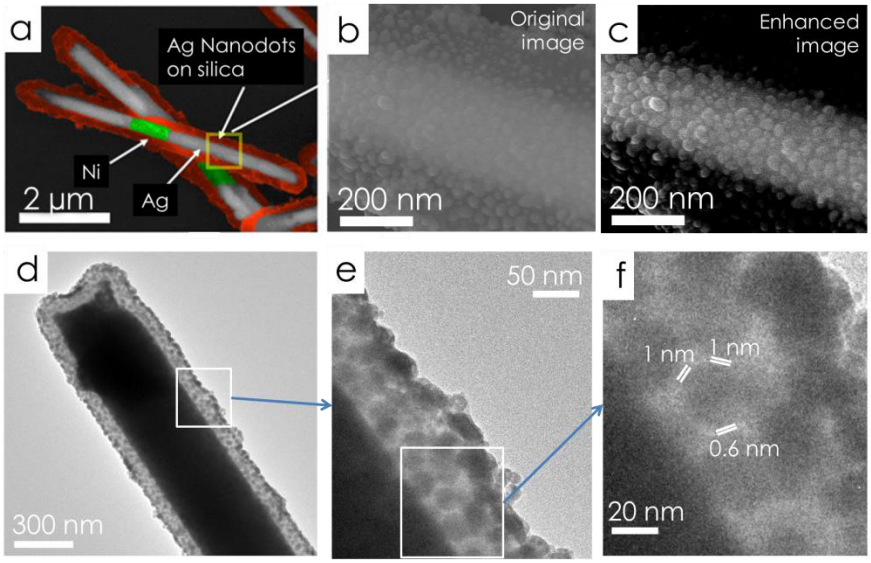

Figure 3.1: Color enhanced SEM images of tri-layer nanocapsules at (a) low and (b) high magnification. (c) The contrast enhanced image of (b). (d–e) TEM images of a typical nanocapsule show a fairly uniform distribution of Ag NPs. (f) Arrays of junctions of the Ag NPs <2 nm.

Next, the Ag/Ni/Ag nanorods were coated with 150 nm amorphous silica via hydrolysis of tetraethyl orthosilicate.[26,66-68] Here, the silica layers serve as supporting substrates for the synthesis of Ag nanodot arrays. Freshly prepared silver nitrate ($AgNO_3$, 0.06 M, 400 μl), ammonia ($NH_3 \bullet H_2O$, 0.12 M, 400 μl), and nanorods (5.7×10^8/ml, 400 μl) were mixed and stirred for 1 hour to enable the silica to adsorb ample Ag ions before polyvinylpyrrolidone (PVP) (in ethanol, 10 ml of 2.5×10^{-5} M) was added. The reactant mixture was incubated at 70 °C to allow PVP to reduce ionic Ag into metallic Ag NPs on the silica. After 7 hours, arrays of Ag NPs were obtained on the surface of the nanorods as shown in Figures 3.1(a) and 3.1(b). By varying the reaction conditions, the average particle size can be tuned from 8 nm to 25 nm.

3.3.1 Estimation of particle and junction sizes.

Measurements within the rectangular highlighted region of Figure 3.2(a) show the average diameter of the NPs was 24.9±6 nm. Figure 3.2(b) is an enhanced SEM image that shows how measurement of the diameter of the nanoparticles was achieved. The size distribution of NPs is shown in the histograms in Figure 3.3(a). In total, there were approximately 115 particles and 330 junctions in the measured region with an area of 0.07 μm^2 (0.16 μm × 0.44 μm). Therefore, the particle density is estimated to be 115/0.07 μm^2 = 1642/μm^2, and the maximum junction density is estimated to be 330/0.07 μm^2 = 4714/μm^2. We find that if the particles have uniform size and are closely packed, then each particle should have six neighboring particles, i.e., each particle contributes three junctions. In this ideal case, the junction density is $1642/\mu m^2 \times 3 = 4926/\mu m^2$.

Next, we directly measured the junction sizes between Ag NPs. Because SERS enhancement drastically increases as the junction size decreases, and because high EF of SERS is generally found in junctions of a few nanometers or less, we only measured junctions ≤ 5 nm and noted that the measurement uncertainty can be large when the junctions have such small values due to the resolution limit of SEM. Additionally, we assumed that the junctions have a size of 0.5 nm when the NPs are too close to measure accurately. If we consider only junctions of ≤ 5 nm as hotspots for SERS enhancement, we obtain a junction size of 2.57±1.18 nm and a hotspot/junction density of 3714/μm^2. If we assume that narrow junctions of ≤ 2 nm contribute to the hotspots, we obtained a junction size of 1.17±0.5 nm and a hotspot/junction density of 1200/μm^2, as shown in Fig 3.3(b–c).

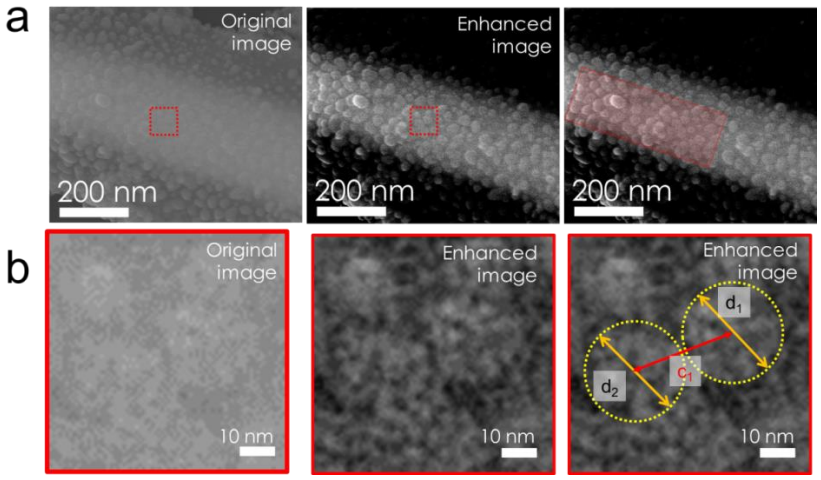

Figure 3.2 Characterization of the size distribution of NPs. (a) Enhanced SEM images from Figure 4.1(b–c), where the region in the red dotted square is magnified to show the characterization in (b).

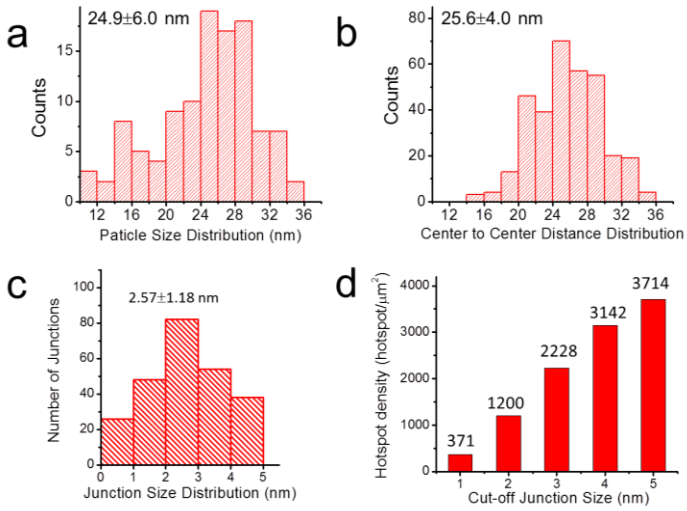

Figure 3.3: (a–b) Size distributions of Ag NPs. (c) Estimation of junction size distribution. (d) Junction/hotspot density by selecting different cut-off junction sizes. Measurements are based on the highlighted rectangular region (of 0.07 μm^2) in figure 3.2(a).

3.4 SERS CHARACTERIZATION

3.4.1 SERS characterization

Before characterizing the SERS sensitivity of the nanocapsules, we studied their optical absorption to determine the optimal condition for SERS sensing. Here, the Ag/Ni/Ag metal cores were removed with the view that most excitation light is absorbed by the outermost Ag nanodot layers, with little energy transfer to the metal cores. The nanocapsules exhibited an absorption peak at 450 nm due to the collective plasmonic resonance of the assembled Ag NPs [Figure 4.4].[69,70] As the absorption was very sensitive to both the size and geometry of the nanoparticles, a broad background was present due to the size and shape distribution of the Ag NPs. With available lasers from 532–633 nm, a 532 nm laser (random polarized) was chosen as the excitation source for Raman scattering measurements because the wavelength of 532 nm is closer to the maximum absorption peak. Consequently, the laser energy can be more effectively absorbed by the nanocapsules, which results in a high intensity $\boldsymbol{E}$-field focused at the hot spots and thus high EF for SERS detection.

Nanocapsules were sparsely dispersed in a 3 mm diameter well made of 1 mm thick polydimethylsiloxane (PDMS) film. BPE (10 μl in ethanol) with concentrations from 1 pM (10^{-12} M) to 1 μM (10^{-6} M) was added to the PDMS well and sealed with a cover slip. The nanocapsules were incubated in the BPE solution for 10 min before being rinsed with ethanol three times for subsequent SERS detection. A 532 nm laser was used

for Raman excitation. Each SERS spectrum was collected from a single focusing spot (~1 μm) on a nanocapsule and integrated for 5 s at the same conditions.

The nanocapsules detected Raman spectra of 1,2-bi-(4-pyridyl) ethylene (BPE) with a concentration as low as 10^{-12} M (1 pM) [Figure 3.5(b)]. The intensity of the SERS at 1644 cm^{-1} increased logarithmically with the concentration of BPE from 1 pM to 1 μM, as shown in Figure 3.5.

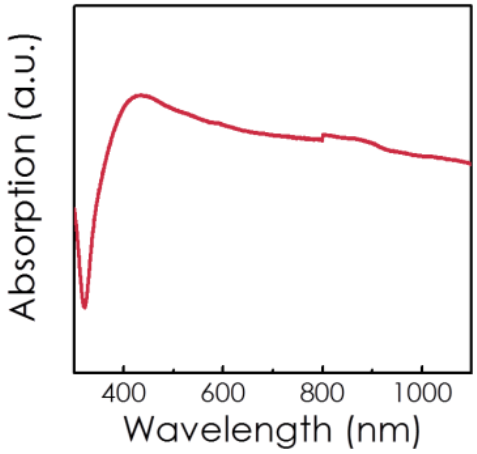

Figure 3.4: Optical absorption of the tri-layer nanocapsules.

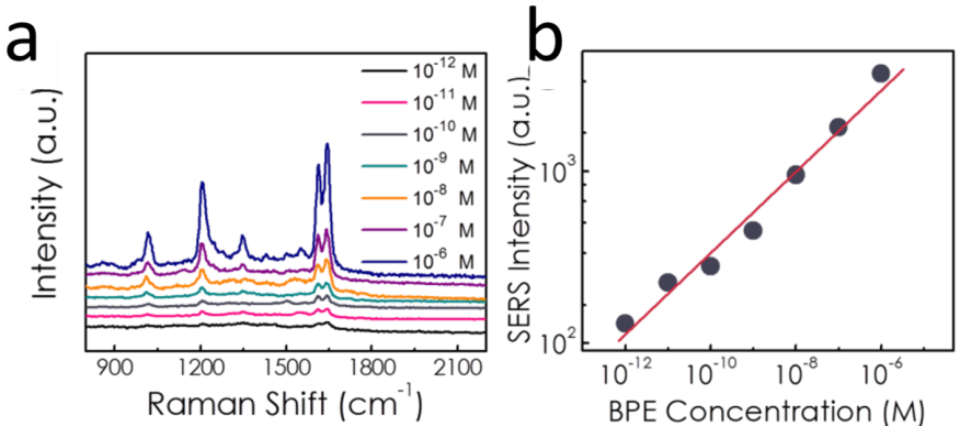

Figure 3.5: (a) SERS characterization of BPE from 1 pM to 1 μM shows clear SERS spectra. (b) SERS intensity increases with BPE concentration.

3.4.2 Estimation of SERS enhancement factor.

We further evaluated the SERS EF of the nanocapsules. The EF of the nanocapsules was measured and estimated to be 1.1×10^{10} following a widely used method[49,51].

Specifically, the SERS EF was calculated by following a commonly used method reported elsewhere: [49,51]

$$EF = \frac{I_{SERS}/N_{SERS}}{I_{RS}/N_{RS}} ,$$

where N_{SERS} is the average number of adsorbed molecules enhanced by the SERS substrate in the detection volume, I_{SERS} is the corresponding SERS intensity, N_{RS} is the average number of molecules excited without surface enhancement, and I_{RS} is its corresponding Raman intensity.

The values of I_{RS} were obtained from 0.1 M BPE in ethanol. A low laser power of 35 μW (532 nm) was chosen to avoid intensity saturation and photo-degradation of the analyte. The laser was fully focused into the BPE solution via a 50× objective. A Raman spectrum with intensity (I_{RS}) of 0.5 counts/second (at 1200 cm^{-1}) was obtained.

N_{RS} is given by $N_{RS}=V_{scat}\,C_{BPE}\,N_A$, where V_{scat} is the scattering volume of BPE that contributes to the measured Raman signal, C_{BPE} is the concentration of BPE (0.1 M), and

N_A is Avogadro's number. V_{scat} is given by $V_{scat}=A_{obj}H_{obj}$, where $A_{obj}=\pi$ (0.5 μm)^2 is the area of the laser spot from the 50× objective and H_{obj} is the effective height of the detection volume of BPE. Therefore, $N_{RS} = A_{obj}H_{obj}c_{BPE}N_A$. We determined H_{obj} using a method reported elsewhere.[71] Briefly, the measurement was performed by moving a silicon <100> wafer via 1 μm increments through the focal plane of the objective and collecting the intensity of the Si Raman signal at 520 cm^{-1} at each point. H_{obj} =13 μm was obtained by integrating the intensity of Raman signal with distance and then dividing by the highest measured signal. Using this method, V_{scat} was determined to be 10.2 μm^3.

Therefore, the total number of molecules (N_{RS}) can be readily known:

$N_{RS} = 0.1mol/L \times 10.2\mu m^3 \times 6.02 \times 10^{23} molecules/mol = 6.14 \times 10^8\ molecules$.

To determine the value of I_{SERS}, we dispersed nanocapsules on a glass substrate, dried them in air, and then incubated them in 1 mM BPE in ethanol for 10 min. The nanocapsules were then rinsed with pure ethanol to remove excess molecules and dried in air. As the nanocapsules are cylinders that possess curvature (600 nm in diameter), we approximated the effective area excited by the laser (spot size 1 μm) to be 1 μm ×0.2 μm= 0.2 μm^2. Under the same experimental conditions described above, we obtained a value of I_{SERS} of 20000 counts/second (at 1200 cm^{-1}). Assuming that molecules residing in the 1.6 nm^3 volume of the 1.17±0.5 nm narrow junction contribute the most to the

measured Raman intensity, where there were approximately 9 molecules/junction for a closely packed monolayer of BPE (3 Å × 6 Å × 10 Å/molecule),[49] we have

$$N_{SERS} = 0.2\ \mu m^2 \times 1200\ hotspots/\mu m^2 \times 9\ molecules/hotspot = 2160\ molecules$$

Therefore,

$$EF = \frac{I_{SERS}/N_{SERS}}{I_{RS}/N_{RS}} = \frac{20000/2160}{0.5/(6.14\times10^8)} = 1.1 \times 10^{10}.$$

3.4.3 SERS mapping

Raman mapping of R6G shows that SERS enhancement was fairly uniform on the nanocapsules. At a concentration of 1 μM, R6G forms a monolayer on the nanocapsules. The functionalization of R6G on nanocapsules follows a procedure that is often used in R6G SERS sensing.[72] Specifically, the nanocapsules were dispersed on a glass substrate and dried in air. The nanocapsules were then incubated in a 1 μM R6G ethanol solution for 2 hours before being washed with ethanol and dried. The Raman mapping was conducted on a single nanocapsule using a confocal 532 nm Raman microscope. The laser spot size was approximately 1 μm, with a scanning step of 250 nm and an integration time of 0.5 s.

Different colors in the Raman mapping represent different Raman intensities of R6G. The Raman intensity at 1655 cm^{-1} was essentially uniform along the axis of the nanocapsules and reduced to zero toward the edges of the nanocapsules due to the

deflated laser on the edges [figure 3.6]. An analysis along the nanocapsules shows that the variation of the Raman intensity (at 1655 cm^{-1}) is within ±9% [figure 3.6]. This low variation suggests that the nanocapsules can readily detect the monolayer analyte with good reproducibility and predictability over their entire surface. Note that the tolerance of detection is actually less than ±9% as the coverage of R6G on the nanocapsules cannot be absolutely uniform. Two factors determine this uniformity: (1) the controlled sizes and spacing of the Ag NPs, which give relatively low variation of EF among hotspots; and (2) the large number of hotspots (of approximately 240) in each detection area [1200 /μm^2 (hot spot density) × 0.2 μm (1/3 of the nanocapsule diameter due to nanocapsule curvature)× 1 μm (laser spot size)]. As a result, the SERS effect is uniform along the nanocapsules because of the averaged EF from all the hotspots in each detection position. Furthermore, we note that the uniform SERS detection demonstrated on our nanocapsules is for monolayer chemicals. With a reduced concentration of the analyte (i.e., less than a monolayer), we expect larger variations of SERS along a nanocapsule, with the final tolerance being determined by the difference of EF from individual hotspots over the entire nanocapsule.

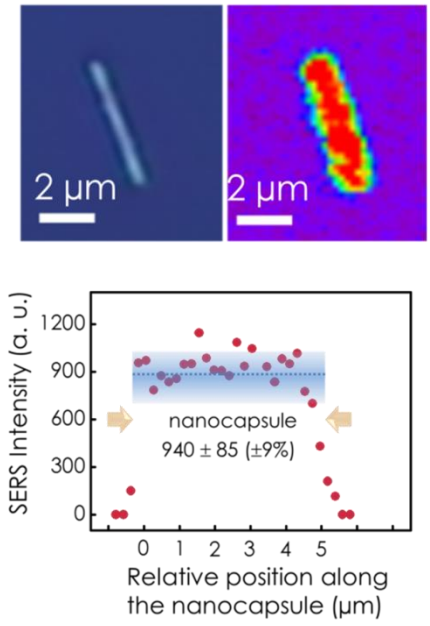

Figure 3.6 Raman mapping profile of 1 μM R6G dispersed on a tri-layer nanocapsule shows uniform SERS intensity on the entire surface and distribution along the nanocapsule (1655 cm^{-1}, scan step 250 nm, integration time 0.5 s).

3.4.4 Single-molecule sensing

According to bi-analyte and temperature-dependent SERS vibrational pumping methods, an EF on the order of 10^7–10^8 is sufficient for the detection of single molecules of various analytes.[73] For example, a SERS substrate with an EF of 5×10^9 has detected a single BPE molecule.[74] Therefore, the high EF value found in the nanocapsules in the present work suggests their single molecule sensitivity.

Accordingly, in another experiment, nanocapsules were dispersed on a glass substrate and dried in air. They were then incubated in 1 pM R6G for 2 hours before

being rinsed with pure ethanol and dried. SERS characterization was performed with a 50 × objective and the 532 nm laser power was set to 35 μW. SERS spectra were recorded with an integration time of 1 s for 100 s. We observed both a strong intensity and frequency fluctuation of Raman spectra from extremely low concentrations of R6G (i.e., 1 pM). These findings are consistent with the single molecule behavior attributed to molecular diffusion into and out of hotspots [Figure 3.7], according to previous reports. [4,38,72,75-79]

As a result, the SERS characterizations have placed the sensitivity of the nanocapsules in the single molecule regime, even though they do not provide definitive proof. [75]

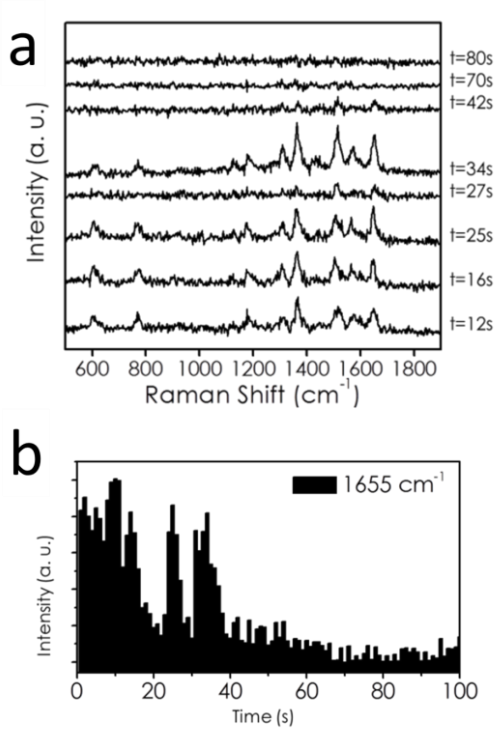

Figure 3.7 (a) Variation of SERS spectra of R6G molecules in a 100 s time frame with a integration time step 1 s for each spectrum. (b) Intensity of SERS at 1655 cm^{-1} as a function of time.

3.5 SIMULATION AND OPTIMIZATION OF SERS ENHANCEMENT

3.5.1 Optimization of the particle and junction sizes of Ag nanoparticles

The Ag NP sizes and junctions can be optimized for highly sensitive SERS detection. With a fixed volume of nanowire suspension (5.7×10^8/ml, 400 μl) and PVP (10 ml of 2.5×10^{-5} M in ethanol), we systematically varied the total volume of $AgNO_3$ (0.06 M) and $NH_3 \cdot H_2O$ (0.12 M) (v:v 1:1) from 20 μl to 1200 μl. Specifically, the following samples were obtained: 20 μl (0.2× sample), 600 μl (6× sample), 800 μl (8× sample), and 1200 μl (12× sample). The morphologies of the as-synthesized nanotubes possess distinct particle and junction sizes (Figure 3.8). The average diameters of the Ag NPs increased from 10.2±2.4 nm (0.2× sample) to 24.8±6.7 nm (8× sample) with the volume of the $AgNO_3/NH_3 \cdot H_2O$ solution. The density of Ag NPs reached a maximum for the 6× sample ($2050/\mu m^2$). The detailed characterization of these findings is provided in figures 3.9–10 and table 3.1. The variation of the particle size may be attributed to a dynamic competition between nucleation and crystalline growth of Ag NPs, which has been commonly observed in NP growth[80].

The highest SERS enhancement was obtained from the 8× sample, which was subsequently employed for SERS detection and ***E***-field assembly in this research. Figure

3.10(c) shows the SERS spectra of 1 mM BPE adsorbed on nanocapsules from the 0.2×, 6×, 8× and 12× samples.

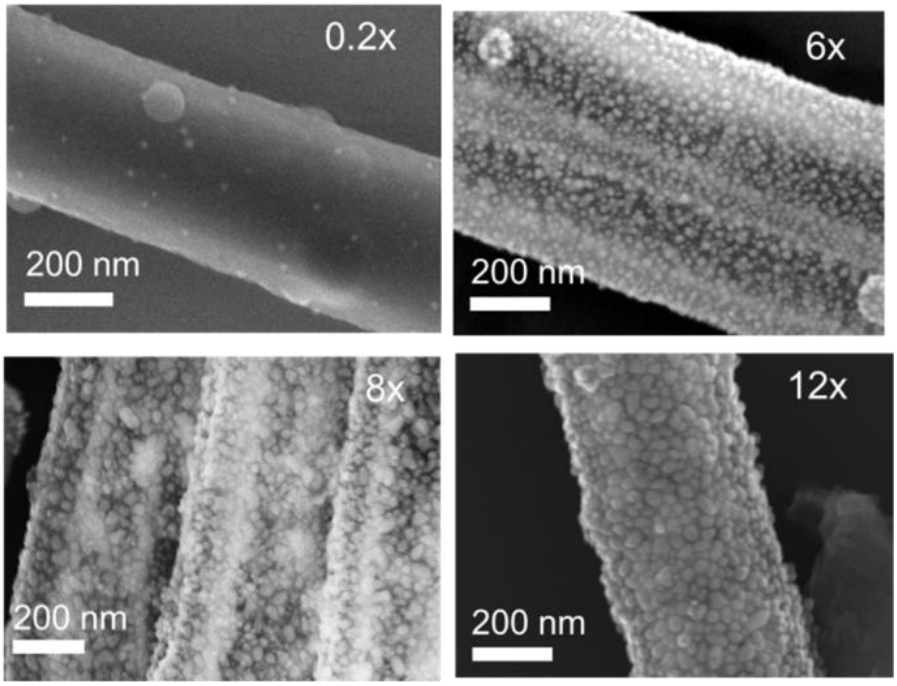

Figure 3.8: SEM images of samples 0.2× to 12× fabricated at different conditions.

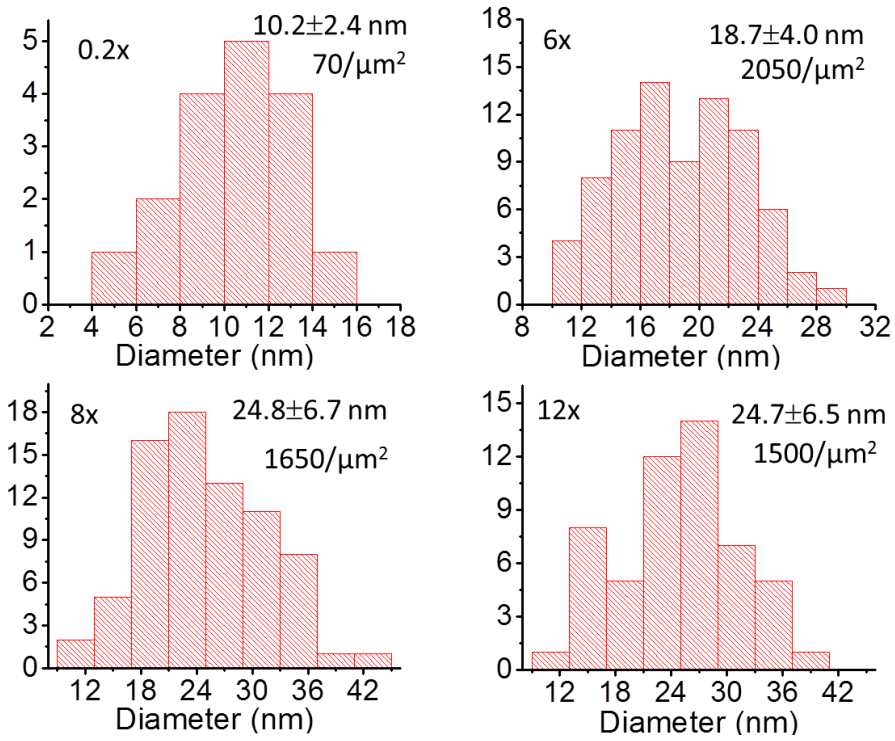

Figure 3.9: Particle size and density distribution of Ag NPs of different samples.

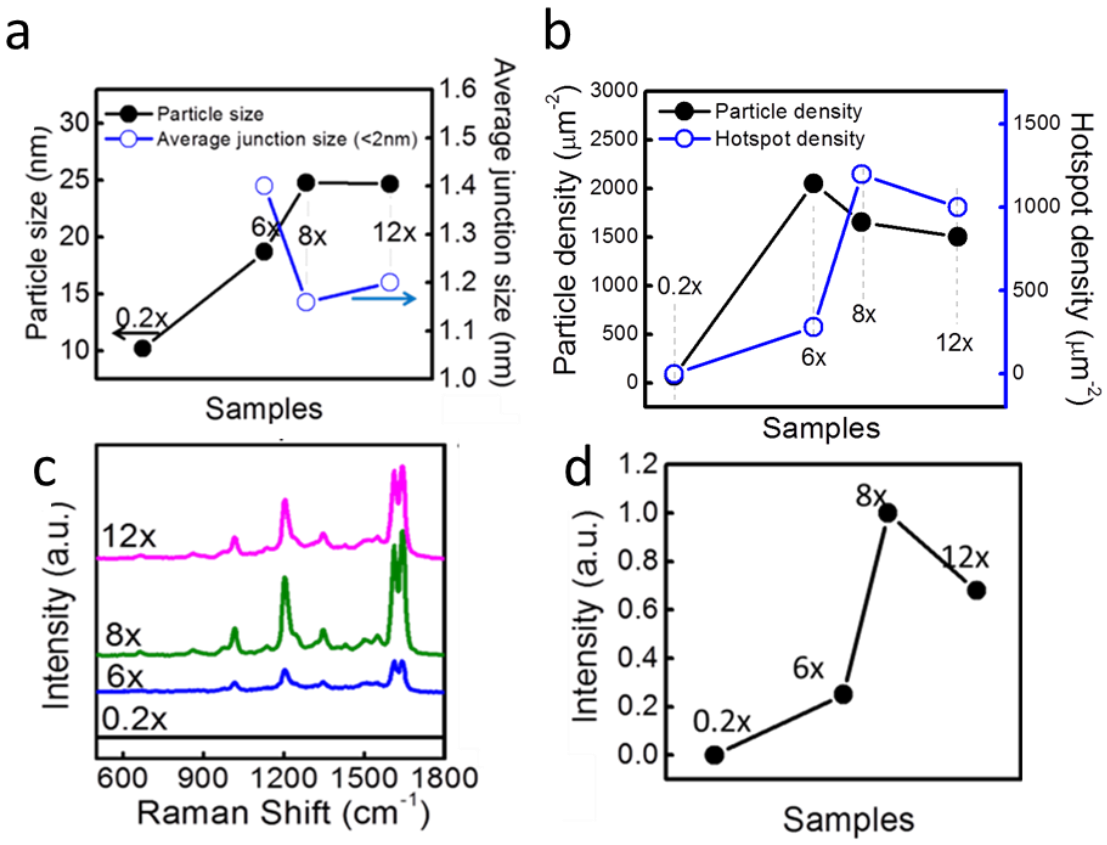

Figure 3.10 (a) Particle size and average hotspot size (< 2nm) of different samples. (b) Particle density and hotspot/junction density (< 2nm) of samples fabricated at different conditions. (c) SERS spectra of 1mM of BPE taken from nanotubes fabricated at various conditions. (d) SERS intensity of nanotubes fabricated at different conditions.

Table 3.1: Summary of particle size, particle density, average hotspot/junction size (<2nm) and density, and SERS intensity for different samples.

Samples	0.2×	6×	8×	12×
Particle size (nm)	10.2±2.4	18.7±4.0	24.8±6.7	24.7±6.5
Density(/μm^2)	70	2050	1650	1500
Junction density (<2nm)(/μm^2)	0	280	1200	1000
Average junction size(<2nm) (nm)	N/A	1.40	1.16	1.20
Normalized SERS Intensity (a.u.)	0	0.25	1	0.68

3.5.2 Plasmonic simulation and discussion

It is of interest to understand how the EF depends on the Ag particle and junction sizes, as well as how the Ag NPs on the hollow structures can further enhance SERS. For this purpose, numerical simulations were conducted and comparisons were made only on nanotubes fabricated in the same batch (300 nm in inner diameter and 70 nm in shell thickness).

It is known that the SERS enhancement can be attributed to two factors, namely, an *E*-field enhancement due to the plasmonic resonance of NPs and a chemical enhancement due to charge transfer between the molecules and metal particles[81]. The *E*-field enhancement can be approximated as[82] $EF \approx \frac{|E(\omega_L)|^4}{|E_0|^4}$, where ω_L is the resonant angular velocity of the local field E in an external field of E_0. Due to the quadruple

dependence on the local *E* field, the *E*-field enhancement is usually considered to be a major contributor to SERS. We used a three-dimensional Finite Difference Time Domain (FDTD) method to simulate this effect.

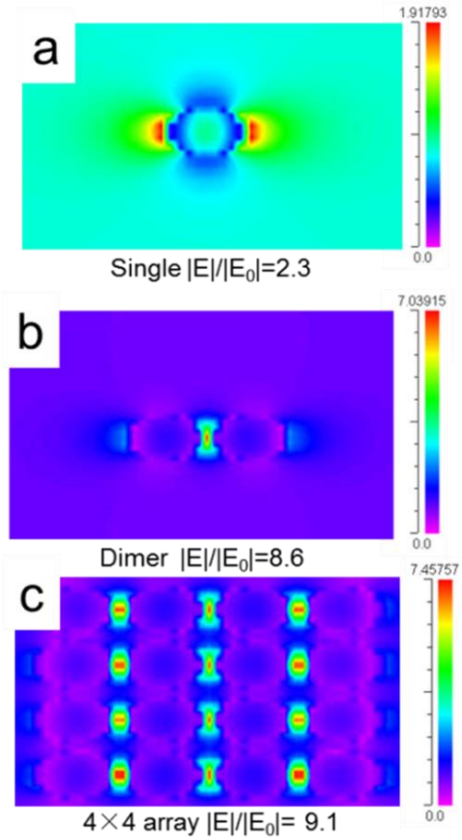

Figure 3.11: Simulation results for Ag NPs of 20 nm in diameter and junction (if any) of 3 nm. (a) A single Ag NP. (b) A dimer of Ag NPs. (c) A 4×4 Ag NP array. The *E*-field enhancement is the highest in the 4×4 Ag NP array and lowest in a single Ag NP.

We simulated the normalized electric field ($|\boldsymbol{E}|/|\boldsymbol{E}_0|$) close to the Ag NPs. The excitation wavelength was set at 532 nm with in-plane polarization perpendicular to the nanotube surface. To determine the effect of NP junctions on SERS EF, we began with simulations for a single particle, a dimer, and finally a 4×4 array (Figure 3.11). The shape of the Ag NPs was assumed to be cylindrical with a uniform thickness of 20 nm, and the junction was set at 3 nm. A single silver NP provided electric field enhancement of $|\boldsymbol{E}|/|\boldsymbol{E}_0|$=2.3; hence, the SERS EF =28 due to the $\boldsymbol{E}^4$ dependence. Metal dimers and the 4×4 array provided $|\boldsymbol{E}|/|\boldsymbol{E}_0|$=8.6 ($EF_{SERS}$ =5470) and $|\boldsymbol{E}|/|\boldsymbol{E}_0|$ =9.1 (EF_{SERS} =6857), respectively. This simulation confirms that a group of metallic particles on the same surface can provide a stronger $\boldsymbol{E}$-field enhancement than that of single particles or dimers.

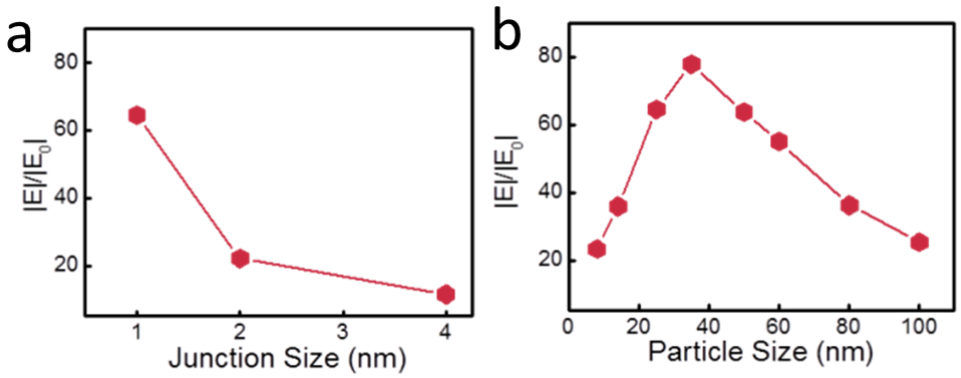

Figure 3.12 (a) The $\boldsymbol{E}$-field EF increases with decrement of the junctions (and with a fixed particle size of 25 nm). (b) The $\boldsymbol{E}$-field EF reaches the maximum value when the particle size is between 30 and 40 nm with a fixed junction of 1 nm.

Therefore, a group of NPs with controlled distributions should further enhance the *E* field. To determine whether this was the case, we simulated the *E*-field enhancement as a function of junctions of the particle arrays. As plotted in figure 3.12(a), narrower junctions between NPs exhibit a strong electric field for an array with Ag NPs of 25 nm in diameter. At a fixed junction of 1 nm, the highest electric field enhancement is obtained in particle arrays with diameters between 20–50 nm, as shown in figure 3.12(b). The simulation results agree remarkably well with previous work, which refer to such results as proof of the "extrinsic size effect"[83]. For NP with larger sizes (>40 nm), the *E*-field enhancement diminishes because the plasmonic resonance shifts to longer wavelengths. When short wavelength lasers excite such NPs they induce higher-order electron cloud distortions of the conduction band electrons and thus degrade the plasmonic resonance. For NPs that are less than 25 nm, the scattering of electrons from the particle's surface produces a damping term that is inversely proportional to the particle diameter. In other words, more optical energy is converted to heat instead of being scattered to give local electric field enhancement. As a result, by comparing the electric fields among NPs with different diameters and junctions, we have optimized the design of the Ag NPs. The result of our simulations readily explains our experimental observation; that is, among all the samples, the 8× samples with the largest diameters (24.8±6.7 nm) and smallest gaps (~ 1.16 nm) offered the highest SERS EF.

Chapter 4: Mechanisms for further SERS enhancement§

4.1 MANAGEMENT OF LIGHT VIA NANOPHOTONIC GRATINGS

Surface enhanced Raman scattering[3,84] has demonstrated single-molecule detection capability[85-87] and has been investigated intensively[88-91] because of its widespread potential in chemical and medical applications. Although a peak enhancement factor as large as 10^{14} can be generated from the random "hot spots" that are created on metallic nanoentities,[87] the density of such "hot spots" is extremely low, which this makes the single-molecule detection event unpredictable. Therefore, a comprehensive enhancement mechanism that can provide a universal increase of the Raman signal intensity across the entire substrate is highly desirable for biomolecule detection.

In recent years, innovative approaches using guided mode resonance (GMR)[92-94] to enhance the already strong localized surface plasmon polaritons (LSPPs) of the metallic nanoparticles were demonstrated to further increase the SERS signals. However, this approach requires the precise placement of rationally designed metallic nanoentities onto the dielectric gratings, either by E-beam lithography[92] or by the separation of SiO_2 nanopillars.[94] The reason for these costly processes is that dispensing a large

§ Portions of this chapter have been previously published in X. Xu, K. Kim, H. Li, D. L. Fan, Advanced Materials, 24, 5516 (2012), X. Xu, H. Li, D. Hasan, R. Ruoff, A. X. Wang and D. L. Fan, Advanced Functional Materials, 23. 4332 (2013) and X. Xu, D. Hasan, L. Wang, S. Chakravarty, R. T. Chen, D. L. Fan and A. X. Wang, "Applied Physics Letters, 100, 191114 (2012)

amount of metallic nanoparticles directly on top of a dielectric grating will dampen the resonant mode and inherently weaken the SERS EFs. Using e-beam lithography to create a rationally designed metallic structure with finite size, or using SiO_2 nanopillars to spatially separate the metallic nanoparticles with the GMR grating, will balance the optical coupling and the energy consumption between the GMR and LSPP modes.

In this work, and in collaboration with Prof. Alan X. Wang, we designed and fabricated a Si_3N_4 grating on a SiO_2 substrate to provide a low quality (Q)-factor GMR enhancement of $3 \sim 4$ over a 15 nm bandwidth centered at a wavelength of 532 nm. This approach can effectively compensate for variations in the device fabrication and ease the precise requirement for the excitation wavelength because of its low sensitivity to phase change. To maintain a good coupling between the GMR and LSPP modes, SiO_2 nanotubes with densely assembled silver nanoparticles are sparsely coated on the Si_3N_4 grating. Because of its small diameter of 450 nm, the SiO_2 nanotubes deliver only a limited amount of silver nanoparticles that are closely coupled to the grating. This attribute minimizes the metal absorption to the GMR mode, though it still provides a sufficient number of "hot spots" for SERS sensing. Compared with e-beam lithography or glancing angle deposition patterned substrate, these plasmonic-active SiO_2 nanotubes can be chemically synthesized in large quantities at low cost and they can be coated directly on the grating surface. Each individual SiO_2 nanotube is an assembly of densely packed "hot spots", which can provide a constant and stable enhancement in addition to the existing SERS effect.

As shown in the inset of figure 4.1, the GMR grating consists of a thin layer of Si_3N_4 grating with a thickness (t) of 300 nm, which is deposited on a SiO_2 substrate. The grating period is P = 340 nm and the grating width is w = 185 nm. Neglecting material dispersion, the refractive indices of Si_3N_4 and SiO_2 at a wavelength of 532 nm are 2.03 and 1.461, respectively. The electric field distribution of a normal incident transverse-magnetic (TM) wave at a wavelength of 532 nm is calculated by the rigorous coupled wave analysis (RCWA) method.[95] The maximum electric field is 4-times the intensity of the incident light and concentrates in the upper area of the air gaps between the Si_3N_4 waveguides.

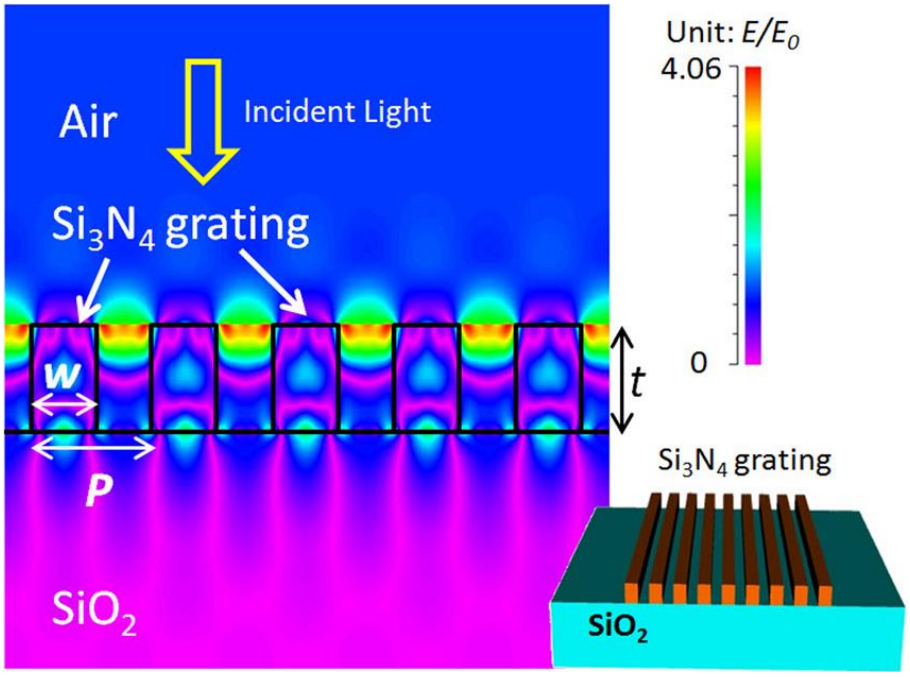

Figure 4.1: Schematic of the proposed GMR grating and the simulated TM mode electric field distribution at the 532 nm resonant wavelength.

To investigate how the resonant mode interacts with metallic LSPPs, we use the RF module from COMSOL 3.5a to numerically compare different SERS substrates. A surface normal constant wave (CW) laser with a 2 μm Gaussian width is used as the excitation light. The first SERS substrate is based on a GMR grating with the aforementioned parameters but without any metallic nanoparticles. We choose the maximum electric field point as the monitoring site. For the second SERS substrate, we use a flat Si_3N_4 substrate and place a silver nanoparticle dimer on top of it. The diameter of the silver particles is 25 nm and the gap between them is 1 nm. The maximum electric field is in the center of the gap. The final SERS substrate is designed by placing the same silver nanoparticle dimer on top of the GMR grating with the lower surface of the dimer aligned to the top surface of the Si_3N_4 waveguides. This configuration is very similar to our experimental setup with SiO_2 nanotubes being placed on top of the GMR grating. However, there is a misalignment between the peak electric field positions of these two structures due to a geometric conflict. Again, the maximum electric field is found to be in the gap of the dimer. Figure 4.2 shows the electric field enhancement (E/E_0, where E_0 is the peak electric field of the incident light) as a function of wavelength for the three SERS substrates. The enlarged view of the electric field distribution of the silver dimer on top of the GMR grating is shown in the inset. The peak EFs are found to be 35.

The effect of the distribution and the number of nanoparticles to SERS EFs on a flat substrate has previously been investigated.[96,97] However, the actual interactions between the LSPP and GMR modes and their impact to SERS EFs have not been

reported. Compared with nanoparticles on a flat substrate, the electric field enhancement of nanoparticles on the GMR grating is more complex. On one hand, having more plasmonic nanoparticles on the grating not only creates more "hot spots", it also enhances the LSPPs due to the near field coupled plasmon resonance of the chain,[98] which results in the enhancement of the total Raman signal. However, plasmonic nanoparticles can absorb photon energy and dampen the coupling between the LSPP and GMR modes, which is detrimental to SERS signals.

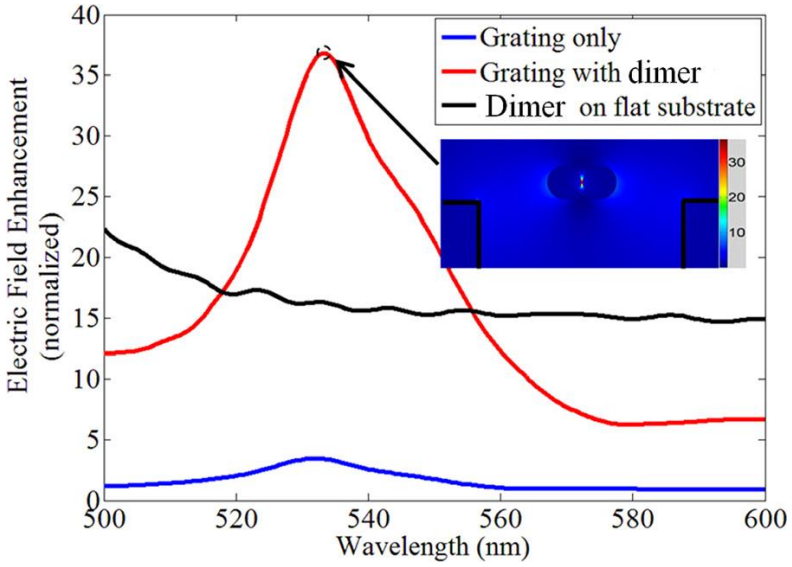

Figure 4.2: Electric field enhancement of different SERS substrate at wavelengths ranging from 500–600 nm.

We quantitatively investigated interactions between these two optical modes via numerical simulation, which can guide our experimental approach. Our simulation is based on a simplified model of one-dimensional silver nanoparticle chains assembled on

the surface of the GMR grating, and the SERS EF is calculated based on the well-known electromagnetic model presented in Section 1.3.1; i.e., the SERS enhancement is proportional to $|E|^4$. We need to consider two extreme cases for the actual SERS measurement. In the first case, the molecule concentration is extremely low such that there is only one molecule and multiple hot spots within the laser spot. Hence, the SERS EFs are determined by the electric field in a single hot spot, assuming that the molecule can be trapped within that specific gap. In the second case, the molecule concentration is relatively high such that there are multiple hot spots and each hot spot has attracted one molecule within the laser spot. Therefore, the total SERS signals are determined by $\sum|E_i|^4$, where E_i is the electric field in each hot spot. Assuming that the Raman signals from every hot spot can be collected, the total Raman signals are actually being used to evaluate the SERS substrate. We plot both the peak electric field in the gap (corresponding to the first case) and the total Raman signals (corresponding to the second case) with respect to the number of silver nanoparticles [figure 4.3], which indicates that there is an optimal number of silver nanoparticles that can provide the strongest SERS signals. We can see that as the number of nanoparticles increases from 1 to the optimal number (for maximum electric field, the optimal number is 6; and for maximum Raman signals, the optimal number is 7), both the peak electric field and the total Raman signals increase. For example, E/E_0 increases from 35 for a dimer with 2 silver nanoparticles to 80 for an array with 6 silver nanoparticles. One key point here is that the electric field distribution is not uniform in the gaps of the nanoparticle chain. The central gap

possesses a higher electric field than the edged gaps, as the top inset of figure 4.3 shows. The results from this simulation agree with those for silver nanoparticles in free space.[98] The addition of more nanoparticles will create more hot spots, and the total SERS signals will increase faster than $|E|^4$. However, after reaching the optimal number of 6, the electric field begins to decrease. Although the number of hot spots continues to increase, the total Raman signals quickly begins to diminish, as it is proportional to $|E|^4$.

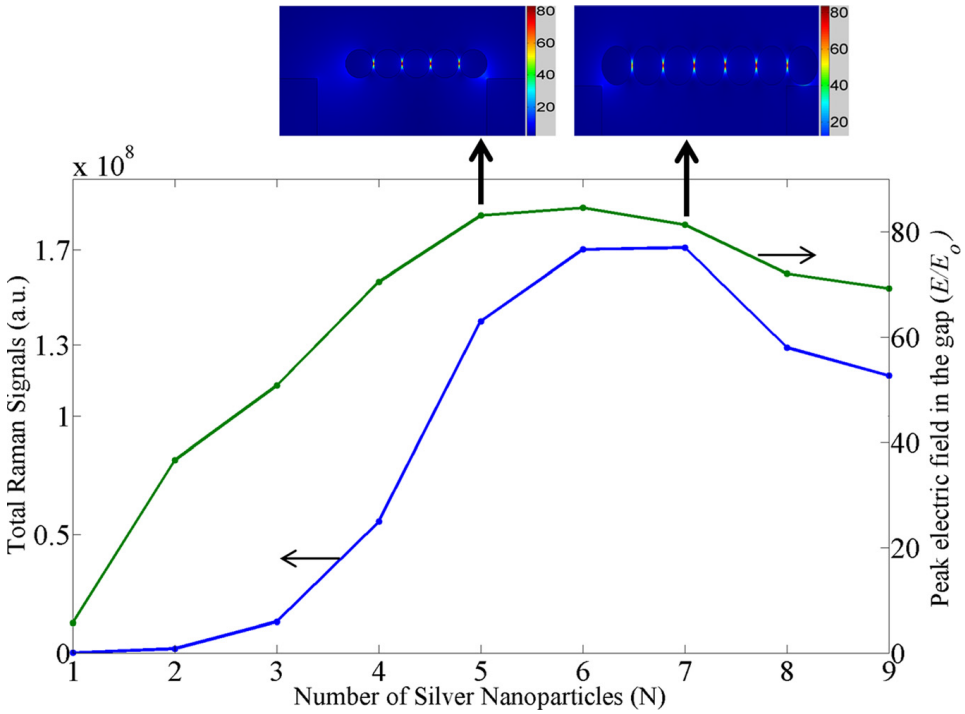

Figure 4.3: Total Raman signals and peak electric field in the gap as a function of the number of silver nanoparticles.

Two major fabrication steps are required for the design of SERS substrates. The SiO_2 nanotubes with densely assembled silver nanoparticles are fabricated via rational chemical synthesis and the process is briefly discussed here. First, silver nanowires with controlled diameters and lengths are fabricated via electro-deposition into nanoporous templates.[63] Second, the nanowires are used as templates for the synthesis of SiO_2 nanotubes. Then, a layer of SiO_2 with controlled thickness is uniformly coated on the outside surface of the nanowires. Next, the silver segments are selectively etched by nitric acid (8 M), resulting in hollow SiO_2 nanotubes. Finally, a large amount of silver nanoparticles are uniformly synthesized on the entire surface of the SiO_2 nanotubes with controlled sizes and gaps for SERS sensing. These nanotubes have been visualized by SEM. High-density silver nanoparticles are found to be uniformly coated on the outer surface of the nanotubes, as shown in figure 4.4(a). The SiO_2 nanotubes have average diameters of 450 nm and lengths of 8 μm. The silver nanoparticles are semi-spherical with diameters of 24.9 ± 7.7 nm, and the mean gap sizes between the neighboring nanoparticles are controlled to be less than 1 nm. Although the nanoparticles are densely arranged, overlap among them is rarely found. As a result, the entire surface of the nanotubes is active for SERS sensing due to the large number of "hot spots" from the densely arranged silver nanoparticles. In the next step, we fabricated the GMR Si_3N_4 grating by e-beam lithography and ion etching. A 300 nm silicon nitride layer is grown by low-pressure chemical vapor deposition (LPCVD) on a 1.5 μm field silicon oxide layer on top of a silicon wafer. The pattern of the GMR grating is written by e-

beam photolithography. Then, a 20 nm thick nickel layer is deposited by evaporation, followed by a lift-off process. The nickel pattern is used as a hard mask to etch the nitride layer to the buried oxide by reactive ion etching (RIE). Finally, the nickel residue is removed by chemical wet etching. Figure 4.4(b) shows the SEM picture of the fabricated Si_3N_4 grating.

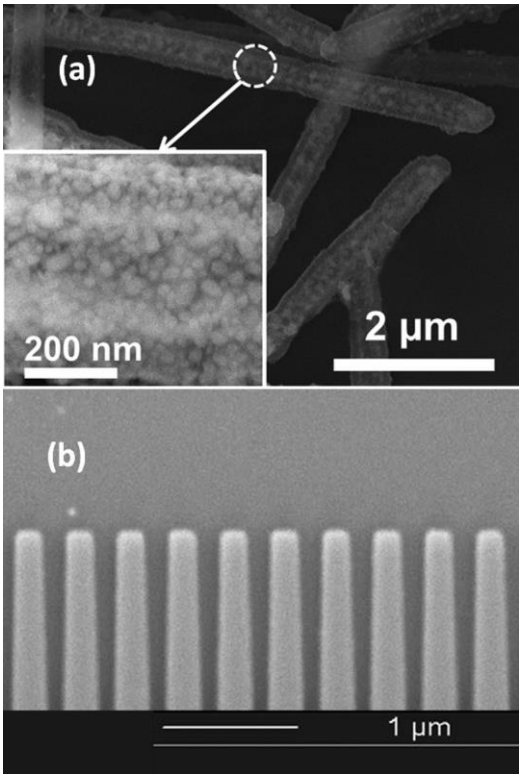

Figure 4.4: (a) SEM picture of the plasmonic-active SiO_2 nanotubes with densely assembled silver nanoparticles. (b) SEM picture of the Si_3N_4 GMR grating.

R6G, a standard SERS characterization dye, is selected as the detection probe. In the first experiment, we only use the GMR grating (without any plasmonic nanotubes) to

evaluate the grating effect. The R6G molecules are dispersed in ethanol with a very high concentration of 5 mM. A confocal Raman microscope equipped with a 532 nm laser is used for the Raman spectroscopic measurements. The integration time is set to 1 s. Raman signals of 5 mM R6G from the flat Si_3N_4 substrate (blue) and the Si_3N_4 GMR grating (green) are plotted in figure 4.5. Although the measured Raman spectra possess a great deal of noise due to the extremely weak signals, the peak Raman shift at 1370 cm^{-1} is enhanced by 3.2 times, which clearly demonstrates the electric field enhancement of the GMR grating.

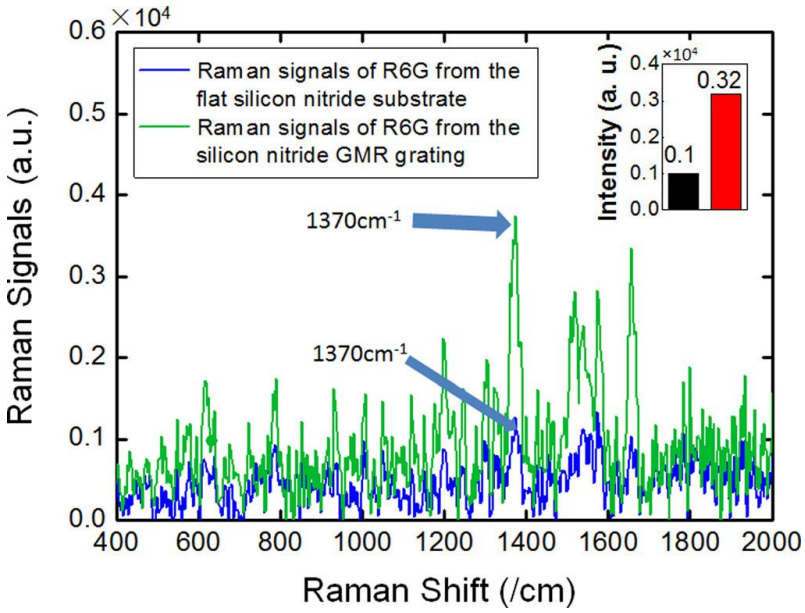

Figure 4.5: Measured 5 mM R6G Raman spectra from the flat Si_3N_4 substrate and from the Si_3N_4 GMR grating (with no plasmonic nanotubes in both cases).

In the second experiment, we included the plasmonic-active SiO_2 nanotubes for SERS characterization. The R6G concentration is reduced to 1 μM, which can still form

a monolayer that can trap molecules in every hot spot. The laser spot size is 2 μm, which can be focused on any specific position of a single nanotube along its longitudinal direction. Within the laser spots, there are approximated 1000 hot spots that can contribute to Raman sensing. In each measurement, there is only one plasmonic-active SiO_2 nanotube within range of the laser spot. Figure 4.5 shows the measured 1 μM R6G SERS signals from a SiO_2 nanotube on the flat Si_3N_4 substrate (blue) and from a SiO_2 nanotube on the Si_3N_4 GMR grating (green), respectively. The inset of figure 4.5 shows the $1000\times$ optical microscope image of the Si_3N_4 grating with sparsely dispersed plasmonic-active SiO_2 nanotubes. For various signature Raman shift peaks between $500/cm^{-1}$ to $1800/cm^{-1}$, the absolute intensity of the Raman signals is simultaneously enhanced by $8\sim10$ times. Because GMR grating increases the local electric field of the excitation light, it is not surprising to find that the noise signals that contain fluorescence and Raman spectra of various trace chemicals also increase with the electric field,[76] and are thus amplified. Here, we note that the noise from fluorescence is proportional to E^2 and that the noise from Raman signals is approximately proportional to E^4. As a result, both Raman signals from R6G and their noise can be enhanced by the GMR grating. Additionally, our characterization shows that EFs are constant and stable across the whole surface of the plasmonic-active SiO_2 nanotube. The absolute SERS EFs from the combined GMR grating and SiO_2 nanotubes are largely determined by the plasmonic enhancement from the nanoparticles, which can be tuned by their diameters and gap sizes, because the LSPPs can provide a much stronger electric field enhancement

than the GMR grating. The interesting phenomenon we observe here is that the GMR grating can provide 3.2× EFs on a pure dielectric substrate [figure 5.5], whereas 8 ~ 10× SERS EFs with plasmonic nanotubes is observed [figure 4.6]. This difference is possibly due to the measurement errors of extremely weak Raman signals without plasmonic nanotubes.

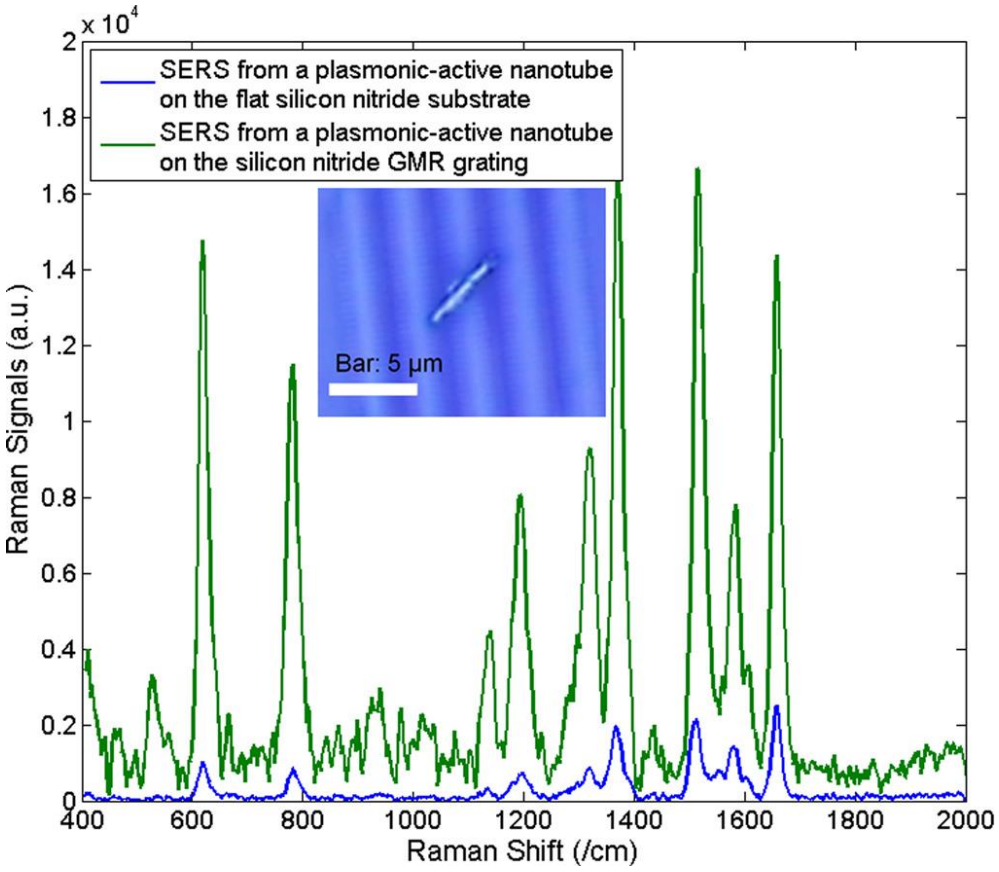

Figure 4.6: Measured 1 μM R6G Raman spectra from the silica nanotube on the flat Si_3N_4 substrate and from the silica nanotube on the GMR grating.

In summary, we have numerically investigated and experimentally demonstrated a SERS substrate composed of Si_3N_4 GMR grating with plasmonic-active SiO_2 nanotubes, where densely grown silver nanoparticles provide a large number of "hot spots" for SERS sensing. Such rationally designed SiO_2 nanotubes can deliver an optimal amount of metallic nanoparticles to the Si_3N_4 grating to achieve sufficient LSPPs without significantly dampening the GMR modes. Experimental measurement of R6G confirms that the SERS substrate can provide constant and stable EFs of $8 \sim 10$ across the entire nanotube surface, in addition to the existing SERS effect. As a new enhancement mechanism to SERS technology, the GMR grating coupled with surface plasmonic resonance (SPR)-active nanotubes demonstrated herein proves that resonant photonic devices can indeed serve as an effective substrate to increase the sensitivity of Raman spectroscopy. Such highly sensitive SERS substrates will have significant potential in early disease diagnostics, chemical detection and environmental protection.

4.2 NEAR-FIELD ENHANCEMENT

In addition to the mechanism of enhancement from nanophotonic devices, the SERS EF of the nanocapsules can also be enhanced by the near-field effect. In the following study, we designed a hollow plasmonic magnetic nanotube structure, which has Ag nanoparticles coated on both the inner and outer surfaces. Through detailed SERS characterization and theoretical simulation, it was found that an additional >2 times SERS enhancement factor can be achieved, which is mainly attributed to the near-field effect between the inner and outer layer Ag nanoparticles and the additional hotspots.

4.2.1 Experimental results

To fabricate such plasmonic magnetic nanotube structures, a rationally designed four-step approach has been used: (1) multi-segment Ag/Ni/Ag (3/3/3 μm) nanowires were electrodeposited as growth templates for silica nanotubes (Scheme 4.1(a) & Figure 4.7a); (2) a layer of silica, with controlled thickness of 70 nm, was uniformly plated on the outer surface of the Ag/Ni/Ag nanowires (Scheme 4.1(b)) via hydrolysis of tetraethyl orthosilicate[26,67,68]; (3) the Ag segments were selectively etched, resulting in the hollow silica nanotubes with magnetic Ni embedment (Scheme 4.1c & Figure 4.7(b)); and (4) plasmonic Ag NPs were uniformly coated through PVP-assisted catalysis[99] on the inner and outer surfaces of the nanotubes with optimized particles and junction sizes (Scheme 4.1d & Figure 4.7(c)).

Scanning electron microscopy (SEM) images show that hollow nanotubes with embedded cylindrical solid segments were successfully synthesized (figure 4.7). Energy dispersive X-Ray spectroscopy (EDS) confirmed that the cylindrical solid was Ni (figure 4.8). Arrays of Ag NPs were uniformly distributed over the entire outer surface of the nanotubes. The Ag NPs also grew on the interior surfaces of the nanotubes as shown in the SEM images (figure 4.7 (c)) obtained by cross-sectional focused ion beam (FIB) milling (figure 4.7d). The Ag NPs were semi-spherical and densely arranged, yet overlapping NPs were rarely found.

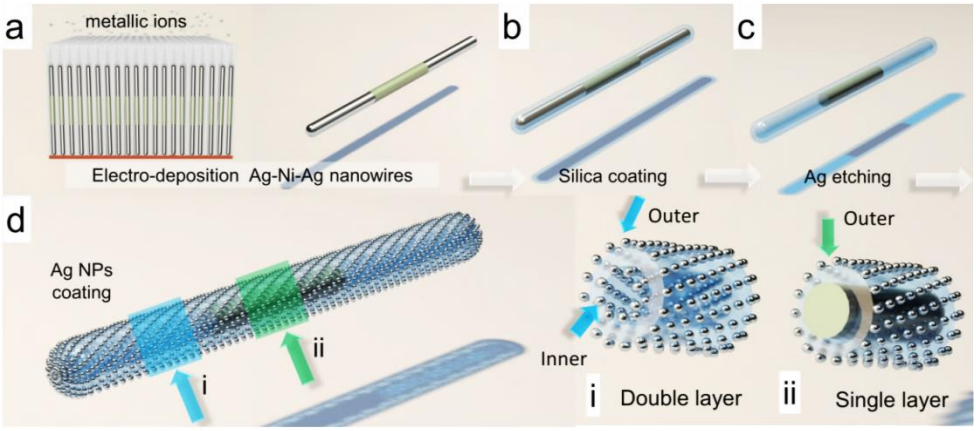

Scheme 4.1: Schematic of the fabrication process of the PM nanotubes. (a) Electrodeposition of Ag/Ni/Ag nanowires. (b) Silica shells coating. (b) Etching of the Ag segment to obtain hollow nanotubes with solid Ni embedment. (d) Synthesis of Ag NPs on both the inner and outer surfaces of nanotubes. (Inserts are cross-sectional views of (i) the hollow segment and (ii) the Ni embedded segment of the PM nanotubes.)

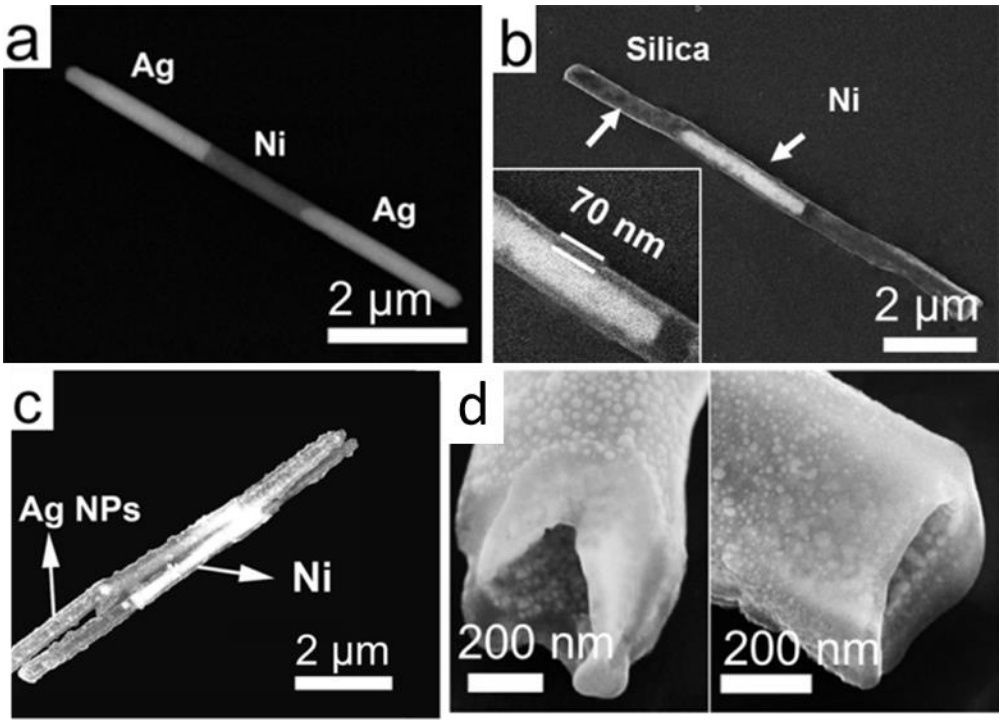

Figure 4.7: Scanning electron microscopy images of (a) multisegment Ag/Ni/Ag nanowires, (b) silica nanotubes embedded with Ni nanomagnets, (c) silica nanotubes with Ni segments and surface-coated Ag NPs, and (d) cross-sectional images of nanotubes obtained by FIB milling show the nanotubes are hollow with Ag NPs on both the inner and outer surfaces.

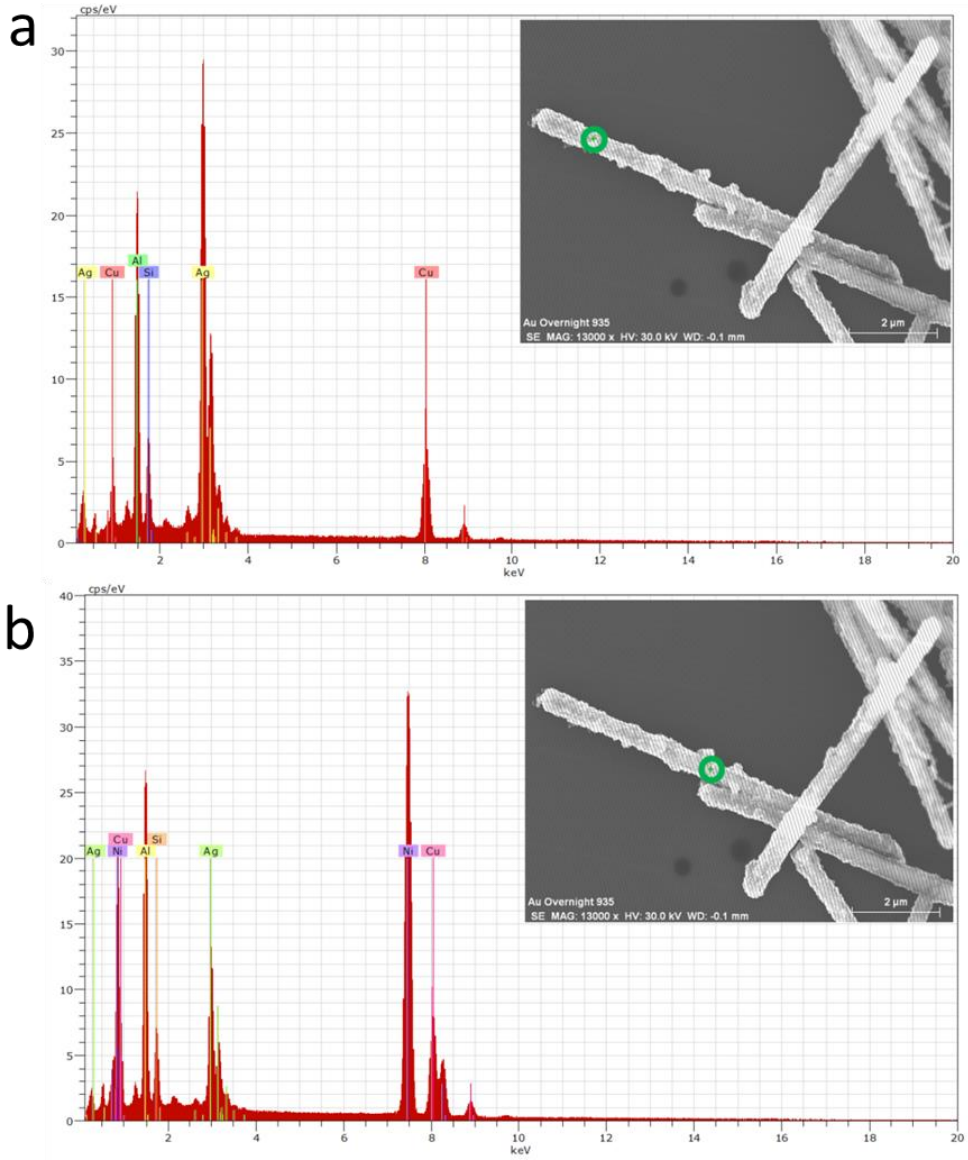

Figure 4.8 (a) EDS shows the ends of the nanotubes consist of Ag and silica. (b) EDS shows the center portion of the nanotubes consists of Ni, Ag and silica.

Notably, we found that Ag NPs not only grew on the outer surface of the nanotube, but also on the interior surface of the nanotube, as shown in the SEM images of cross-sections obtained by FIB milling (figure 4.7d). Therefore, there were double-layered Ag NPs on the hollow parts of the PM nanotubes and single-layered Ag NPs on the solid part of the nanotubes (scheme 4.1 insert). Because of the difficulties associated with characterization, we cannot directly measure the size and distribution of the inner layer Ag NPs. However, the effect of the inner surface coating of Ag NPs can be known from SERS measurements. When a laser beam is scanned along a single nanotube with a 70 nm thick silica coating, the hollow segments of the nanotubes with double-layer Ag NPs exhibited more than two times the SERS intensity than those from single-layer Ag NPs on the outer surface of the Ni embedded section of nanotubes (figure 4.9(a)). Similar results were also observed when we replaced the Ni segment with Pt (figure 4.9(b)).

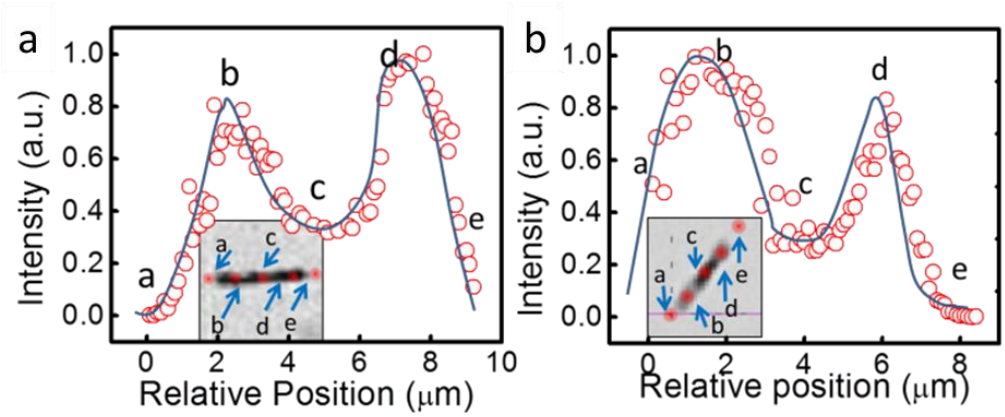

Figure 4.9: (a) Ni embedded and (b) Pt embedded hollow nanotubes.

The experimental details are as following:

A Raman microscope equipped with a high precision motorized stage (resolution: 50 nm) was used for SERS characterization. A 532 nm laser was employed as the Raman excitation source. In the Raman experiments, we first dispersed the nanotube samples on a glass slide, dried and incubated them in 1 mM BPE (ethanol solution) for 10 min, before rinsing them with pure ethanol to remove excess molecules.

The laser was then focused on one end of a nanotube with a spot size of 1 μm and scanned slowly from one end of the nanotube to the other, during which time Raman signals were simultaneously collected by a spectrometer coupled to the microscope. The step size of the laser was set at 100 nm for a high spatial resolution. The integration time of the Raman spectrum was 0.6 seconds. Using this approach, a series of SERS spectra along a nanotube could be readily obtained. We plotted the peak intensity of the Raman signal of BPE at 1200 cm^{-1} as a function of the scanning distance on the nanotubes [figure 4.9]. The results clearly indicate that the Raman signals received more than two times enhancement from the dual-sided Ag NPs on the hollow sections of nanotube (i.e., on the two ends) than from the single-sided Ag NPs on the solid sections (i.e., in the center).

4.2.2 Simulation and discussion

To understand how the dual-side Ag-coated hollow nanotubes can further enhance SERS than the single-side Ag-coated nanotubes with solid embedment, we performed

numerical simulations with the RF module from COMSOL 3.5a. In our modeling, a three-dimensional (3-D) silica nanotube is constructed (illustrated in scheme 4.1(d) & inserts): the inner cylinder radius is 150 nm, and the shell thickness is 70 nm. The densely coated Ag NPs are simplified by a 2-D conformal array attached to the outer and inner surfaces of the silica nanotubes. The Ag NP diameter is 25 nm and the gap between them is 2 nm. The silica nanotube is placed on top of a glass substrate, and is excited by a surface normal Gaussian beam with a diameter of 1 μm and a wavelength of 532 nm. The polarization direction is perpendicular to the axis of the cylinder. Table 4.1 lists our simulation results corresponding to our experimentally measured devices, and Figure 4 shows the cross-sectional views of the electric field distribution of the four devices as listed in table 4.1.

Table 4.1: Simulation parameters for plasmonic magnetic nanotubes, where D is the particle size.

	Outer layer	**Inner layer**	**Ag NPs**
Simulation 1	Ag NPs	Hollow (air)	D=25 nm, gap=2 nm
Simulation 2	Ag NPs	Ag NPs	D=25 nm, gap=2 nm
Simulation 3	Ag NPs	Pt	D=25 nm, gap=2 nm
Simulation 4	Ag NPs	Ni	D=25 nm, gap=2 nm

In figure 4.10(a), we find, rather surprisingly, that the hotspot with maximum electric field enhancement is actually at the bottom of the nanotube and not at the top. This is because the hotspot at the bottom of the nanotube is surrounded by high-index silica, whereas the other hotspots have only one side in contact with silica. (The other side is exposed to low-index air.) Additionally, the inter-particle coupling through the NP chain at the outer surface enhances the electric field at the bottom[100]. Comparing figures 4.10(a–b), we are able to clearly deduce the contribution of the inner layer Ag NPs; specifically, the presence of the inner layer not only adds more hotspots for SERS sensing, but it also significantly increases the intensity of the hotspots in the outer layer NPs, which is due to the near-field effect [101] of inter-layer coupling between NP chains in the inner and outer surfaces of the nanotubes. When the air core is filled with Pt, which has no surface plasmonic resonance at visible wavelengths, we observed interesting phenomena; first, the EF of the hotspots on top of the nanotube is enhanced approximately 2×, which is due to the reflected light from the Pt core; second, the hotspots at the bottom of the nanotube are significantly reduced because almost no light can penetrate the Pt core to excite the surface plasmons. Moreover, the inter-particle coupling through the NP chain can be weakened by evanescent field absorption of Pt. Similar electric field enhancement is observed in Ni-filled nanotubes as well.

If we assume there are enough molecules so that every hotspot can contribute to the SERS measurement, we can calculate the total SERS signals by $\sum|E_i|^4$, where $\boldsymbol{E}_{\mathrm{i}}$ is the electric field in each hotspot. The total SERS signals of these four devices are 0.8×10^5,

2.5×10^6, 1.4×10^5 and 1.3×10^5 a.u., respectively. It is seen that device 2 will be able to provide higher SERS signals than devices 3 and 4 by more than 10×. However, in reality, the SERS signals from hotspots at the bottom to the nanotubes are more difficult to collect due to NP scattering. Experimentally, we obtained differences of more than 2× (figure 4.8). The comparison of single-side and dual-side Ag NP coated nanotubes is summarized in table 4.2.

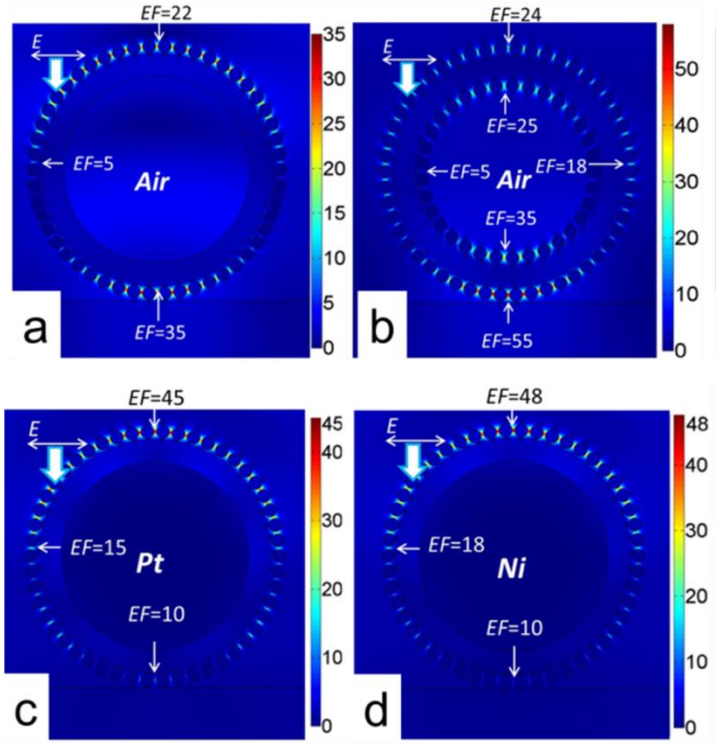

Figure 4.10: (a–d) Simulation results show the cross sectional views of the optical induced electric field enhancement of the four devices listed in Table 4.1.

Moreover, we note that the thickness of silica also affects the enhancement of SERS. We observed a near-field enhancement effect on nanotubes with silica coating

ranging from 70 to 150 nm. However, when the thickness of silica was increased to 300 nm, the near-field enhancement effect was not observed, which may be attributed to the reduced plasmonic coupling between Ag NPs across the silica shell.

Table 4.2: Comparison of nanocapsule sensors with single- and dual-sided coated Ag NPs.

	Single-sided Ag NPs	**Dual-sided Ag NPs**
Substrate for Ag NPs	Silica coated solid nanowire segments (Ni or Pt)	Hollow silica nanotubes
Ag NPs coating condition	Same conditions as described in the main text	
Ag NPs on the outer surface of silica	Same characteristics: particle and junction size	
Ag NPs on the inner surface of silica	none	large arrays exist as revealed by FIB/SEM, the particle size and junction cannot be accurately determined
SERS testing condition	Same condition as described in the supporting information S5	
SERS enhancement	EF=7.2×10^{9} (8× sample on the Ni embedded sections)	More than two time stronger than that from single-sided Ag NPs

Chapter 5: Robotization of SERS Nanosensors**

5.1 INTRODUCTION

Robotization of nanoentities is highly desirable for biological applications, such as biochemical delivery, single cell sensing, and analysis. However, most of the state-of-the-art sensors are in a passive and static fashion. In recent work, we employed the electric tweezers technique and magnetic field to robotize the SERS sensitive nanocapsules for location predicable sensing, living cell bioanalysis, and tunable biochemical release.

5.2 ELECTRIC TWEEZERS

Ordinary tweezers are a mechanical tool that can physically hold a small object and move it from one location to another by hand. However, holding a very small object, such as a nanowire, via a mechanical device is not feasible. Optical tweezers and magnetic tweezers have been invented in recent years to "hold" certain nanoentities. In the former approach, a focused laser beam holds a dielectric particle in the "waist" of the beam profile, while in the latter approach a magnetic field gradient holds a paramagnetic particle. An entity of interest (e.g., DNA) can be attached to a dielectric particle or a paramagnetic particle and can be held in place by the optical or the magnetic tweezers,

** Portions of this chapter have been previously published in X. Xu, K. Kim, H. Li, D. L. Fan, Advanced Materials, 24, 5516 (2012); X. Xu, H. Li, D. Hasan, R. Ruoff, A. X. Wang and D. L. Fan, Advanced Functional Materials, 23. 4332 (2013); Fan, D. L.; Zhu, F. Q.; Cammarata, R. C.; Chien, C. L. Nano Today, 6, 339 (2011); X. Xu, C. Liu, K. Kim and D .L. Fan. Advanced Functional Materials, 24, 4843 (2014)

respectively. As optical and magnetic tweezers hold the particle by trapping it in an electromagnetic field, there is no net force delivered to the particle that would cause it to move. Instead, a particle is "moved" by mechanically moving the stage. It would be far more versatile if one could "hold" *and* apply a force to manipulate small entities in suspension and, even better, perform it with no moving parts. Electric tweezers can accomplish this feat.

Electric tweezers enjoy certain distinct advantages compared with their magnetic and optical counterparts. By suitable functionalization, a small entity in suspension can be made to carry either positive or negative charge to be responsive to a DC electric field. For electrically neutral entities, one can use an AC electric field to induce an effective electric dipole moment and manipulate them with the electric field gradients (*EFG*). Unlike optical and magnetic tweezers, which require extensive instrumentation, electric tweezers use a relatively simple approach in which voltages are applied to strategically-designed electrodes that can produce the necessary DC and AC electric fields. Finally, there are no mechanically moving parts in electric tweezers except for the small entities being manipulated.

Electric tweezers are based on combined DC and AC electric fields for precision orientation and the transport of metallic nanowires in aqueous suspension, the fundamentals of which have been reported elsewhere [60,62-65,102].

Briefly, in a combined DC and AC electric (***E***) field, a longitudinal nanoparticle can be transported by the DC ***E*** field due to electrophoretic force and aligned by the AC

E field due to dielectrophoretic force. The transport and alignment of the nanoparticle can be controlled completely and independently by the DC and AC ***E*** fields, respectively. Applying the combined ***E*** fields in both the X and Y directions with controlled duration, longitudinal nanoparticles, such as nanowires, can be readily transported along prescribed trajectories on a 2-D surface with a precision of at least 150 nm.

5.2.1 Orientation controlled transportation

Uniform AC and DC ***E*** fields were established in a quadruple microelectrode chip with two pairs of parallel-electrodes separated at a distance of 500 μm. Nanocapsules suspended in D.I. water were dispersed at the center of the quadruple electrodes. The nanocapsules can be readily transported parallel [figure 5.1(a), AC//DC] or perpendicular to their orientations [figure 5.1(b), AC⊥DC], which is similar to earlier manipulations of Au nanowires[60,63,64], by applying electric tweezers with a combined AC (15 V, 20 MHz) and DC voltages (−2.5V to +2.5V) on the quadruple electrodes. The transport speed linearly increased with the applied DC voltages for both orientations and reached approximately 80 μm/second at 2.5 V in vertical transport. We noticed that the Ag/Ni/Ag nanorod cores in the nanocapsules played a critical role in steering the transport orientations. After their metallic cores had been etched away,[103] the hollow nanotubes were transported by a DC ***E*** field; however, the orientations of the nanotubes were uncontrollable by the AC ***E*** field due to weak polarization and low alignment torques of the insulating silica nanotubes in an AC ***E*** field [figure 5.2]. Therefore, it is essential to

have the metallic Ag/Ni/Ag rod in the Raman nanosensors to facilitate steering of the orientation.

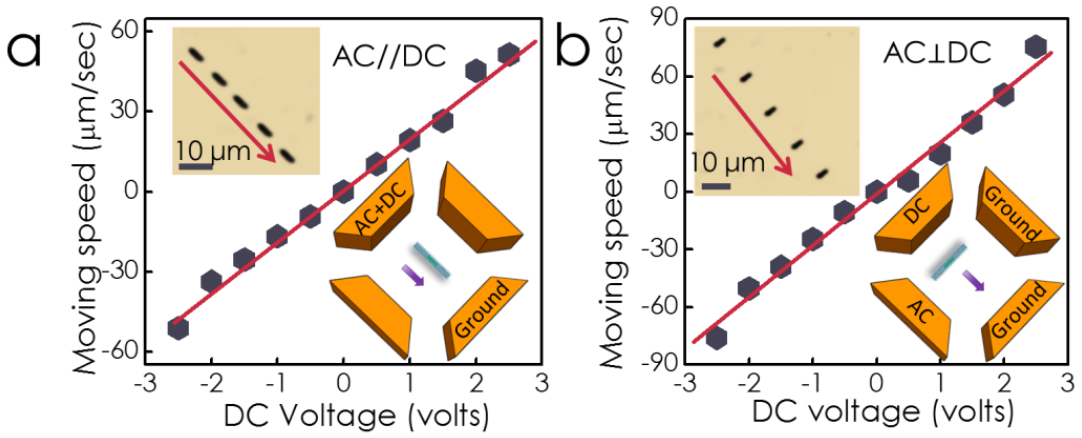

Figure 5.1: AC and DC configurations of quadruple electrodes for the manipulation of nanocapsules. The nanocapsules are aligned in the direction of the AC ***E*** field and transported in the direction of the DC ***E*** field. Nanocapsules were transported with controlled speed and orientation using "electric tweezers", (a) parallel (AC//DC) and (b) perpendicular (AC⊥DC) to their own alignment directions, as shown in the overlapped optical images. The transport speed is linearly proportional to the applied DC voltage.

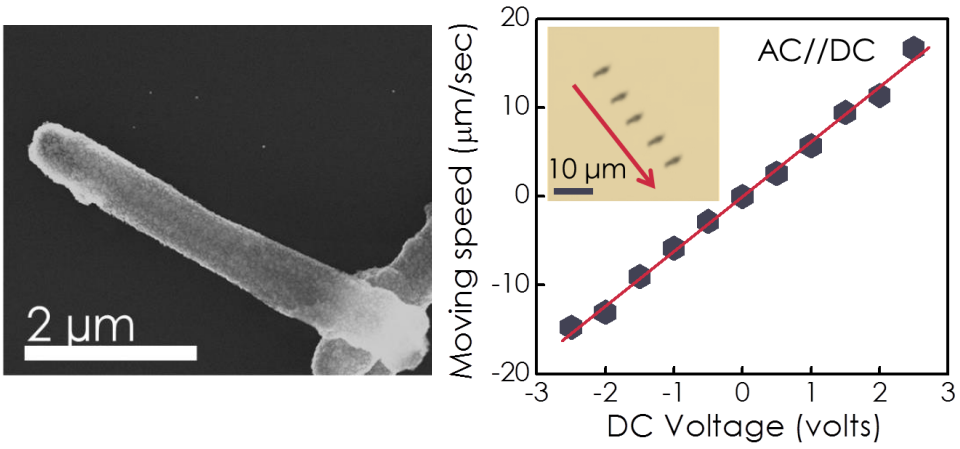

Figure 5.2: (a) A SEM image of a hollow plasmonic nanotube. (b) Hollow nanotubes being transported by a DC ***E*** field. The orientations of the nanotubes could not be controlled by the AC ***E*** field due to weak polarization and low alignment torques of the insulating silica nanotubes in an AC ***E*** field. For example, with AC//DC, the nanotubes could not be aligned parallel to the moving direction.

5.2.2 Controlled Rotation

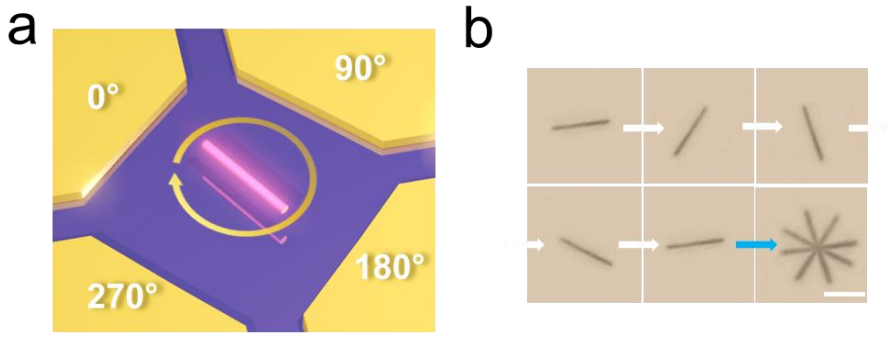

Figure 5.3: (a–b) Four 90° phase-shifted AC voltages applied on a quadruple microelectrode for the rotation of nanowires.

The electric tweezers is a versatile tool; it not only controls the orientation and transport of longitudinal nanoentities, it can also rotate longitudinal nanoentities.[65] When four AC voltages with sequential 90° phase shifts were applied on quadruple microelectrodes, nanowires that were placed in the central region of the microelectrodes could be compelled to rotate because of the electrical interactions [Figure 5.3].

When a longitudinal nanoentity, such as a nanowire, in a liquid of permittivity ε_m rotates in an electric field ***E***, the electric torque can be given as:

$$|T_e| = | p \times E | = \frac{2\pi}{3} r^2 l \varepsilon_m Im(K) E^2$$

where ***p*** is the induced dipole moment of a nanowire of radius *r* and length *l*, ε_m is the permittivity of the suspension medium, and *Im(K)* is the Clausius-Mossotti factor.

However, the viscous torque (T_η) received by the rotating nanowires balances the electric torque (T_e), i.e., $T_\eta + T_e = 0$. The rotational speed of nanowires can be expressed as:

$$\Omega = -C\frac{\varepsilon_m r^2 E^2}{\eta l^2}\mathrm{Im}(K)$$

where η is the viscosity and C is a constant.

From the above equation, we see that the rotational speed can be controlled by the voltage of the AC electric field with a $\Omega \sim V^2$ dependence. By using such a rotating electric field, we can readily rotate the one-dimensional SERS nanosensors for various applications, e.g., controlled biochemical release. The detailed study of the rotation of SERS nanosensor will be described in section 6.3.

5.3 MAGNETIC FIELD MANIPULATION

In addition to the nanotubes being plasmonically sensitive, the unique structures also offered tunable magnetic properties for controlled manipulation. The magnetic anisotropy of the Ni segment is dominated by its shape anisotropy[104-106], as opposed to its weak crystalline anisotropy. When the aspect ratio of the Ni segment is high, (e.g., 10/1; Ni length 3 um, diameter 300 nm), the anisotropic direction and the magnetic easy axis is along the nanotube long axis as measured by Vibrating Sample Magnetometry (VSM) (figure 5.4(a)). A hysteresis loop along the magnetic easy axis demonstrates higher magnetic remanence and squareness than those measured perpendicular to the nanotubes. When the aspect ratio of the Ni segments is below 1, (e.g., a stack of thin Ni disks with

diameters of 300 nm and thickness of 30 nm), magnetic anisotropy is generally transverse to the nanotubes with essentially zero remanence due to the anti-parallel coupling of the magnetizations in neighboring nanodisks (figure 5.4(b)). This fascinating way of controlling the magnetic anisotropy has been vividly demonstrated by manipulating nanotubes in suspension with a magnetic field. As shown in figure 5.4, nanotubes with magnetic anisotropy along the long axis align with the magnetic field during transport, but those with transverse magnetic anisotropy align perpendicular to the magnetic field. The transport speed was 2–7 μm/s, which can be controlled by the magnetic field gradient.

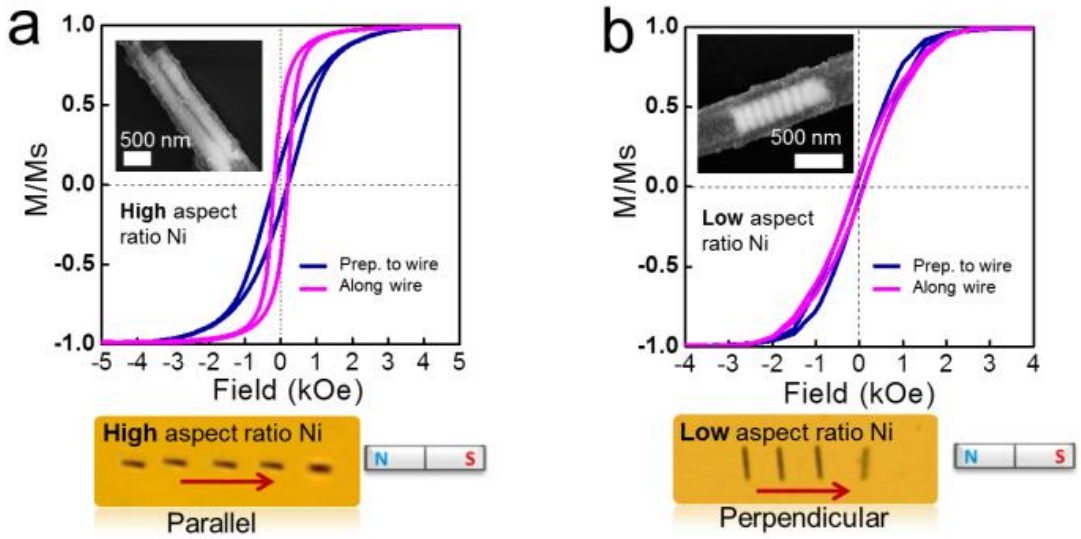

Figure 5.4: Magnetic anisotropy can be readily tuned by the aspect ratio of magnetic Ni embedment as shown in the hysteresis loops for Ni with (a) high and (b) low aspect ratios, respectively. The overlapped images show nanotubes transported parallel or perpendicular to the magnetic field due to their unique anisotropies. The speed of nanotubes is 5–7 μm/sec.

Chapter 6: Applications of robotized SERS nanosensors[††]

6.1 LOCATION PREDICABLE BIOSENSING

Different from most previous reports of SERS sensing nanostructures, our Raman nanocapsule sensors are designed for facile assembly at designated locations. Previously, seek-and-find efforts are generally required for SERS sensing devices due to the randomness of hotspots. These efforts have greatly hindered the development of SERS for realistic applications. It is highly desirable to assemble the hot-spots at specific locations for location-predictable biosensing. Previously, substantial efforts were exerted to address this problem; [28,29,36] however, it remains a daunting task to obtain Raman sensors with reliable spatial accuracy. Here, we present how the strategic design of nanocapsules can facilitate the rational assembly of hot-spots for location-predictable Raman sensing using electric tweezers, our recently invented and contactless nanomanipulation technique.

As shown in Section 5.2.2, the nanocapsules can be successfully transported in the microelectrodes. The next task is to assemble the nanocapsules on arrays of nanomagnets for location predictable SERS sensing. How do we assemble these nanocapsules for location predicable sensing? Here, we leveraged the electric tweezers as

[††] Portions of this chapter have been previously published in X. Xu, K. Kim, H. Li, D. L. Fan, Advanced Materials, 24, 5516 (2012); X. Xu, H. Li, D. Hasan, R. Ruoff, A. X. Wang and D. L. Fan, Advanced Functional Materials, 23. 4332 (2013); X. Xu, K. Kim, D. L. Fan. Angewandte Chemie International Edition, in press (2014) and K. Kim, X. Xu, J. Guo and D. L. Fan. Nature Communications, 5, 3632 (2014)

discussed in Section 5.2.2 and the unique magnetic Ni embedment in the Ag/Ni/Ag core of the nanocapsules to assemble an ordered plasmonic nanosensor array on pre-patterned nanomagnets, as shown in Scheme 6.1.

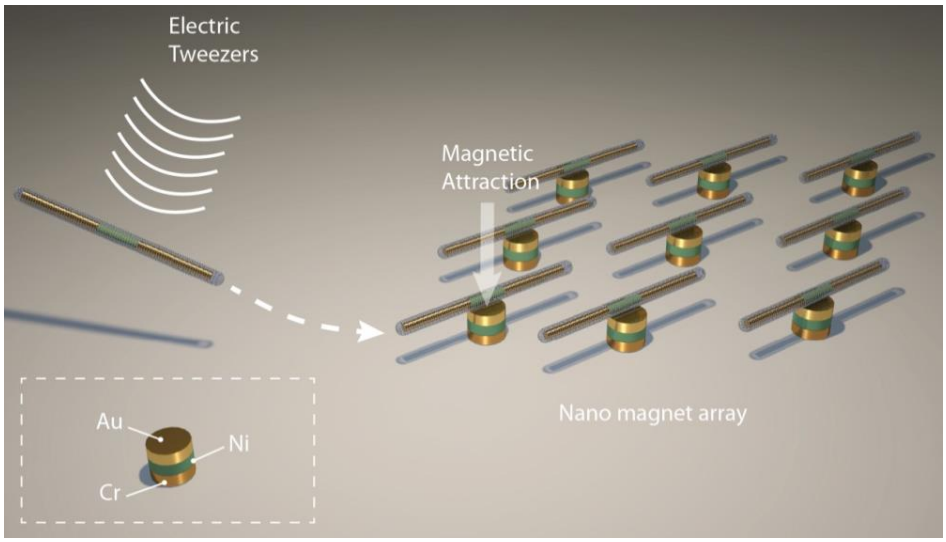

Scheme 6.1: With the electric tweezers, nanocapsules can be transported and assembled onto a pre-patterned array of nanomagnets by utilizing the magnetic attraction force between the Ni segments in the nanocapsules and the magnetic layers inside the nanomagnets.

At the center of the quadruple microelectrode, we fabricated a 3×3 nanomagnet array through standard e-beam lithography [figure 6.1(a)]. Each nanomagnet with a diameter of 1 μm actually consists of a tri-layer structure: a 6 nm Cr adhesion layer on the substrate, a 100 nm Ni layer providing magnetic fields, and a 100 nm Au layer for tuning the magnetic interaction force.

By programming the AC and DC *E* fields in both the X and Y directions, we have forced the nanocapsules to move along a prescribed trajectory, such as "steps", with orientations either parallel [figure 6.1(b)] or perpendicular [figure 6.1(c)] to their transport directions. When nanocapsules were maneuvered into the vicinity of nanomagnets by the electric tweezers, the magnetic attraction force securely anchored the nanocapsules on the top of the nanomagnets. The magnetic force was between the nickel segments in the core of the nanocapsules and the Ni layer in the patterned nanomagnets on the chip. The manipulation of the nanocapsules was so versatile and precise that we easily maneuvered a nanocapsule to pass by a few neighboring nanomagnets and anchored it on a nanomagnet at the center of the array and other locations [figure 6.1(d) and 6.1(e)]. In this manner, we have assembled an array of nanocapsules on top of nanomagnets as shown in figure 6.1(f), where the bright circles indicate nanomagnets.

Finally, from the assembled nanocapsule arrays, we successfully detected SERS of various chemicals, including R6G, methyl blue and BPE, and realized location predictable biochemical sensing by design, as shown in figure 6.2. Note that the probability of single-molecule detection increases with the number of hot-spots on the nanocapsules excited by the laser. This outcome can be readily achieved by increasing the size of the laser spot, by having prescribed scanning along the nanocapsules, and even by trapping multiple nanocapsules on a single nanomagnet.

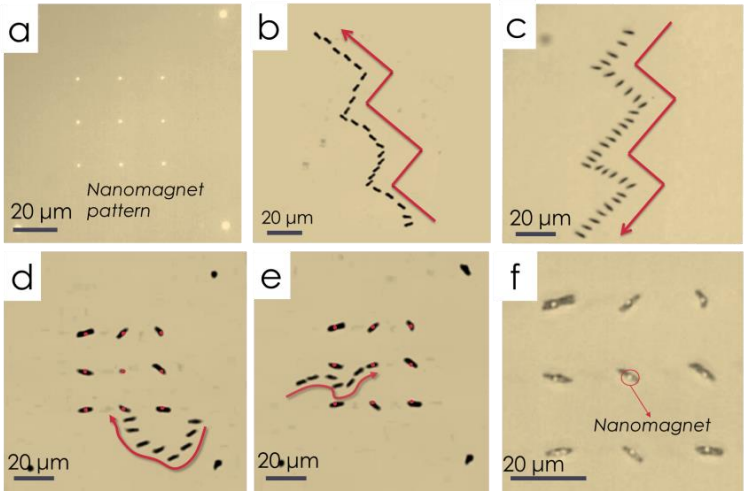

Figure 6.1: Nanocapsules can be precisely transported and assembled on the nanomagnets with electric tweezers. (a) A 3×3 array of nanomagnets fabricated using E-beam lithography. With combined AC and DC E fields applied in both the X and Y directions, the nanocapsules were transported along prescribed trajectories such as "stairs" with (b) parallel and (c) transverse orientations. (d, e) Overlapped snapshots show the assembling process of a nanocapsule, where the nanomagnets are highlighted in red. The nanocapsules can be maneuvered and positioned at designated positions, showing the high flexibility and precision of the assembling process. (f) An assembled 3×3 nanocapsules array. The bright nanomagnets are in the center of the nanocapsules, indicating that the attachment is due to the magnetic attraction between the Ni segments in the center of the nanocapsules and the magnetic layers in the patterned magnets. All of the images were taken by reflective optical imaging.

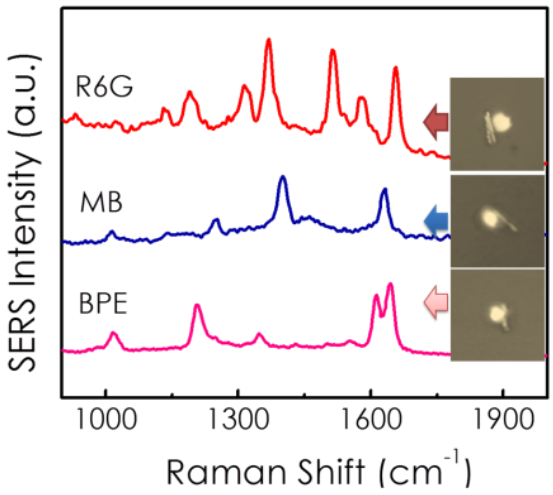

Figure 6.2: Various chemicals were detected from assembled nanocapsules, including R6G, methylene blue, and BPE.

6.2 LIVE CELL BIOANALYSIS

Although single complex biological samples can be investigated with standard Raman microscopy, a detailed investigation of specific components on the cell surface is not possible with this approach[107]. In our work, we demonstrated the utility of the bifunctional nanotubes in revealing the membrane composition of a single Chinese Hamster Ovary (CHO) cell amidst many. We chose CHO cells because they are widely used in biological research, especially in studies of genetics, toxicity screening, gene expression, and the expression of recombinan proteins. Here, leveraging the unique bifunctionality of the nanotubes, we can precisely transport a nanotube to a specific living CHO cell amidst many and detect its membrane chemistry using SERS spectroscopy.

CHO cells (ATCC Inc.) were cultured in RPMI medium (Invitrogen) supplemented with 10% Fetal Bovine Serum and 1% penicillin-streptomycin (Invitrogen). The cells were maintained in a humidified 37°C, 5% CO_2 incubator. Before the experiment was conducted, the CHO cells were washed by a phosphate buffered saline (PBS) solution, followed by the addition of nanotubes (dispersed in PBS).

In the experiment, a plasmonic magnetic nanotube (SEM figure 4.7(c)) was transported and aligned in the direction of the magnetic field and precisely laid on the membrane of a CHO cell (overlapped images in figures 6.3(a–b)). From the SERS spectra (figure 6.3(c)), which were recorded from the nanotube with an integration time of 5 s, shows strong characteristic peaks of lipids[107-109]. The peak position 1511 cm^{-1} can be assigned to amide II, which is from protein (blue bar in figure 6.3(c)). This result reveals that the cell membrane in contact with the nanotube consists mostly of lipids and some protein molecules, which is consistent with real cell membrane composition[107]. Without nanotubes, no Raman signals could be detected from the cell, clearly demonstrating the highly desirable bifunctionality of the nanotubes for precision and ultrasensitive single-cell bio-analysis. This technique is generally applicable to any adhesive cells. It can be readily applied to hamster cells as well as to mouse or human cells.

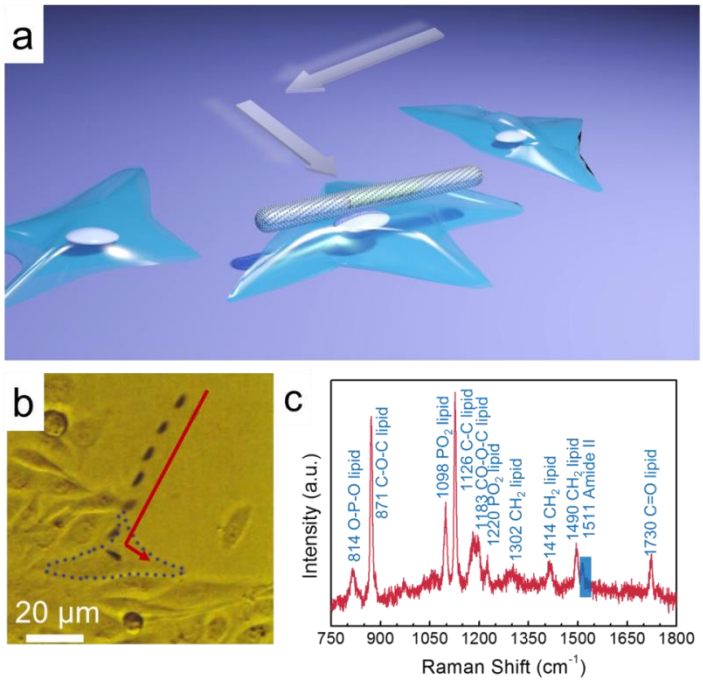

Figure 6.3: (a, b) The transport of a nanotube to a single CHO cell amidst many cells. (c) SERS spectrum from the CHO cell membrane is dominated by contributions due to lipids. A few peaks can be assigned to protein (blue bar).

6.3 CONTROLLED BIO-CHEMICAL RELEASE

The great potential of nanoparticles for biosubstance delivery has intrigued considerable research interest because of their controllable geometry, chemistry, and surface functionality[110]. Various nanoentities were explored for in-vivo drug delivery and cancer therapy[110,46,111]. Among them, one-dimensional nanowires and nanotubes received special attention, whose lengths and diameters could be controlled to the scales of live cells and biomolecules, respectively[112]. These nanoentities were used as vehicles for

transporting biospecies, such as cytokines[64], peptides[113], enzymes[114], and genes[115], for in-vitro stimulation[64]. It remains a grand challenge to release biosubstances attached to nanoparticles in a tunable fashion, the achievement of which is expected to enable an in-depth understanding of the fundamental sciences in drug delivery, single cell stimulation, and cell-cell communications[64].

Previously, pulsed electrical potentials were employed to release biosubstances from patterned microelectrodes[116,117], demonstrating the feasibility of electrically induced biochemical release from nanoparticles. However, this intriguing mechanism requires complex lithographical patterning to electrically connect the nanoparticles. Recently, heat generated from optical excitation of plasmonic nanoparticles was used for releasing gene molecules[118]. Additionally, the vibrations induced by the radio-frequency electromagnetic fields have been used to enhance the rate of release of drug molecules[119]. Nevertheless, it remains a daunting task to tune the molecular release rate from individual nanoparticles with high precision and constant monitoring.

In this research, we investigated an innovative concept of motorized nanosensors for tuning the release rate of biochemicals and their real-time detection via systematic experimentation and analytical modeling. The nanomotor sensors, with enhanced functionalities in both molecular sensing and actuation, were assembled from designed plasmonic nanoparticles and patterned nanomagnets and rotated with controlled speed and chirality by the electric tweezers [61,63,65]. Both single and multiple analytes can be released in a tunable fashion by the mechanical rotation of nanomotors. The chemistry

and concentration of individual analytes were revealed simultaneously using high-speed micro-Raman spectroscopy. The mechanism of action was investigated and attributed to the convection-induced fluidic boundary layer reduction, which quantitatively agrees with the experimental results. To the best of our knowledge, this effect is observed in such a micro/nanomechanical system for the first time. This research, i.e., exploring robotized nanosensors by integrating SERS[120-122] and NEMS, could inspire a new device paradigm for biochemical detection, cell-cell communication, and drug delivery[64,123,124].

The designed nanomotor sensors consist of plasmonic-sensitive nanorods as rotors, patterned nanomagnets as bearings, and microelectrodes as stators, as shown in figure 6.4(a). The nanorod rotor, which is the most critical component of a nanomotor for attaching and detecting biochemicals, has a tri-layer structure with a core that is composed of a Au/Ni/Au three-segment nanowire, a layer of silica coated on the nanowire core, and uniformly surface-distributed Ag nanoparticles (NPs) synthesized on the outer surface of silica [figure 6.4(a)]. Here, each layer of the nanorod was designed to serve a purpose: the metallic nanowire core can be efficiently polarized in electric fields for the fast transport and rotation by our recent invention—the electric tweezers[61,63,65]; the Ni-segment presented in the nanowire core assists in anchoring the nanorod on a pre-patterned nanomagnet into a nanomotor[125]; and the mesoporous silica coating with densely surface-distributed Ag NPs (~1570/μm^2) provides efficient absorption of molecules for their subsequent ultrasensitive Raman detection[126].

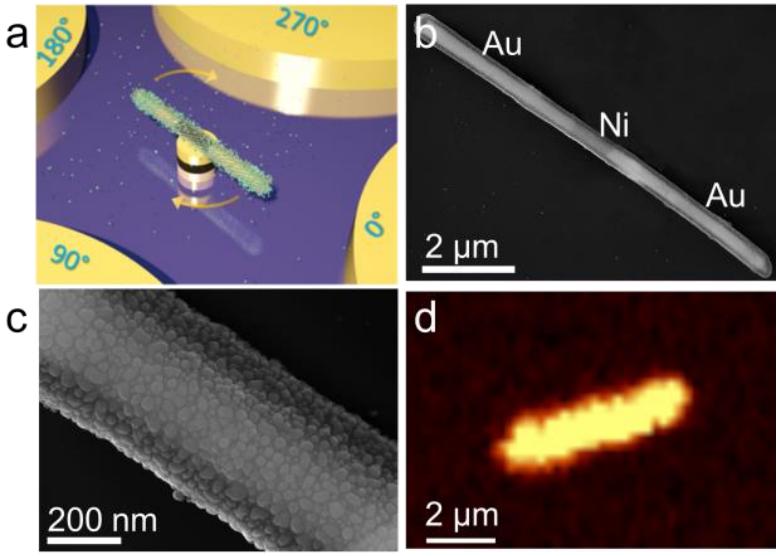

Figure 6.4: (a) Schematic diagram of a rotating nanomotor releasing molecules. (b) Scanning electron microscopy (SEM) images of plasmonic nanorods made of a three-layer structure with a Au-Ni-Au nanowire as the core, a silica coating, and a dense layer of Ag nanoparticles on the outer surface of silica. (c) A higher magnification SEM image shows the dense Ag nanoparticles grown on the silica. (d) Raman mapping of 1 μM R6G dispersed on a plasmonic nanorod showing essentially uniform SERS intensity on the surface of the nanorod.

Three steps were taken to fabricate the nanorotors. Briefly, the multi-segment Au/Ni/Au nanowires (300 nm in diameter) were synthesized by electrodeposition into nanoporous templates[63,127] before a 70 nm thick silica layer was coated on the outer surface of the nanowires via the hydrolysis of tetraethyl orthosilicate[67,68]. Next, a large

array of Ag NPs were synthesized uniformly on the surface of silica in a mixture of silver nitrite and ammonia via catalysis of polyvinylpyrrolidone (PVP) for 7 hours at 70°C[21]. Finally, the as-synthesized nanowire rotors were sonicated, centrifuged and washed before being re-dispersed in deionized (D.I.) water. Additional experimental details are provided in the Supporting Information.

SEM confirmed the successful synthesis of the tri-layered nanorod rotors, as shown in figures 6.4 (b–c). The Ag NPs, which can been seen to be densely distributed on the nanorod surface, were semi-spherical with an average diameter of ~25.2±6.4 nm and density of ~1570/μm^2. If we consider that the NP junctions are less than 2 nm as the plasmonic hotspots, where the Raman signals of molecules can be substantially enhanced because of ultrahigh electric fields generated by the coherence oscillation of conduction-band electrons[128], we find that the density of hotspots can be as high as ~1300/μm^2. These hotspots distributed along the nanorods are essentially uniform as shown in the Raman mapping of R6G molecules (figure 6.4(d)), 1 μM R6G incubated with the nanorods for 2 hrs before being dried). Here, the Raman image was obtained from a single plasmonic nanorod using a confocal Raman microscope exciting at 532 nm with a step size of 250 nm and a spot size of ~1 μm. The integration time of each spectrum was set at 0.5 s. The Raman enhancement factor of such nanorods can be estimated to be ~10^{10} following a method reported previously[49,51], which is one of the highest recorded among such state-of-the-art devices[72,129].

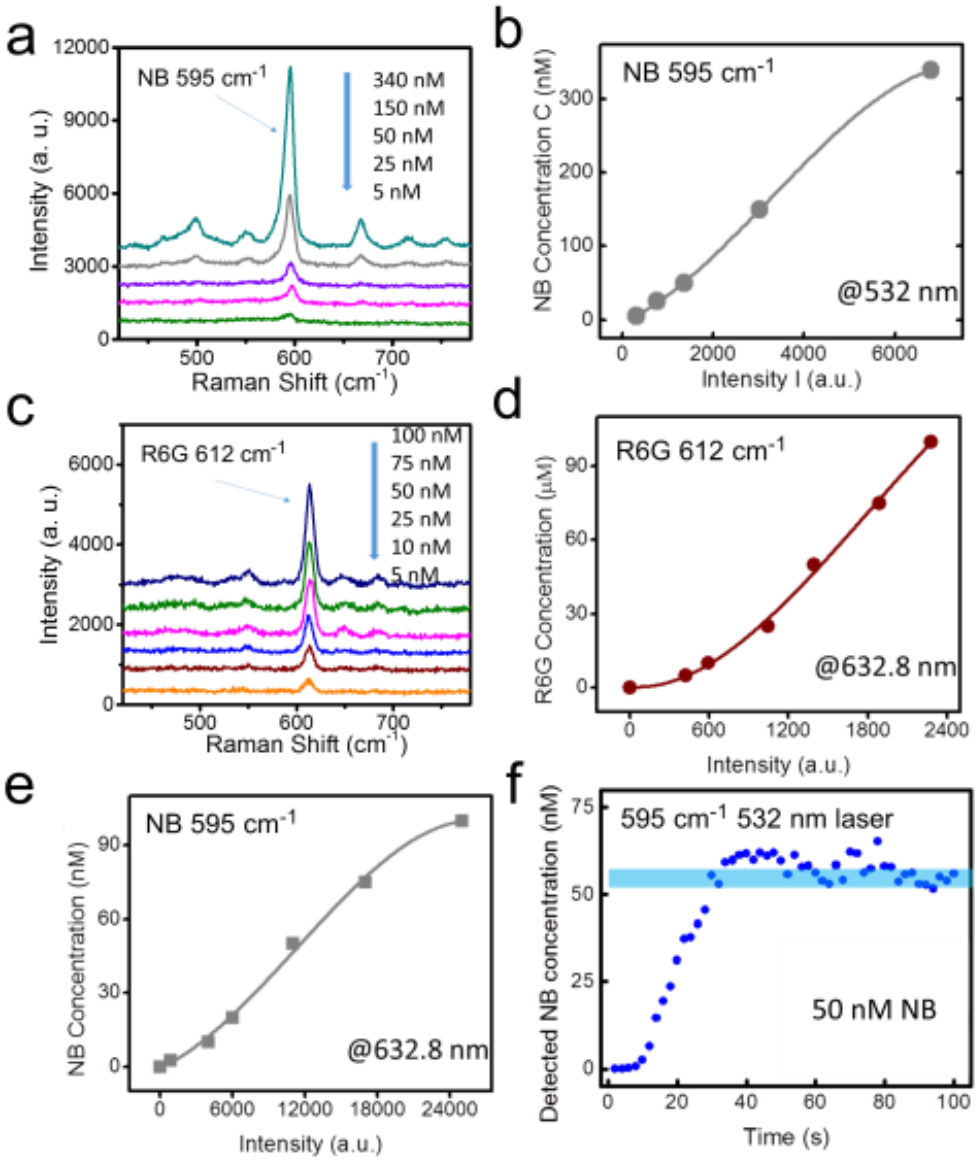

Figure 6.5: (a–e) Raman intensity (I_{SERS}) as a function of the concentration of NB (532 nm/632.8 nm laser excitation) and R6G (632 nm excitation). (f) Time-dependent detection of NB molecules (50 nM) adsorbing on a plasmonic nanorod.

The strong Raman enhancement and high density of hotspots on the nanorods are pivotal for ultrasensitive SERS detection. Using these nanorods, we can readily determine both the chemistry and concentration of multiple molecules simultaneously with Raman spectroscopy; nile blue (NB) and R6G, two commonly used SERS probes, were employed for this demonstration purpose due to their large Raman scattering cross-sections and wide biological applications[73].

The plasmonic nanorods were incubated in a series of NB solutions with concentrations from 5 nM to 340 nM for 30 min before detection with Raman spectroscopy. The Raman peak intensity at 595 cm^{-1} as function of NB concentration was plotted and fit with polynomial functions. The same method was employed to determine the relation between Raman intensity and concentration of NB or R6G in mixed solutions with a laser excitation at 632.8 nm. Five to eight plasmonic nanorods were examined for each concentration. Generally, the Raman intensity agrees among different plasmonic nanorods, with an average standard deviation of 24%, which could be largely due to the geometrical variation of the nanorods (i.e., diameter 10%, length 10%).

It was shown that the Raman intensity monotonically increased with the concentration of NB (or R6G) [figure 6.5(a–e)], from which, one can quantitatively determine the concentrations of the analytes. Note that we measured multiple nanorods to obtain the average Raman intensity for each concentration. The detection is highly sensitive such that the time-dependent absorption of biomolecules (e.g., NB, 50 nM) to the surface of the plasmonic nanorods can be monitored, which shows a monotonic

increase before reaching a saturation plateau at ~70 s [figure 6.5(f)]. For the absorption experiment, the plasmonic nanorods were fixed onto a glass slide by dispensing a small droplet of the nanorod suspension and drying it in air. Then, a PDMS film with a small well was attached to the glass slide and the sample was set in the Raman detection system. The laser beam was adjusted to a size of ~30 μm and focused on a nanorod on the substrate. The collection of the Raman spectra was initiated prior to the addition of a NB solution of 50 nM in the PDMS well. The Raman spectra were collected continuously, each with an integration time of 2 s.

More importantly, the structure of the plasmonic nanorods was carefully designed for a unique functionality—the activation of the plasmonic sensors into NEMS motors. The nanomotors consist of the plasmonic nanorods serving as rotors and the patterned nanomagnets as bearings (a thin-film stack of Au (100 nm)/Ni (80 nm)/Cr (6 nm), 1 μm in diameter) [figure 6.4(a)]. To assemble such nanomotors, we employed electric tweezers, which is a recently developed nanomanipulation technique that can align and transport non-spherical nanoentities with a precision of at least 300 nm[60,63]. The randomly suspended plasmonic nanorods were manipulated in both the X and Y directions. The transport velocity increased linearly with the applied DC voltages [figure 6.6(a)]. When the nanorods were in the vicinity of the nanomagnets, they were swiftly attracted to and assembled on the nanomagnets because of magnetic attraction. Then, a rotating electric field was generated by four AC electric voltages with sequential 90°

phase-shift applied to the quadruple microelectrodes, which compelled the plasmonic nanomotors to rotate [figure 6.4(a), figure 6.6(b)].

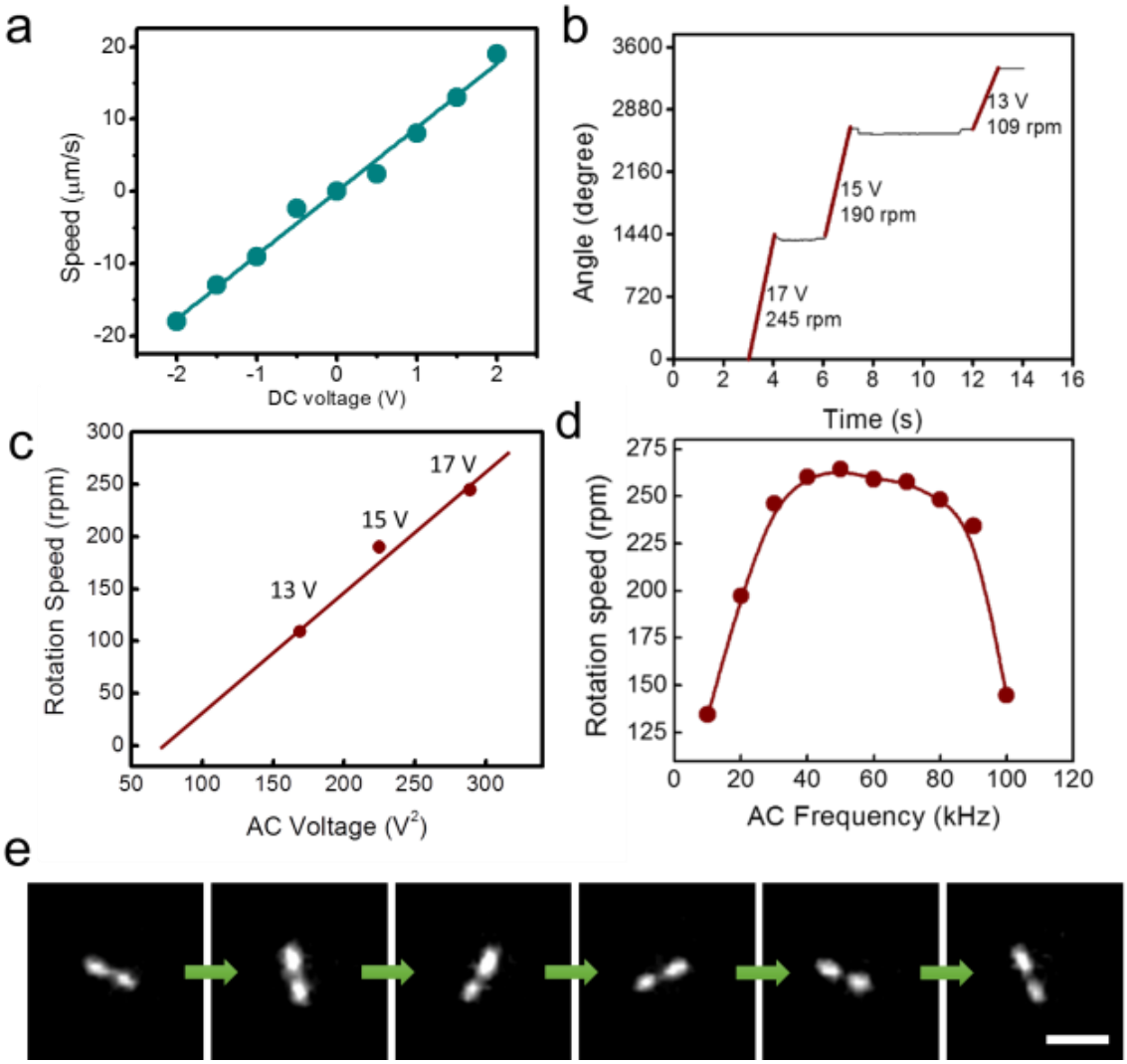

Figure 6.6: (a) The transport speed of the plasmonic nanorod increases with the applied DC voltages. (b, c) The rotational speed of nanomotors increases linearly with V^2 (20 kHz), (d) and it depends on the applied AC frequency (15 V). (e) Snapshots (every 1/6 second) of a rotating nanomotor functionalized with an NB imaged in the Raman mode. Note that the objective of the inverted microscope is underneath the rotating nanomotor. Thus, the Raman image of the middle portion of the plasmonic nanorotor is shadowed by the magnetic bearing. (Scale bar: 10 μm)

The rotation is a result of the induced electric torque (T_e) generated from the interactions between the polarized nanorod and the external AC electric field[65,130,131] as described in Section 5.2.2, where $T_e \sim E^2$. The E^2 dependence of the rotational speed (ω) accounts for its V^2 dependence in figure 6.6(c). In addition to the applied voltage, the speed of the plasmonic nanomotors can also be optimized by the applied AC frequency, where the highest value obtained at 50 kHz in the range of 10 to 100 kHz [figure 6.6(d)]. As a result, the functional nanoentities and nanomotors can be successfully synthesized, assembled, and actuated with high sensitivity for biochemical detection and control in mechanical rotation.

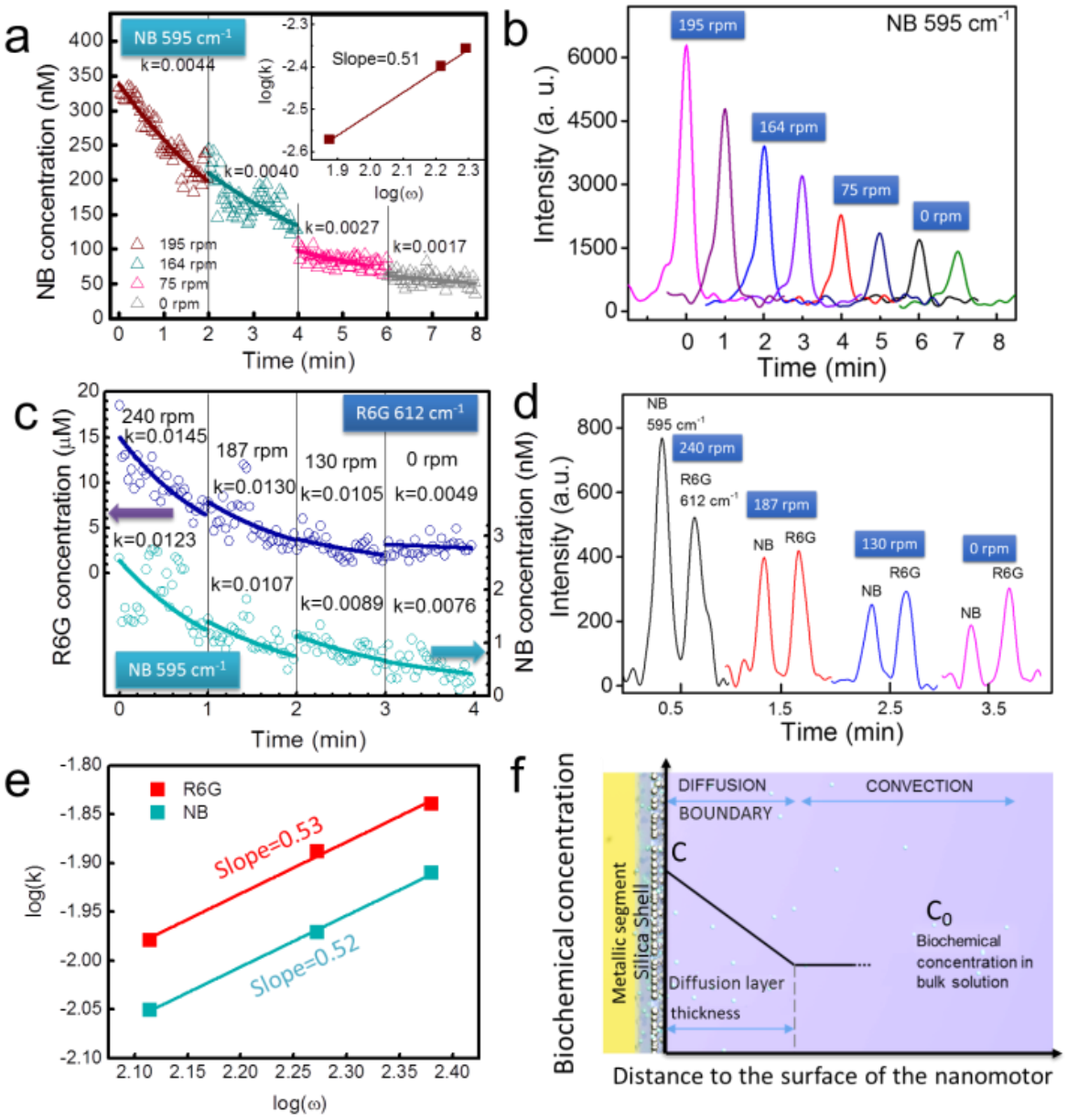
a
NB 595 cm-1
k=0.0044
k=0.0040
k=0.0027
k=0.0017
195 rpm
164 rpm
75 rpm
0 rpm
NB concentration (nM)
Time (min)
Slope=0.51
log(k)
log(ω)
b
NB 595 cm-1
195 rpm
164 rpm
75 rpm
0 rpm
Intensity (a. u.)
Time (min)
c
R6G 612 cm-1
240 rpm
k=0.0145
187 rpm
k=0.0130
130 rpm
k=0.0105
0 rpm
k=0.0049
k=0.0123
k=0.0107
k=0.0089
k=0.0076
NB 595 cm-1
R6G concentration (μM)
NB concentration (nM)
Time (min)
d
NB
595 cm-1
240 rpm
R6G
612 cm-1
187 rpm
NB
R6G
130 rpm
R6G
NB
0 rpm
R6G
NB
Intensity (a.u.)
Time (min)
e
R6G
NB
Slope=0.53
Slope=0.52
log(k)
log(ω)
f
DIFFUSION
BOUNDARY
CONVECTION
C
C0
Biochemical concentration in bulk solution
Metallic segment
Silica Shell
Diffusion layer thickness
Biochemical concentration
Distance to the surface of the nanomotor

Figure 6.7: Tunable release of biochemicals by the mechanical rotation of nanomotors. (a) Concentration of NB versus time at different rotational speeds. Inset: the rate of release monotonically increases with the rotational speed with a power-law dependence of 0.51. (b) Representative Raman spectra of R6G every 1 min at each rotational speed. (c) Tunable release of bi-analytes (i.e., NB and R6G) by the rotational speed. (d) Representative Raman spectra showing both analytes at different rotational speeds at every 1 min. (e) The release rates of both analytes of NB and R6G monotonically increase with the rotational speed with power-law dependencies of 0.52 and 0.53, respectively. (f) Schematic diagram of the model of the diffusion boundary layer next to the surface of the nanomotors. (Blue spheres: biochemical molecules; White spheres: Ag NPs)

Next, we investigated the applications of nanomotors for tuning the biochemical release and their associated mechanisms. Both the releases of single (NB) and multiplex biochemicals (i.e., mixtures of NB and R6G) were examined. The nanomotors were functionalized with NB (340 nM) or the mixture of NB (50 nM) and R6G (100 μM) by incubation in the respective solutions for 30 min (20 μl) before an aliquot of a 2 μl suspension solution was re-dispersed in an abundance of D. I. water (2 ml). Immediately after the dispersion, the nanorods were quickly assembled into nanomotors and rotated. The distribution of molecules according to their Raman signals on the surface of the nanomotors can be directly imaged and videotaped by the ultrasensitive high-speed CCD

camera at a frame rate of 24 f/s [figure 6.6(e)]. In the study of the molecular release of NB, the rotational speed of the nanomotors was precisely controlled from 195 rpm to 75 rpm at 17 to 10 V. The molecular release rate from the surface of the rotating nanorods was monitored and recorded simultaneously using a high-speed Raman spectroscope operating at 0.5 spectrum/s [figures 6.7(a–b)].

It was found that, regardless of the rotational speed or the molecular species, the concentration of the molecules measured with the Raman spectra decreased monotonically with time. Note that only those molecules attached to the nanomotors can be detected, due to the significant plasmonic enhancement from the Ag NPs. Additionally, the molecular concentration on the surface of nanomotors was much higher than that in the bulk solution. Consequently, a net molecular mass flow can be established from the nanomotors to the bulk solution, which is consistent with the monotonic concentration decrease observed in Raman spectroscopy.

This phenomenon can be modeled using the Nernst diffusion-layer theory, which is widely used to rationalize phenomena involving solid-liquid interfaces[132]. According to this theory, a stationary liquid layer is formed with a thickness of λ at the interface of a solid surface and a suspension medium. Within such a stationary layer, the transport of mass, such as molecules or ions, between the solid surface and bulk liquid can occur only by passive diffusion in the direction of the chemical gradient. Out of such a region, liquid convection dominates, which can actively pump molecules to the outer boundary of the stationary layer. If the concentration of the analyte at the layer boundary is approximated

to be same as that in the bulk solution, then a static concentration gradient can be established across this stationary diffusion layer, as shown in figure 6.7(f). According to Fick's diffusion laws, the time dependence concentration of molecules on the surface of nanomotors (C) can be calculated as:

$$C = C' \cdot e^{-kt} + C_0 \qquad (1)$$

where $C' = C_1 - C_0$, C_1 is the initial concentrations of NB on the surface of nanomotors, C_0 is the concentration of NB in the bulk solution, and k (with a unit of 1/s) is the molecule release rate. The value of k is proportional to D/λ, where D is the diffusion coefficient of the NB molecules. From Eq. (1), we can readily determine the rate of molecule release when the nanomotors were rotated at different speeds (ω). Here, at each rotational speed, the data were fit according to Eq. (1) using the Origin software package with the initial C_1 values given as the as-measured values [figure f.7(a)]. Notably, the molecule release rate (k) monotonically increases with the rotational speed with a power-law dependence of $k \sim \omega^{0.51}$ [figure 6.7(a) inset). How can the mechanical rotation of nanomotors tune the rate of molecule release? We attribute the mechanism to the reduction of the stationary diffusion layer as a result of liquid convection due to the rotation of nanomotors. This phenomenon is described by the classical boundary layer theory[33]. According to this theory, a flow with a speed of v passing over a flat surface can result in the thinning of the stationary layer next to the solid surface due to fluidic convection promoted by the flow. The thickness of the stationary layer follows the relation of $\lambda \sim {R_e}^{-0.5} \sim v^{-0.5}$.[133] Given the molecular release rate of $k \sim D/\lambda \sim 1/\lambda$ and

that the fluidic velocity (v) is proportional to the rotational speed (ω) of the nanomotors ($v \sim \omega$), it can be readily shown that $k \sim \sqrt{\omega}$, which quantitatively agrees with our experimental observation of $k \sim \omega^{0.51}$ (figure 6.7(a) inset). Moreover, we note that the theory for the rotating disk electrode (RDE) system, which has been studied extensively in electrochemistry[132], further supports our understanding, which is that the transport of ionic masses to a rotating disk electrode increases with the rotational speed of the electrode with a power-law dependence of 0.5 [132,134,135].

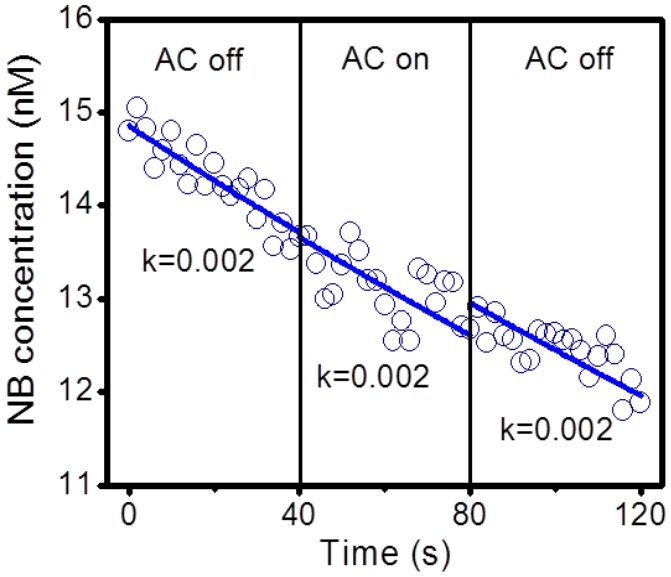

Figure 6.8: The release rate (k) remains a constant (of 0.002 /s) when the AC ***E***-field was alternatively switched "on" and "off".

It is also important to determine whether the applied AC electric (E) fields could directly alter the molecule release rate[131]. A control experiment was performed on a stationary nanorotor functionalized with NB molecules. The AC E-fields (17 V, 20 kHz)

were turned on and off alternately multiple times while the molecular release was monitored. The molecular release rate remained unchanged when the *E*-field was modulated, which suggests that the AC *E*-field has a negligible effect on the molecule release rate (figure 6.8). This experiment was repeated several times to confirm this observation.

The next question is whether the above mechanism is applicable to the release of multiplex biochemicals? To address this question, we functionalized the nanomotors with a mixture of NB and R6G, rotated the nanomotors from 240 to 130 rpm at 18 to 14 V, 50 kHz, and collected the time-dependent Raman signals of both analytes. As each type of molecule possesses a unique Raman spectrum, the chemistry, as well as the concentration of each analyte on the surface of nanomotors, can be determined simultaneously (figures 6.7(c–d)). By employing the same fitting procedure used for the single chemical release, we determined the release rate (k) of each biochemical at different rotational speed (ω). Both analytes showed demonstrated linear increment with ω with a power-law dependence of 0.52 and 0.53 for NB and R6G, respectively (figure 6.7(a)). The results demonstrated that the release of multiplex biochemicals has the dependence of $k \sim \omega^{0.5}$, which is the same found for single analyte release and suggests that the aforementioned model used to rationalize single molecule release can be applied to multiplex release. Moreover, we note that the release rate of NB (k: 0.0076 ~ 0.0123 s^{-1}) in the multiplex release system is consistently higher than that obtained as a single analyte (k: 0.0017~0.0044 s^{-1}). This outcome can be attributed to the higher concentration and

release rate of R6G molecules in the multiplex sample, where the dominating R6G could assist the detachment of NB molecules from the nanomotors during its own release and thus increase the release rate of NB. Here, a much higher concentration of R6G is necessary in the mixed sample (R6G:~20 μM, NB:~ a few nM) to obtain signals from both molecules on a similar level, which could be due to the much poorer attachment of R6G to Ag NPs than NB.

In summary, we investigated a new mechanism for tuning the release rate of biochemicals from the surface of nanoparticles via controlled mechanical rotation. The investigation was conducted with both experimentation and analytic modeling. We synthesized, assembled and rotated surface-enhanced plasmonic nanomotor sensors in this study. The kinetics of molecule release from the nanomotors was monitored by high-speed Raman spectroscopy. Both single and multiple analytes can be released at desirable rates by controlling the rotational speeds of the nanomotors. The release rate shows a power-law dependence of approximately 0.5 with the rotational speed. The release mechanism can be attributed to the convection-induced thickness reduction of the diffusion layer, which agrees quantitatively with the experimental results. To the best of our knowledge, this effect has been observed with micro/nanoscale devices for the first time in the present work. The nanomotor sensors could be useful for tuning the release rate of biosignals relevant to single-cell stimulation, cell-cell communication, and drug delivery. This research could also inspire a new device scheme of robotized nanosensors.

Chapter 7: Conclusion

In conclusion, we rationally designed and synthesized ultrasensitive SERS sensitive nanoparticles as motorized nanosensors. Two enhancement mechanisms were investigated by both numerical simulation and experimental testing. The nanomotor sensors were innovatively applied for location predicable biochemical detection, single-cell bioanalysis, and controllable biochemical release and real-time detection. This work, exploring robotized nanosensors by integrating SERS and NEMS, could inspire a new device scheme for biochemical detection, cell-cell communication, and drug delivery.

Appendix A: List of journal Publications

1. K. Kim*, **X. Xu***, J. Guo* and D. L. Fan. “Ultrahigh-Speed Rotating Nanoelectromechanical System (NEMS) Devices Assembled from Nanoscale Building Blocks”. ***Nature Communications***, 5, 3632 (2014)
2. **X. Xu**, K. Kim, H. Li, D. L. Fan, " Ordered Arrays of Raman Nanosensors for Ultrasensitive and Location Predictable Biochemical Detection", ***Advanced Materials***, 24, 5516 (2012)
3. **X. Xu***, C. Liu*, K. Kim and D .L. Fan. “Electric-Driven Rotation of Silicon Nanowires and Silicon Nanowires”, ***Advanced Functional Materials***, 24, 4843 (2014)
4. **X. Xu**, H. Li, D. Hasan, R. Ruoff, A. X. Wang and D. L. Fan, "Near-Field Enhanced Magnetic Plasmonic Bifunctional Nanotubes for Single Cell Bioanalysis", ***Advanced Functional Materials***, 23. 4332 (2013)
5. D. L. Fan, F. Q. Zhu, **X. Xu**, R. C. Cammarata and C. L. Chien, "Electronic Properties of Nanoentities Revealed by Mechanical Motion" ***Proceeding of the National Academy of Science*** USA, 109, 9309 (2012)
6. **X. Xu***, D. Hasan*, L. Wang*, S. Chakravarty, R. T. Chen, D. L. Fan and A. X. Wang, " Guided-Mode-Resonance-Coupled Plasmonic-Active SiO2 Nanotubes for Surface Enhanced Raman Spectroscopy", ***Applied Physics Letters***, 100, 191114 (2012)

7. J. Ning*, **X. Xu***, C. Liu and D. L. Fan, " Three-Dimensional Freestanding Porous Thin Graphite Nanosuperstructures for $Ni(OH)_2$-based Energy Storage Devices", ***Journal of Materials Chemistry A***, in press (2014)
8. C. Liu, **X. Xu**, Alex Rettie, C. Mullins and D. L. Fan, " Rational One-Step Synthesis of 3-D ZnO Nanosuperstructures by Engineered Catalysts for Substantial Improvement of Solar Water Oxidation Efficiency", ***Journal of Materials Chemistry A***, 1, 8111 (2013)
9. **X. Xu**, M. Wu, M. Asoro, P. Ferreira and D. L. Fan, "One Step Hydrothermal Synthesis of Comb-like ZnO Nanostructures ", ***Crystal Growth and Design***, 12, 4829 (2012)
10. X. Wang, R. T. Chen, and D. L. Fan, C. Lin, **X. Xu**, L. Wang, "Ultra-Efficient Nano-Photonic Devices using Hybrid Material Systems for Optical Communication and Sensing ", ***Avionics, IEEE, AVFOP 2012*** (2012)
11. **X. Xu**, K. Kim, D. L. Fan. "Rotary enhanced ultra-sensitive bio-sensor", ***ASME-Journal of Nanotechnology in Engineering and Medicine***, submitted (2014)
12. **X. Xu**, K. Kim, D. L. Fan. "Tunable Release of Multiplex Biochemicals by Plasmonic Nanomotors", ***Angewandte Chemie International Edition,*** in press (2014)
13. J. Ning*, **X. Xu***, C. Liu and D. L. Fan, "Three-Dimensional Porous Graphite/Mn_3O_4 Nanosuperstructures for Electrochemical Supercapacitors", ***Chemistry of Materials***, in preparation (2014)

Appendix B: List of conference presentations

1. **X. Xu**, K. Kim and D. L. Fan, "Plasmonic Rotary Nanomotors for Controlled Biochemical Release and Detection with Raman Spectroscopy", ***2014 MRS Spring Meeting & Exhibit***, San Francisco, CA (2014)

2. J. Ning*****, **X. Xu***, C. Liu and D. L. Fan "Free Standing T hree-Dimensional Porous Graphite/$Ni(OH)_2$ Foam for Supercapacitors" ***2014 MRS Spring Meeting & Exhibit, San Francisco***, CA (2014)

3. D. L. Fan and **X. Xu**, "Ultrasensitive Surface Enhanced Raman Scattering (SERS) Nanomotor Sensors", ***Energy Materials Nanotechnology Spring Meeting***, Orlando, FL (2013)

4. J. Ning, **X. Xu**, C. Liu and D. L. Fan, "Three Dimensional Graphene/Graphite Structures Templated on Engineered Highly Porous Ni/Cu Foams" ***NanoTechnology for Defense Conference***, Tucson, AZ (2013)

5. **X. Xu**, K. Kim and D. L. Fan, "Plasmonic Rotary Nanomotors for Controlled Biochemical Release and Detection with Raman Spectroscopy" ***NanoTechnology for Defense Conference,*** Tucson, AZ (2013)

6. C. Liu, **X. Xu**, A. Rettie, C. Mullin and D. L. Fan. "One-step Waferscale Synthesis of 3-D Highly Branched Semiconductor Nanoarchitectures by Designed Chemical Catalysts for Substantial Improvement of Solar Water Oxidation Efficiency" ***NanoTechnology for Defense Conference***, Tucson, AZ (2013)

7. **X. Xu**, H. Li, R. S. Ruoff, A. X. Wang, D. L. Fan, "Bifunctional Nanotubes for Single Cell Sensing" ***2012 MRS Fall Meeting & Exhibit***, Boston, MA (2012)

8. C. Liu, **X. Xu**, A. Rettie, C. Mullin and D. L. Fan. "Rational One-step Synthesis of Three-Dimensional ZnO Nanosuperstructures by Engineered Catalysts for 150% Improvement of Solar Water Splitting", ***2012 MRS Fall Meeting & Exhibit***, Boston, MA (2012)

9. **X. Xu**, M. Wu, M. Asoro, C. Liu, H. P. He, P. Ferreira and D. L. Fan, "Facile Synthesis of ZnO Superstructures Assisted by One-Dimensional Catalysts", ***2011 MRS Fall Meeting & Exhibit***, Boston, MA (2011)

10. **X. Xu**, K. Kim and D. L. Fan, "Determining Metallicity of Nanowires via Their Mechanical Motions in Electric Fields", ***2011 MRS Fall Meeting & Exhibit***, Boston, MA (2011)

11. **X. Xu**, H. F. Li, K. Kim, R. S. Ruoff, A. Wang, D. L. Fan, "Ordered Arrays of Plasmonic Magnetic Nanotubes For Single Molecular Biosensing", ***2011 MRS Fall Meeting & Exhibit***, Boston, MA (2011)

Reference

(1) Fleischmann, M.; Hendra, P. J.; McQuillan, A. J. Raman spectra of pyridine adsorbed at a silver electrode. *Chem. Phys. Lett.* **1974**, *26*, 163.

(2) Jeanmaire, D. L.; Van Duyne, R. P. Surface raman spectroelectrochemistryPart I. Heterocyclic, aromatic, and aliphatic amines adsorbed on the anodized silver electrode. *Journal of Electroanalytical Chemistry and Interfacial Electrochemistry* **1977**, *84*, 1.

(3) Albrecht, M. G.; Creighton, J. A. Anomalously intense Raman spectra of pyridine at a silver electrode. *J. Am. Chem. Soc.* **1977**, *99*, 5215.

(4) Nie, S. M.; Emery, S. R. Probing single molecules and single nanoparticles by surface-enhanced Raman scattering. *Science* **1997**, *275*, 1102.

(5) Kneipp, K.; Wang, Y.; Kneipp, H.; Perelman, L. T.; Itzkan, I.; Dasari, R.; Feld, M. S. Single molecule detection using surface-enhanced Raman scattering (SERS). *Phys. Rev. Lett.* **1997**, *78*, 1667.

(6) Rao, S.; Raj, S.; Balint, S.; Fons, C. B.; Campoy, S.; Llagostera, M.; Petrov, D. Single DNA molecule detection in an optical trap using surface-enhanced Raman scattering. *Appl. Phys. Lett.* **2010**, *96*.

(7) Kang, T.; Yoo, S. M.; Yoon, I.; Lee, S. Y.; Kim, B. Patterned Multiplex Pathogen DNA Detection by Au Particle-on-Wire SERS Sensor. *Nano Lett.* **2010**, *10*, 1189.

(8) Barhoumi, A.; Halas, N. J. Label-free detection of DNA hybridization using surface enhanced Raman spectroscopy. *J Am Chem Soc* **2010**, *132*, 12792.

(9) Barhoumi, A.; Zhang, D.; Tam, F.; Halas, N. J. Surface-enhanced Raman spectroscopy of DNA. *J Am Chem Soc* **2008**, *130*, 5523.

(10) Zhang, X.; Zhao, J.; Whitney, A. V.; Elam, J. W.; Van Duyne, R. P. Ultrastable substrates for surface-enhanced Raman spectroscopy: Al2O3 overlayers fabricated by atomic layer deposition yield improved anthrax biomarker detection. *J Am Chem Soc* **2006**, *128*, 10304.

(11) Zhang, X.; Young, M. A.; Lyandres, O.; Van Duyne, R. P. Rapid detection of an anthrax biomarker by surface-enhanced Raman spectroscopy. *J Am Chem Soc* **2005**, *127*, 4484.

(12) Stuart, D. A.; Biggs, K. B.; Van Duyne, R. P. Surface-enhanced Raman spectroscopy of half-mustard agent. *Analyst* **2006**, *131*, 568.

(13) Ma, K.; Yuen, J. M.; Shah, N. C.; Walsh, J. T., Jr.; Glucksberg, M. R.; Van Duyne, R. P. In vivo, transcutaneous glucose sensing using surface-enhanced spatially offset Raman spectroscopy: multiple rats, improved hypoglycemic accuracy, low incident power, and continuous monitoring for greater than 17 days. *Anal Chem* **2011**, *83*, 9146.

(14) Stuart, D. A.; Yuen, J. M.; Shah, N.; Lyandres, O.; Yonzon, C. R.; Glucksberg, M. R.; Walsh, J. T.; Van Duyne, R. P. In vivo glucose measurement by surface-enhanced Raman spectroscopy. *Anal Chem* **2006**, *78*, 7211.

(15) Shafer-Peltier, K. E.; Haynes, C. L.; Glucksberg, M. R.; Van Duyne, R. P. Toward a glucose biosensor based on surface-enhanced Raman scattering. *J. Am. Chem. Soc.* **2003**, *125*, 588.

(16) Stuart, D. A.; Yonzon, C. R.; Zhang, X.; Lyandres, O.; Shah, N. C.; Glucksberg, M. R.; Walsh, J. T.; Van Duyne, R. P. Glucose sensing using near-infrared surface-enhanced Raman spectroscopy: gold surfaces, 10-day stability, and improved accuracy. *Anal Chem* **2005**, *77*, 4013.

(17) Lyandres, O.; Shah, N. C.; Yonzon, C. R.; Walsh, J. T., Jr.; Glucksberg, M. R.; Van Duyne, R. P. Real-time glucose sensing by surface-enhanced Raman spectroscopy in bovine plasma facilitated by a mixed decanethiol/mercaptohexanol partition layer. *Anal Chem* **2005**, *77*, 6134.

(18) Yonzon, C. R.; Haynes, C. L.; Zhang, X.; Walsh, J. T., Jr.; Van Duyne, R. P. A glucose biosensor based on surface-enhanced Raman scattering: improved partition layer, temporal stability, reversibility, and resistance to serum protein interference. *Anal Chem* **2004**, *76*, 78.

(19) Yuen, J. M.; Shah, N. C.; Walsh, J. T., Jr.; Glucksberg, M. R.; Van Duyne, R. P. Transcutaneous glucose sensing by surface-enhanced spatially offset Raman spectroscopy in a rat model. *Anal Chem* **2010**, *82*, 8382.

(20) Kim, H.; Kosuda, K. M.; Van Duyne, R. P.; Stair, P. C. Resonance Raman and surface- and tip-enhanced Raman spectroscopy methods to study solid catalysts and heterogeneous catalytic reactions. *Chem Soc Rev* **2010**, *39*, 4820.

(21) Heck, K. N.; Janesko, B. G.; Scuseria, G. E.; Halas, N. J.; Wong, M. S. Observing metal-catalyzed chemical reactions in situ using surface-enhanced Raman spectroscopy on Pd-Au nanoshells. *J Am Chem Soc* **2008**, *130*, 16592.

(22) Le Ru, E. C.; Etchegoin, P. G. *Principles of Surface-Enhanced Raman Spectroscopy: And Related Plasmonic Effects*; Elsevier Science, 2008.

(23) Stiles, P. L.; Dieringer, J. A.; Shah, N. C.; Van Duyne, R. P. Surface-Enhanced Raman Spectroscopy. *Annual Review of Analytical Chemistry* **2008**, *1*, 601.

(24) Barhoumi, A.; Zhang, D.; Tam, F.; Halas, N. J. Surface-Enhanced Raman Spectroscopy of DNA. *J Am Chem Soc* **2008**, *130*, 5523.

(25) Talley, C. E.; Jackson, J. B.; Oubre, C.; Grady, N. K.; Hollars, C. W.; Lane, S. M.; Huser, T. R.; Nordlander, P.; Halas, N. J. Surface-Enhanced Raman Scattering from Individual Au Nanoparticles and Nanoparticle Dimer Substrates. *Nano Lett* **2005**, *5*, 1569.

(26) Zhu, Y. F.; Shi, J. L.; Shen, W. H.; Dong, X. P.; Feng, J. W.; Ruan, M. L.; Li, Y. S. Stimuli-responsive controlled drug release from a hollow mesoporous silica sphere/polyelectrolyte multilayer core-shell structure. *Angew Chem Int Edit* **2005**, *44*, 5083.

(27) Qin, L. D.; Jang, J. W.; Huang, L.; Mirkin, C. A. Sub-5-nm gaps prepared by on-wire lithography: Correlating gap size with electrical transport. *Small* **2007**, *3*, 86.

(28) Huebner, U.; Schneidewind, H.; Cialla, D.; Weber, K.; Zeisberger, M.; Mattheis, R.; Moeller, R.; Popp, J. Fabrication of regular patterned SERS arrays by electron beam lithography. *Biophotonics: Photonic Solutions for Better Health Care Ii* **2010**, *7715*.

(29) Haynes, C. L.; Van Duyne, R. P. Nanosphere lithography: A versatile nanofabrication tool for studies of size-dependent nanoparticle optics. *J. Phys. Chem. B* **2001**, *105*, 5599.

(30) Feng, F.; Zhi, G.; Jia, H. S.; Cheng, L.; Tian, Y. T.; Li, X. J. SERS detection of low-concentration adenine by a patterned silver structure immersion plated on a silicon nanoporous pillar array. *Nanotechnology* **2009**, *20*.

(31) Jiao, Y.; Ryckman, J. D.; Ciesielski, P. N.; Escobar, C. A.; Jennings, G. K.; Weiss, S. M. Patterned nanoporous gold as an effective SERS template. *Nanotechnology* **2011**, *22*.

(32) Banholzer, M. J.; Qin, L. D.; Millstone, J. E.; Osberg, K. D.; Mirkin, C. A. On-wire lithography: synthesis, encoding and biological applications. *Nature Protocols* **2009**, *4*, 838.

(33) Qin, L. D.; Park, S.; Huang, L.; Mirkin, C. A. On-wire lithography. *Science* **2005**, *309*, 113.

(34) Ko, H.; Singamaneni, S.; Tsukruk, V. V. Nanostructured Surfaces and Assemblies as SERS Media. *Small* **2008**, *4*, 1576.

(35) Zheng, G. F.; Chen, X. D.; Mirkin, C. A. Complementary Electrical and Spectroscopic Detection Assays with On-Wire-Lithography-Based Nanostructures. *Small* **2009**, *5*, 2537.

(36) Lee, S. J.; Morrill, A. R.; Moskovits, M. Hot spots in silver nanowire bundles for surface-enhanced Raman spectroscopy. *J. Am. Chem. Soc.* **2006**, *128*, 2200.

(37) Kneipp, K.; Wang, Y.; Kneipp, H.; Itzkan, I. I.; Dasari, R. R.; Feld, M. S. Population pumping of excited vibrational states by spontaneous surface-enhanced Raman scattering. *Phys Rev Lett* **1996**, *76*, 2444.

(38) Michaels, A. M.; Jiang, J.; Brus, L. Ag nanocrystal junctions as the site for surface-enhanced Raman scattering of single Rhodamine 6G molecules. *J. Phys. Chem. B* **2000**, *104*, 11965.

(39) Wang, H.; Schaefer, K.; Moeller, M. In situ Immobilization of Gold Nanoparticle Dimers in Silica Nanoshell by Microemulsion Coalescence. *J. Phys. Chem. C* **2008**, *112*, 3175.

(40) Wang, X.; Li, G.; Chen, T.; Yang, M.; Zhang, Z.; Wu, T.; Chen, H. Polymer-Encapsulated Gold-Nanoparticle Dimers: Facile Preparation and Catalytical Application in Guided Growth of Dimeric ZnO-Nanowires. *Nano Lett.* **2008**, *8*, 2643.

(41) Wustholz, K. L.; Henry, A.-I.; McMahon, J. M.; Freeman, R. G.; Valley, N.; Piotti, M. E.; Natan, M. J.; Schatz, G. C.; Duyne, R. P. V. Structure−Activity Relationships in Gold Nanoparticle Dimers and Trimers for Surface-Enhanced Raman Spectroscopy. *J. Am. Chem. Soc.* **2010**, *132*, 10903.

(42) Oldenburg, S. J.; Averitt, R. D.; Westcott, S. L.; Halas, N. J. Nanoengineering of optical resonances. *Chem. Phys. Lett.* **1998**, *288*, 243.

(43) Jackson, J. B.; Halas, N. J. Silver Nanoshells: Variations in Morphologies and Optical Properties. *The Journal of Physical Chemistry B* **2001**, *105*, 2743.

(44) Prodan, E.; Nordlander, P. Structural Tunability of the Plasmon Resonances in Metallic Nanoshells. *Nano Lett.* **2003**, *3*, 543.

(45) Kundu, J.; Levin, C. S.; Halas, N. J. Real-time monitoring of lipid transfer between vesicles and hybrid bilayers on Au nanoshells using surface enhanced Raman scattering (SERS). *Nanoscale* **2009**, *1*, 114.

(46) Choi, M.-R.; Stanton-Maxey, K. J.; Stanley, J. K.; Levin, C. S.; Bardhan, R.; Akin, D.; Badve, S.; Sturgis, J.; Robinson, J. P.; Bashir, R.; Halas, N. J.; Clare, S. E. A Cellular Trojan Horse for Delivery of Therapeutic Nanoparticles into Tumors. *Nano Lett.* **2007**, *7*, 3759.

(47) Ayala-Orozco, C.; Liu, J. G.; Knight, M. W.; Wang, Y. M.; Day, J. K.; Nordlander, P.; Halas, N. J. Fluorescence Enhancement of Molecules Inside a Gold Nanomatryoshka. *Nano Lett* **2014**, *14*, 2926.

(48) Chou, S. Y.; Krauss, P. R.; Renstrom, P. J. Imprint lithography with 25-nanometer resolution. *Science* **1996**, *272*, 85.

(49) Hu, M.; Ou, F. S.; Wu, W.; Naumov, I.; Li, X.; Bratkovsky, A. M.; Williams, R. S.; Li, Z. Gold Nanofingers for Molecule Trapping and Detection. *J. Am. Chem. Soc.* **2010**, *132*, 12820.

(50) Ou, F. S.; Hu, M.; Naumov, I.; Kim, A.; Wu, W.; Bratkovsky, A. M.; Li, X.; Williams, R. S.; Li, Z. Hot-Spot Engineering in Polygonal Nanofinger Assemblies for Surface Enhanced Raman Spectroscopy. *Nano Lett.* **2011**, *11*, 2538.

(51) Schmidt, M. S.; Hübner, J.; Boisen, A. Large Area Fabrication of Leaning Silicon Nanopillars for Surface Enhanced Raman Spectroscopy. *Adv. Mater.* **2012**, *24*, OP11.

(52) Liusman, C.; Li, S. Z.; Chen, X. D.; Wei, W.; Zhang, H.; Schatz, G. C.; Boey, F.; Mirkin, C. A. Free-Standing Bimetallic Nanorings and Nanoring Arrays Made by On-Wire Lithography. *Acs Nano* **2010**, *4*, 7676.

(53) Jones, M. R.; Osberg, K. D.; Macfarlane, R. J.; Langille, M. R.; Mirkin, C. A. Templated techniques for the synthesis and assembly of plasmonic nanostructures. *Chem Rev* **2011**, *111*, 3736.

(54) Qin, L. D.; Zou, S. L.; Xue, C.; Atkinson, A.; Schatz, G. C.; Mirkin, C. A. Designing, fabricating, and imaging Raman hot spots. *P Natl Acad Sci USA* **2006**, *103*, 13300.

(55) Qin, L.; Zou, S.; Xue, C.; Atkinson, A.; Schatz, G. C.; Mirkin, C. A. Designing, fabricating, and imaging Raman hot spots. *Proceedings of the National Academy of Sciences of the United States of America* **2006**, *103*, 13300.

(56) Qin, L.; Banholzer, M. J.; Millstone, J. E.; Mirkin, C. A. Nanodisk Codes. *Nano Lett.* **2007**, *7*, 3849.

(57) Banholzer, M. J.; Osberg, K. D.; Li, S.; Mangelson, B. F.; Schatz, G. C.; Mirkin, C. A. Silver-Based Nanodisk Codes. *ACS Nano* **2010**, *4*, 5446.

(58) Anker, J. N.; Hall, W. P.; Lyandres, O.; Shah, N. C.; Zhao, J.; Van Duyne, R. P. Biosensing with plasmonic nanosensors. *Nature Materials* **2008**, *7*, 442.

(59) Moskovits, M. IMAGING Spot the hotspot. *Nature* **2011**, *469*, 307.

(60) Fan, D. L.; Cammarata, R. C.; Chien, C. L. Precision transport and assembling of nanowires in suspension by electric fields. *Appl. Phys. Lett.* **2008**, *92*, 093115.

(61) Fan, D. L.; Zhu, F. Q.; Cammarata, R. C.; Chien, C. L. Manipulation of nanowires in suspension by ac electric fields. *Appl. Phys. Lett.* **2004**, *85*, 4175.

(62) Fan, D. L.; Zhu, F. Q.; Cammarata, R. C.; Chien, C. L. Efficiency of assembling of nanowires in suspension by ac electric fields. *Appl. Phys. Lett.* **2006**, *89*, 223115.

(63) Fan, D. L.; Zhu, F. Q.; Cammarata, R. C.; Chien, C. L. Electric tweezers. *Nano Today* **2011**, *6*, 339.

(64) Fan, D.; Yin, Z.; Cheong, R.; Zhu, F. Q.; Cammarata, R. C.; Chien, C. L.; Levchenko, A. Subcellular-resolution delivery of a cytokine through precisely manipulated nanowires. *Nature Nanotech.* **2010**, *5*, 545.

(65) Fan, D.; Zhu, F.; Cammarata, R.; Chien, C. Controllable High-Speed Rotation of Nanowires. *Phys. Rev. Lett.* **2005**, *94*.

(66) Inaba, S.; Fujino, S.; Sakai, K. Non-contact measurement of the viscosity of a soda-lime-silica melt using electric field tweezers. *Physics and Chemistry of Glasses-European Journal of Glass Science and Technology Part B* **2010**, *51*, 304.

(67) Yi, D. K.; Selvan, S. T.; Lee, S. S.; Papaefthymiou, G. C.; Kundaliya, D.; Ying, J. Y. Silica-coated nanocomposites of magnetic nanoparticles and quantum dots. *J. Am. Chem. Soc.* **2005**, *127*, 4990.

(68) Graf, C.; Vossen, D. L. J.; Imhof, A.; van Blaaderen, A. A general method to coat colloidal particles with silica. *Langmuir* **2003**, *19*, 6693.

(69) Amendola, V.; Bakr, O. M.; Stellacci, F. A Study of the Surface Plasmon Resonance of Silver Nanoparticles by the Discrete Dipole Approximation Method: Effect of Shape, Size, Structure, and Assembly. *Plasmonics* **2010**, *5*, 85.

(70) Liu, Z. X.; Wang, H. H.; Li, H.; Wang, X. M. Red shift of plasmon resonance frequency due to the interacting Ag nanoparticles embedded in single crystal SiO2 by implantation. *Appl. Phys. Lett.* **1998**, *72*, 1823.

(71) Smythe, E. J.; Dickey, M. D.; Bao, J. M.; Whitesides, G. M.; Capasso, F. Optical Antenna Arrays on a Fiber Facet for in Situ Surface-Enhanced Raman Scattering Detection. *Nano Lett.* **2009**, *9*, 1132.

(72) Blackie, E. J.; Le Ru, E. C.; Etchegoin, P. G. Single-Molecule Surface-Enhanced Raman Spectroscopy of Nonresonant Molecules. *J. Am. Chem. Soc.* **2009**, *131*, 14466.

(73) Le Ru, E. C.; Blackie, E.; Meyer, M.; Etchegoin, P. G. Surface enhanced Raman scattering enhancement factors: a comprehensive study. *J. Phys. Chem. C* **2007**, *111*, 13794.

(74) Blackie, E. J.; Ru, E. C. L.; Etchegoin, P. G. Single-Molecule Surface-Enhanced Raman Spectroscopy of Nonresonant Molecules. *J. Am. Chem. Soc.* **2009**, *131*, 14466.

(75) Stranahan, S. M.; Willets, K. A. Super-resolution Optical Imaging of Single-Molecule SERS Hot Spots. *Nano Lett.* **2010**, *10*, 3777.

(76) Weber, M. L.; Litz, J. P.; Masiello, D. J.; Willets, K. A. Super-Resolution Imaging Reveals a Difference between SERS and Luminescence Centroids. *ACS Nano* **2012**, *6*, 1839.

(77) Lim, D.-K.; Jeon, K.-S.; Kim, H. M.; Nam, J.-M.; Suh, Y. D. Nanogap-engineerable Raman-active nanodumbbells for single-molecule detection. *Nature Materials* **2009**, *9*, 60.

(78) Dieringer, J. A.; Lettan, R. B., 2nd; Scheidt, K. A.; Van Duyne, R. P. A frequency domain existence proof of single-molecule surface-enhanced Raman spectroscopy. *J Am Chem Soc* **2007**, *129*, 16249.

(79) Michaels, A. M.; Nirmal, M.; Brus, L. E. Surface enhanced Raman spectroscopy of individual rhodamine 6G molecules on large Ag nanocrystals. *J. Am. Chem. Soc.* **1999**, *121*, 9932.

(80) Park, B. K.; Jeong, S.; Kim, D.; Moon, J.; Lim, S.; Kim, J. S. Synthesis and size control of monodisperse copper nanoparticles by polyol method. *J. Colloid Interface Sci.* **2007**, *311*, 417.

(81) Qian, X. M.; Nie, S. M. Single-molecule and single-nanoparticle SERS: from fundamental mechanisms to biomedical applications. *Chem. Soc. Rev.* **2008**, *37*, 912.

(82) Camden, J. P.; Dieringer, J. A.; Wang, Y.; Masiello, D. J.; Marks, L. D.; Schatz, G. C.; Van Duyne, R. P. Probing the structure of single-molecule surface-enhanced Raman scattering hot spots. *J. Am. Chem. Soc.* **2008**, *130*, 12616.

(83) Link, S.; El-Sayed, M. A. Size and temperature dependence of the plasmon absorption of colloidal gold nanoparticles. *J. Phys. Chem. B* **1999**, *103*, 4212.

(84) Jeanmaire, D. L.; Van Duyne, R. P. Surface raman spectroelectrochemistry. *Journal of Electroanalytical Chemistry and Interfacial Electrochemistry* **1977**, *84*, 1.

(85) Qian, X. M.; Nie, S. M. Single-molecule and single-nanoparticle SERS: from fundamental mechanisms to biomedical applications. *Chem. Soc. Rev.* **2008**, *37*, 912.

(86) Camden, J. P.; Dieringer, J. A.; Wang, Y.; Masiello, D. J.; Marks, L. D.; Schatz, G. C.; Van Duyne, R. P. Probing the Structure of Single-Molecule Surface-Enhanced Raman Scattering Hot Spots. *J. Am. Chem. Soc.* **2008**, *130*, 12616.

(87) Kneipp, K.; Wang, Y.; Kneipp, H.; Perelman, L.; Itzkan, I.; Dasari, R.; Feld, M. Single Molecule Detection Using Surface-Enhanced Raman Scattering (SERS). *Phys. Rev. Lett.* **1997**, *78*, 1667.

(88) Kuncicky, D. M.; Prevo, B. G.; Velev, O. D. Controlled assembly of SERS substrates templated by colloidal crystal films. *J. Mater. Chem.* **2006**, *16*, 1207.

(89) Banholzer, M. J.; Qin, L.; Millstone, J. E.; Osberg, K. D.; Mirkin, C. A. On-wire lithography: synthesis, encoding and biological applications. *Nature Protocols* **2009**, *4*, 838.

(90) White, I. M.; Gohring, J.; Fan, X. SERS-based detection in an optofluidic ring resonator platform. *Opt. Express* **2007**, *15*, 17433.

(91) Jackson, J. B.; Westcott, S. L.; Hirsch, L. R.; West, J. L.; Halas, N. J. Controlling the surface enhanced Raman effect via the nanoshell geometry. *Appl. Phys. Lett.* **2003**, *82*, 257.

(92) Hu, M.; Fattal, D.; Li, J.; Li, X.; Li, Z.; Williams, R. S. Optical properties of sub-wavelength dielectric gratings and their application for surface-enhanced Raman scattering. *Appl. Phys. A* **2011**, *105*, 261.

(93) Li, J.; Fattal, D.; Li, Z. Plasmonic optical antennas on dielectric gratings with high field enhancement for surface enhanced Raman spectroscopy. *Appl. Phys. Lett.* **2009**, *94*, 263114.

(94) Kim, S.-m.; Zhang, W.; Cunningham, B. T. Coupling discrete metal nanoparticles to photonic crystal surface resonant modes and application to Raman spectroscopy. *Opt. Express* **2010**, *18*, 4300.

(95) Moharam, M. G.; Gaylord, T. K. Rigorous coupled-wave analysis of metallic surface-relief gratings. *Journal of the Optical Society of America A* **1986**, *3*, 1780.

(96) Fang, Y.; Seong, N. H.; Dlott, D. D. Measurement of the Distribution of Site Enhancements in Surface-Enhanced Raman Scattering. *Science* **2008**, *321*, 388.

(97) Margueritat, J. r. m.; Gehan, H. l. n.; Grand, J.; Lévi, G.; Aubard, J.; Félidj, N.; Bouhelier, A.; Colas-Des-Francs, G.; Markey, L.; Marco De Lucas, C.; Dereux, A.; Finot, E. Influence of the Number of Nanoparticles on the Enhancement Properties of Surface-Enhanced Raman Scattering Active Area: SensitivityversusRepeatability. *ACS Nano* **2011**, *5*, 1630.

(98) Wang, Z. B.; Luk'yanchuk, B. S.; Guo, W.; Edwardson, S. P.; Whitehead, D. J.; Li, L.; Liu, Z.; Watkins, K. G. The influences of particle number on hot spots in strongly coupled metal nanoparticles chain. *The Journal of chemical physics* **2008**, *128*, 094705.

(99) Xu, X.; Kim, K.; Li, H.; Fan, D. L. Ordered Arrays of Raman Nanosensors for Ultrasensitive and Location Predictable Biochemical Detection. *Adv. Mater.* **2012**, *In press.*

(100) Gunnarsson, L.; Bjerneld, E. J.; Xu, H.; Petronis, S.; Kasemo, B.; Käll, M. Interparticle coupling effects in nanofabricated substrates for surface-enhanced Raman scattering. *Appl. Phys. Lett.* **2001**, *78*, 802.

(101) Wei, Q. H.; Su, K. H.; Durant, S.; Zhang, X. Plasmon Resonance of Finite One-Dimensional Au Nanoparticle Chains. *Nano Lett.* **2004**, *4*, 1067.

(102) Gao, J. H.; Liang, G. L.; Cheung, J. S.; Pan, Y.; Kuang, Y.; Zhao, F.; Zhang, B.; Zhang, X. X.; Wu, E. X.; Xu, B. Multifunctional yolk-shell nanoparticles: A potential MRI contrast and anticancer agent. *J. Am. Chem. Soc.* **2008**, *130*, 11828.

(103) Xu, X.; Hasan, D.; Wang, L.; Chakravarty, S.; Chen, R. T.; Fan, D. L.; Wang, A. X. Guided-mode-resonance-coupled plasmonic-active SiO2 nanotubes for surface enhanced Raman spectroscopy. *Appl. Phys. Lett.* **2012**, *100*, 191114.

(104) Lee, S. H.; Zhu, F. Q.; Chien, C. L.; Markovic, N. Effect of geometry on magnetic domain structure in Ni wires with perpendicular anisotropy: A magnetic force microscopy study. *Phys Rev B* **2008**, *77*.

(105) Chen, M.; Chien, C. L.; Searson, P. C. Potential modulated multilayer deposition of multisegment Cu/Ni nanowires with tunable magnetic properties. *Chem. Mater.* **2006**, *18*, 1595.

(106) Chien, C. L.; Zhu, F. Q.; Zhu, J. G. Patterned nanomagnets. *Phys Today* **2007**, *60*, 40.

(107) Böhme, R.; Richter, M.; Cialla, D.; Rösch, P.; Deckert, V.; Popp, J. Towards a specific characterisation of components on a cell surface-combined TERS-investigations of lipids and human cells. *J Raman Spectrosc* **2009**, *40*, 1452.

(108) Kneipp, J.; Wittig, B.; Bohr, H.; Kneipp, K. Surface-enhanced Raman scattering: a new optical probe in molecular biophysics and biomedicine. *Theor. Chem. Acc.* **2010**, *125*, 319.

(109) Kneipp, J.; Kneipp, H.; McLaughlin, M.; Brown, D.; Kneipp, K. In vivo molecular probing of cellular compartments with gold nanoparticles and nanoaggregates. *Nano Lett.* **2006**, *6*, 2225.

(110) Doane, T. L.; Burda, C. The unique role of nanoparticles in nanomedicine: imaging, drug delivery and therapy. *Chem. Soc. Rev.* **2012**, *41*, 2885.

(111) Bardhan, R.; Chen, W.; Bartels, M.; Perez-Torres, C.; Botero, M. F.; McAninch, R. W.; Contreras, A.; Schiff, R.; Pautler, R. G.; Halas, N. J.; Joshi, A. Tracking of Multimodal Therapeutic Nanocomplexes Targeting Breast Cancer in Vivo. *Nano Lett.* **2010**, *10*, 4920.

(112) Xu, X.; Li, H.; Hasan, D.; Ruoff, R. S.; Wang, A. X.; Fan, D. L. Near-Field Enhanced Plasmonic-Magnetic Bifunctional Nanotubes for Single Cell Bioanalysis. *Adv. Funct. Mater.* **2013**, *23*, 4332.

(113) Xu, Z. P.; Zeng, Q. H.; Lu, G. Q.; Yu, A. B. Inorganic nanoparticles as carriers for efficient cellular delivery. *Chem. Eng. Sci.* **2006**, *61*, 1027.

(114) Orozco, J.; Vilela, D.; Valdés-Ramírez, G.; Fedorak, Y.; Escarpa, A.; Vazquez-Duhalt, R.; Wang, J. Efficient Biocatalytic Degradation of Pollutants by Enzyme-Releasing Self-Propelled Motors. *Chemistry - A European Journal* **2014**, *20*, 2866.

(115) Salem, A. K.; Searson, P. C.; Leong, K. W. Multifunctional nanorods for gene delivery. *Nature Materials* **2003**, *2*, 668.

(116) Wildt, B.; Wirtz, D.; Searson, P. C. Triggering cell detachment from patterned electrode arrays by programmed subcellular release. *Nature Protocols* **2010**, *5*, 1273.

(117) Mali, P.; Bhattacharjee, N.; Searson, P. C. Electrochemically Programmed Release of Biomolecules and Nanoparticles. *Nano Lett.* **2006**, *6*, 1250.

(118) Lee, S. E.; Liu, G. L.; Kim, F.; Lee, L. P. Remote Optical Switch for Localized and Selective Control of Gene Interference. *Nano Lett.* **2009**, *9*, 562.

(119) Peiris, P. M.; Bauer, L.; Toy, R.; Tran, E.; Pansky, J.; Doolittle, E.; Schmidt, E.; Hayden, E.; Mayer, A.; Keri, R. A.; Griswold, M. A.; Karathanasis, E. Enhanced Delivery of Chemotherapy to Tumors Using a Multicomponent Nanochain with Radio-Frequency-Tunable Drug Release. *ACS Nano* **2012**, *6*, 4157.

(120) Campion, A.; Kambhampati, P. Surface-enhanced Raman scattering. *Chem. Soc. Rev.* **1998**, *27*, 241.

(121) Xu, X. B.; Kim, K.; Li, H. F.; Fan, D. L. Ordered Arrays of Raman Nanosensors for Ultrasensitive and Location Predictable Biochemical Detection. *Adv. Mater.* **2012**, *24*, 5457.

(122) Xu, X.; Li, H.; Hasan, D.; Ruoff, R. S.; Wang, A. X.; Fan, D. L. Near-Field Enhanced Plasmonic-Magnetic Bifunctional Nanotubes for Single Cell Bioanalysis. *Adv. Funct. Mater.* **2013**, *23*.

(123) Klipp, E.; Liebermeister, W.; Wierling, C.; Kowald, A.; Lehrach, H.; Herwig, R. *Systems Biology*; Wiley-Blackwell, 2009.

(124) Arlett, J. L.; Myers, E. B.; Roukes, M. L. Comparative advantages of mechanical biosensors. *Nature Nanotech.* **2011**, *6*, 203.

(125) Kim, K.; Xu, X.; Guo, J.; Fan, D. L. Ultrahigh-speed rotating nanoelectromechanical system devices assembled from nanoscale building blocks. *Nat Commun* **2014**, *5*.

(126) Férey, G. Hybrid porous solids: past, present, future. *Chem. Soc. Rev.* **2008**, *37*, 191.

(127) Whitney, T. M.; Searson, P. C.; Jiang, J. S.; Chien, C. L. Fabrication and Magnetic Properties of Arrays of Metallic Nanowires. *Science* **1993**, *261*, 1316.

(128) Willets, K. A.; Van Duyne, R. P. Localized surface plasmon resonance spectroscopy and sensing. *Annu. Rev. Phys. Chem.* **2007**, *58*, 267.

(129) Le Ru, E. C.; Etchegoin, P. G. Single-Molecule Surface-Enhanced Raman Spectroscopy. *Annu. Rev. Phys. Chem.* **2012**, *63*, 65.

(130) Fan, D. L.; Zhu, F. Q.; Xu, X.; Cammarata, R. C.; Chien, C. L. Electronic properties of nanoentities revealed by electrically driven rotation. *Proceedings of the National Academy of Sciences* **2012**, *109*, 9309.

(131) Jones, T. B. *Electromechanics of Particles*; CambridgeUniversity Press: New York, 1995.

(132) Brad, A. J.; Faulkner, L. R. *Electrochemical Methods*; Wiley: New York, 1980.

(133) Munson, B. R.; Young, D. F.; Okiishi, T. H. *Fundamentals of Fluid Mechanics*; 4th ed.; John Wiley, 2002.

(134) Nikolic, J.; Expósito, E.; Iniesta, J.; González-Garcia, J.; Montiel, V. Theoretical Concepts and Applications of a Rotating Disk Electrode. *J. Chem. Educ.* **2000**, *77*, 1191.

(135) Levich, V. G. *Physicochemical Hydrodynamics*; Prentice-Hall: New York, 1962.